



저작자표시-비영리-변경금지 2.0 대한민국

이용자는 아래의 조건을 따르는 경우에 한하여 자유롭게

- 이 저작물을 복제, 배포, 전송, 전시, 공연 및 방송할 수 있습니다.

다음과 같은 조건을 따라야 합니다:



저작자표시. 귀하는 원저작자를 표시하여야 합니다.



비영리. 귀하는 이 저작물을 영리 목적으로 이용할 수 없습니다.



변경금지. 귀하는 이 저작물을 개작, 변형 또는 가공할 수 없습니다.

- 귀하는, 이 저작물의 재이용이나 배포의 경우, 이 저작물에 적용된 이용허락조건을 명확하게 나타내어야 합니다.
- 저작권자로부터 별도의 허가를 받으면 이러한 조건들은 적용되지 않습니다.

저작권법에 따른 이용자의 권리는 위의 내용에 의하여 영향을 받지 않습니다.

이것은 [이용허락규약\(Legal Code\)](#)을 이해하기 쉽게 요약한 것입니다.

[Disclaimer](#)

공학박사학위논문

Synthesis and characterization of
phosphorus-based organic and boron nitride-
based inorganic flame retardants for polymers

고분자의 난연성 향상을 위한 유기 인계 난연제 및
질화붕소 기반의 무기계 난연제의 합성에 관한 연구

2022년 8월

서울대학교 대학원

화학생물공학부

심민지

**Synthesis and characterization of phosphorus-based
organic and boron nitride-based inorganic flame
retardants for polymers**

by

Min-Ji Sim

Adviser: Professor Jong-Chan Lee, Ph. D.

**Submitted in Partial Fulfillment
of the Requirements for the Degree of
DOCTOR OF PHILOSOPHY**

August, 2022

**School of Chemical and Biological Engineering
College of Engineering
Graduate School
Seoul National University**

Abstract

This study introduces the strategies to further improve the flame retardancy of previously reported phosphorus-containing flame retardants. Firstly, a novel phosphorus/nitrogen-containing flame retardant (PNFR) was designed to maximize the flame retardancy via synergistic effect of phosphorus and nitrogen. The PNFR was successfully synthesized and incorporated into polyketone which is one of engineering plastics. The neat polyketone showed the limiting oxygen index (LOI) value of 20.2% and no rating in vertical burning test, meaning that the neat polyketone has highly flammable property. In contrast, as introducing 7 wt% PNFR into polyketone, it exhibited the increased LOI value up to 25.9% and VTM-0 rating in vertical burning test, which indicates that PNFR could induce flame retardancy into polyketone. Here, it was revealed that the release of an inert gas as well as the effective char-forming ability of PNFR, resulting from the synergistic effect of phosphorus and nitrogen, significantly improve the flame retardancy of polyketone.

Secondly, it was found that the crosslinked network can enhance the flame retardancy of phosphorus-containing flame retardant. A self-polymerizable

phosphonate, bis(cardanyl) phenylphosphonate (CP), was synthesized and incorporated into poly(vinyl chloride) (PVC) as polymer matrix. Herein, the flame retardancy and flexibility of PVC improved with an increase in the CP content (wt%) due to the presence of the phosphonate group and long alkyl chain of CP, respectively. In addition, CP can be self-polymerized by heat treatment and that the crosslinked network of CP leads to an additional enhancement in flame retardancy of PVC by inducing anti-dripping property and the formation of graphitized char layer. CP with self-polymerization properties is a promising candidate to improve the thermal stability, flame retardancy, and flexibility of PVC while maintaining its transparency and migration stability.

Finally, among two-dimensional layered inorganic materials, boron nitride (BN) has fascinating features such as electrical insulation and outstanding chemical and thermal stability, suggesting that BN can be a promising filler for high-performance nanocomposites. However, a severe aggregation of BN due to its low functionalization efficiency has limited the further applications. Herein, to improve the dispersion of BN within polymer nanocomposites, a facile functionalization method of BN was proposed. A boron nitride with functional groups (f-BN), which was obtained by the calcination of melamine-boric acid complex, was further functionalized

using L-lactic acid; L-BN. Observations revealed that L-lactic acid was grafted onto f-BN via two main functionalization routes by heat treatment. Herein, to investigate the effect of the functionalization degree of L-BN on flame retardancy, it was introduced into poly(lactic acid), PLA. L-BN-25 formed a hydrogen bond with PLA, thereby improving flame retardancy. On the other hand, since L-BN-90 has a functionalization degree of 26%, the amount of carbon and oxygen is relatively increased, resulting in the reduction of the flame retardancy. However, f-BN and L-BN enhanced the flame retardancy of PLA with a small content due to improved dispersion state compared to commercially available BN. Since the functionalization degree of L-BN could be adjusted depending on the heating conditions, it is an effective strategy that would be applied to various further applications.

Keywords: Phosphorus-containing flame retardant, phosphorus/nitrogen-containing flame retardant, polyketone, poly(vinyl chloride), flame retardancy, boron nitride, surface functionalization

Student Number: 2018-34202

Table of Contents

Abstract.....	i
List of Tables.....	vii
List of Figures	ix

Chapter 1

Introduction

1.1. Flame retardant	2
1.2. Non-halogen-based flame retardant	3
1.3. Motivation	5
1.4. References.....	7

Chapter 2

Preparation of a novel phosphorus-nitrogen flame retardant and its effects on the flame retardancy and physical properties of polyketone

2.1. Introduction	1 1
2.2. Experimental.....	1 5
2.3. Results and discussion.....	1 9
2.4. Conclusion	3 2
2.5. References.....	3 4

Chapter 3

Enhancement of flame retardancy and physical property for poly(vinyl chloride) having renewable cardanol-based self-polymerizable phosphonate under heat treatment process

3.1. Introduction	5 7
3.2. Experimental.....	6 0
3.3. Results and discussion.....	6 6
3.4. Conclusion	8 2
3.5. References.....	8 4

Chapter 4

Controllable surface functionalization of boron nitride by heat treatment and its effect on flame retardancy of poly(lactic acid)

4.1. Introduction	1 2 2
4.2. Experimental.....	1 2 5
4.3. Results and discussion.....	1 2 9
4.4. Conclusion	1 4 0
4.5. References.....	1 4 2
Abstract in Korean.....	1 6 3

List of Tables

Table 2.1. Composition and flame-retarding properties of neat polyketone (PK) and flame-retarding PKs featuring different phosphorus-nitrogen flame retardant (PNFR) contents

Table 2.2. Thermogravimetric analysis data of neat and flame-retarding polyketones (PKs) in nitrogen and air atmosphere; here, PK-0, PK-3, PK-5, and PK-7 represent PK-phosphorus-nitrogen flame retardant (PNFR) systems that contain 0, 3, 5, and 7 wt% PNFR, respectively, while T_{initial} , T_{max1} , T_{max2} , and T_{max3} are the initial, first, second, and third decomposing temperatures, respectively

Table 2.3. Experimental (thermogravimetric analysis-determined) and calculated residual char of neat and flame-retarding polyketones (PKs) in nitrogen and air atmosphere; here, PK-0, PK-3, PK-5, and PK-7 represent PK-phosphorus-nitrogen flame retardant (PNFR) systems that contain 0, 3, 5, and 7 wt% PNFR, respectively

Table 2.4. Differential scanning calorimetry results of neat and flame-retarding polyketones (PKs), where PK-0, PK-3, PK-5, and PK-7 represent PK-phosphorus-nitrogen flame retardant (PNFR) systems that contain 0, 3,

5, and 7 wt% PNFR, respectively, while T_m , ΔH_f , and X_c are the melting temperature, enthalpy of fusion, and crystallinity, respectively ($\Delta H_{f100\%}$ is 100% crystalline of polyketone, 227 J g^{-1})

Table 3.1. Formulations of the PVC films with different CP contents

Table 3.2. FTIR assignments for cardanol and CP

Table 3.3. TGA results and P content in residual char of the PVC films

Table 3.4. FTIR assignments for thermal degradation behavior of PVC-0 and PVC-10

Table 3.5. LOI and UL-94 test results of the PVC and X-PVC films

List of Figures

Figure 2.1. Schematics for (a) synthesis of phosphorus-nitrogen flame retardant (PNFR) and (b) preparation of neat and flame-retarding polyketones (PKs) via solution casting. Here TEA and THF are triethylamine and tetrahydrofuran, respectively, while PK-0 and PK-7 are pure PK and PK-PNFR containing 93 wt% PK and 7 wt% PNFR, respectively

Figure 2.2. ^1H nuclear magnetic resonance spectrum of phosphorus-nitrogen flame retardant

Figure 2.3. Thermogravimetric analysis curves of phosphorus-nitrogen flame retardant in nitrogen and air atmosphere

Figure 2.4. Fourier-transform infrared spectra of phosphorus-nitrogen flame retardant in the 25-500 °C temperature range in air atmosphere

Figure 2.5. (a) Scanning electron microscopy (SEM) image and (b) SEM-energy dispersive X-ray spectroscopy results of residual char after

combustion of phosphorus-nitrogen flame retardant. Inset in (a) is a digital photograph of residual char

Figure 2.6. Thermogravimetric analysis curves of neat and flame-retarding polyketones (PKs) in (a) nitrogen and (b) air atmosphere; where PK-0, PK-3, PK-5, and PK-7 represent PK-phosphorus-nitrogen flame retardant (PNFR) systems that contain 0, 3, 5, and 7 wt% PNFR, respectively

Figure 2.7. Scanning electron microscopy images of residual char from (a) PK-0, (b) PK-3, (c) PK-5, and (d) PK-7, where PK-0, PK-3, PK-5, and PK-7 represent PK-phosphorus-nitrogen flame retardant (PNFR) systems that contain 0, 3, 5, and 7 wt% PNFR, respectively

Figure 2.8. Fourier-transform infrared spectra of (a) PK-0 and (b) PK-7 in the 25-500 °C temperature range in air

Figure 2.9. Differential scanning calorimetry thermograms of neat and flame-retarding polyketones (PKs), where PK-0, PK-3, PK-5, and PK-7 represent PK-phosphorus-nitrogen flame retardant (PNFR) systems that contain 0, 3, 5, and 7 wt% PNFR, respectively

Figure 2.10. X-ray diffraction patterns of neat and flame-retarding PKs, where PK-0, PK-3, PK-5, and PK-7 represent PK-phosphorus-nitrogen flame retardant (PNFR) systems that contain 0, 3, 5, and 7 wt% PNFR, respectively

Figure 3.1. Schematic illustration of synthesis route of CP

Figure 3.2. (a) FTIR spectra of cardanol and CP, (b) ^1H NMR spectra of cardanol and CP, and ^{31}P NMR spectra of (c) phenylphosphonic acid and (d) CP

Figure 3.3. Transmittance spectra of PVC films over the wavelength range of 400-700 nm (inset pictures: digital photographs of the PVC films)

Figure 3.4. SEM-EDS of (a) PVC-0 and (b) PVC-10

Figure 3.5. TEM-EDS of (a) PVC-0 and (b) PVC-10

Figure 3.6. TGA curves of the PVC films in N_2

Figure 3.7. DTG curves of the PVC films

Figure 3.8. SEM images for the residual char of (a) PVC-0, (b) PVC-5, (c) PVC-7, and (d) PVC-10

Figure 3.9. TG-FTIR spectra of (a) PVC-0 and (b) PVC-10

Figure 3.10. TGA curves of cardanol and CP

Figure 3.11. DSC curves of cardanol and CP

Figure 3.12. FTIR spectra of the PVC films after heat-treatment at (a) 140 °C for 1 h and (b) 120 °C for 1 h

Figure 3.13. DSC curves of the (a) PVC films and (b) X-PVC films

Figure 3.14. GPC results of CP of before and after the heat-treatment

Figure 3.15. (a) LOI values and UL-94 ratings of the PVC and X-PVC films, (b) digital photographs for residual char of PVC-10 and X-PVC-10,

(c) Raman spectra for residual char of PVC-10 and X-PVC-10, and (d) I_D/I_G values of the PVC and X-PVC films, as obtained from the Raman spectroscopy results

Figure 3.16. Digital photographs of burning process for (a) PVC-0, (b) PVC-10, and (c) X-PVC-5

Figure 3.17. Raman spectra for residual char of the (a) PVC films and the (b) X-PVC films

Figure 3.18. Tensile test results of the (a) PVC and (b) X-PVC films

Figure 3.19. Glass transition temperatures (T_g) of the (a) PVC films and (b) X-PVC films from DSC thermograms

Figure 3.20. XRD patterns of the PVC films

Figure 3.21. Digital photographs of X-PVC-10 under various deformation conditions

Figure 3.22. Calibration curve based on the UV absorption at 265 nm against amount of CP

Figure 3.23. Migration stability test of the PVC films in (a) n-hexane and (b) distilled water; migration stability test of the X-PVC films in (c) n-hexane and (d) distilled water

Figure 3.24. Digital photographs of the X-PVC films

Figure 4.1. (a) Schematic illustration of the synthetic process of boron nitride with functional groups (f-BN), (b) fourier transform infrared (FTIR) spectra of commercially available BN and f-BN, and (c) transmission electron microscopy (TEM) image of f-BN (inset: high-magnification TEM image)

Figure 4.2. X-ray diffraction (XRD) patterns of (a) commercially available BN and (b) f-BN

Figure 4.3. (a) Thermogravimetric analysis (TGA) curves of f-BN and L-BNs (inset: the degree of functionalization depending on heating conditions), and (b) FTIR spectra of L-BN-25, L-BN-90, and L-lactic acid

Figure 4.4. Thermogravimetric analysis (TGA) curves of f-BN, L-BN-50, and L-BN-120

Figure 4.5. The Fourier transform infrared (FTIR) spectra of f-BN before and after heat treatment to 500 °C

Figure 4.6. ^1H nuclear magnetic resonance (NMR) spectrum of the crude product after the further surface functionalization

Figure 4.7. The FTIR spectra of L-lactic acid, L-BN-50, and L-BN-120

Figure 4.8. (a) B_{1s} and (b) N_{1s} X-ray photoelectron spectroscopy (XPS) profile of f-BN

Figure 4.9. (a) B_{1s} X-ray photoelectron spectroscopy (XPS) profile of L-BN-25, (b) N_{1s} XPS profile of L-BN-25, (c) B_{1s} XPS profile of L-BN-90, and (d) N_{1s} XPS profile of L-BN-90

Figure 4.10. (a) B_{1s} XPS profile of L-BN-50, (b) N_{1s} XPS profile of L-BN-50, (c) B_{1s} XPS profile of L-BN-120, and (d) N_{1s} XPS profile of L-BN-120

Figure 4.11. The solid-state NMR spectra of f-BN and L-BNs

Figure 4.12. FTIR spectra of the product of the reaction between L-lactic acid and boric acid under heat treatment

Figure 4.13. Routes of the surface functionalization of f-BN using L-lactic acid under various heating conditions

Figure 4.14. The dispersion test for f-BN and L-BNs in (a) n-hexane, (b) chloroform, (c) water, and (d) isopropyl alcohol (IPA)

Figure 4.15. SEM images and EDS mapping of (a) PLA, (b) PLA-3.0fBN, (c) PLA-3.0LBN25, and (d) PLA-3.0LBN90

Figure 4.16. The limiting oxygen index (LOI) results (a) PLA, PLA-BN, and PLA-fBN, (b) PLA, PLA-LBN25, and PLA-LBN90

Figure 4.17. SEM image and EDS mapping of PLA-3.0BN

Chapter 1

Introduction

1.1. Flame retardant

In recent years, as the application of polymers has been expanded to various fields such as electronics, construction and aerospace, the research to improve the intrinsic combustible properties of polymers, which is one of the causes of limiting these applications, has been attracting considerable attention [1, 2]. The effective strategy to impart flame retardancy is to introduce flame retardant elements (e.g., halogen, phosphorus, nitrogen, and inorganic materials) into the polymers [3, 4]. The introduction methods of flame retardants can be classified into reactive-type and additive-type method [5]. Reactive-type method is to form the chemical bond between polymer matrix and flame retardants [6]. While this method does not leach out small molecules [7], it is uneconomical due to the complex process of designing new system for each polymer matrix. On the contrary, since additive-type method is to physically add flame retardant into polymer matrix [5], this method is simple and economical process compared to reactive-type method. However, it has disadvantages such as poor compatibility and leaching out, resulting in the deterioration of mechanical properties of polymer matrix [8, 9].

1.2. Non-halogen-based flame retardant

Among the flame retardants, halogen-based flame retardants were widely used in various industrial fields owing to excellent flame retardancy. However, since they generate the harmful substances to the environment and human during combustion process, their use has been recently regulated all over the world [10]. Therefore, the many studies on the non-halogen-based flame retardants have been conducted.

Inorganic flame retardant, one of the representative non-halogen-based flame retardants, shows the superior thermal stability and flame retardancy [11]. In particular, inorganic flame retardant is known to impart flame retardancy by forming a metal oxide layer on the surface of polymer matrix during combustion process [12, 13]. However, in order to induce flame retardancy, a considerable amount of flame retardant should be added into polymer matrix. In addition, it has a disadvantage of poor compatibility with polymer matrix [14]. Therefore, it is imperative to develop a novel flame retardant capable of imparting effective flame retardancy with a relatively small amount.

Accordingly, the research on organic phosphorus-containing flame

retardant as other representative non-halogen-based flame retardant has been attracted attention. Organic phosphorus-containing flame retardant has advantages such as low toxicity, high flame retardancy efficiency, and good compatibility with polymer matrix [15]. The flame retardant mechanism of phosphorus-containing flame retardant includes the gas phase and condensed phase mechanism [16]. In gas phase, the active radicals such as $\text{PO}\cdot$ and $\text{PO}_2\cdot$ which are generated by decomposition of phosphorus-containing flame retardant during combustion process scavenge the hydroxyl or hydrogen radicals which are required for combustion [17]. On the other hand, in condensed phase, polyphosphoric acid which is produced from decomposition of phosphorus-containing flame retardant can catalyze the carbonization and form the barrier on polymer surface [15]. This barrier prevents the spread of fire by inhibiting the heat or mass transfer from/to polymer matrix. Therefore, organic phosphorus-containing flame retardant can impart a flame retardant effect with a relatively small amount compared to the inorganic flame retardant via these two flame retardant mechanisms.

1.3. Motivation

In previous research, a phosphorus-containing flame retardant was developed for poly(lactic acid) (PLA) [18]. When the phosphorus-containing flame retardant was introduced into PLA, the increase of limiting oxygen index (LOI) value in LOI test and the achievement of VTM-0 in vertical burning test were observed, indicating that the phosphorus-containing flame retardant could enhance the flame retardancy of PLA. However, when this phosphorus-containing flame retardant was applied to other polymer matrices (e.g., polyurethane, polyketone), no noticeable flame retardancy was observed. Thus, it was believed that when phosphorus element is used alone, it is insufficient to maximize the flame retardant effect.

Therefore, this study introduces strategies for maximizing the flame retardant effect of phosphorus-containing flame retardants. First, a phosphorus/nitrogen-containing flame retardant was designed and synthesized to induce the synergistic effect of phosphorus and nitrogen. Secondly, to confirm the effect of crosslinked network on flame retardancy, a phosphorus-containing flame retardant with unsaturated alkyl chain was

developed. Finally, boron nitride which is widely used as filler of polymer nanocomposites was synthesized and surface functionalized.

1.4. References

1. Xiao, Y., et al., *In situ co-polymerization of high-performance polybenzoxazine/silica aerogels for flame-retardancy and thermal insulation*. Journal of Applied Polymer Science, 2021. **138**(18): p. 50333.
2. Liu, Q., et al., *Recent advances in the flame retardancy role of graphene and its derivatives in epoxy resin materials*. Composites Part A: Applied Science and Manufacturing, 2021. **149**: p. 106539.
3. Ai, L., et al., *Synergistic flame retardant effect of organic phosphorus–nitrogen and inorganic boron flame retardant on polyethylene*. Polymer Engineering & Science, 2020. **60**(2): p. 414-422.
4. Luo, H., et al., *An efficient organic/inorganic phosphorus–nitrogen–silicon flame retardant towards low-flammability epoxy resin*. Polymer Degradation and Stability, 2020. **178**: p. 109195.
5. Marosi, G., et al., *Reactive and additive phosphorus-based flame retardants of reduced environmental impact*, in *Polymer Green Flame Retardants*. 2014, Elsevier. p. 181-220.
6. Biswas, B. and B.K. Kandola, *The effect of chemically reactive type flame retardant additives on flammability of PES toughened epoxy resin and carbon fiber-reinforced composites*. Polymers for Advanced Technologies, 2011. **22**(7): p. 1192-1204.
7. Kanno, T., et al., *Flame resistant nylon-6, 6 composites with improved mechanical strength by the combination of additive-and*

- reactive-type flame retardants*. Polymer Journal, 2007. **39**(4): p. 347-358.
8. Jian, R., et al., *A facile method to flame-retard epoxy resin with maintained mechanical properties through a novel P/N/S-containing flame retardant of tautomerization*. Materials Letters, 2017. **204**: p. 77-80.
 9. Yang, R., et al., *Synthesis, mechanical properties and fire behaviors of rigid polyurethane foam with a reactive flame retardant containing phosphazene and phosphate*. Polymer Degradation and Stability, 2015. **122**: p. 102-109.
 10. Zabihi, O., et al., *A sustainable approach to scalable production of a graphene based flame retardant using waste fish deoxyribonucleic acid*. Journal of Cleaner Production, 2020. **247**: p. 119150.
 11. Peng, H.K., et al., *Mechanical properties, thermal stability, sound absorption, and flame retardancy of rigid PU foam composites containing a fire-retarding agent: Effect of magnesium hydroxide and aluminum hydroxide*. Polymers for Advanced Technologies, 2019. **30**(8): p. 2045-2055.
 12. Song, G., et al., *Preparation and characterization of flame retardant form-stable phase change materials composed by EPDM, paraffin and nano magnesium hydroxide*. Energy, 2010. **35**(5): p. 2179-2183.
 13. Yeh, J., H. Yang, and S. Huang, *Combustion of polyethylene filled with metallic hydroxides and crosslinkable polyethylene*. Polymer Degradation and Stability, 1995. **50**(2): p. 229-234.
 14. Cheng, X., et al., *Flame-retardant mechanism of zinc borate and magnesium hydroxide in aluminum hypophosphite-based*

- combination for TPE-S composites. Journal of Fire Sciences, 2019. 37(3): p. 273-300.*
15. Huo, S., et al., *Phosphorus-containing flame retardant epoxy thermosets: Recent advances and future perspectives. Progress in Polymer Science, 2021. 114: p. 101366.*
 16. Green, J., *A review of phosphorus-containing flame retardants. Journal of Fire Sciences, 1992. 10(6): p. 470-487.*
 17. Yu, S., et al., *Enhanced flame-retardant performance of poly (lactic acid)(PLA) composite by using intrinsically phosphorus-containing PLA. Progress in Natural Science: Materials International, 2018. 28(5): p. 590-597.*
 18. Sim, M.-J. and S.-H. Cha, *Efficient polymeric phosphorus flame retardant: flame retardancy, thermal property, and physical property on polylactide. Polymer Bulletin, 2019. 76(7): p. 3463-3479.*

Chapter 2

Preparation of a novel phosphorus-nitrogen flame retardant and its effects on the flame retardancy and physical properties of polyketone

2.1. Introduction

Nowadays, high-performance engineering plastics that present good thermal resistance, chemical resistance, and mechanical properties are using in various industries [1, 2]. An aliphatic polyketone (PK) has been attracting considerable interest as polymer that can compete with these engineering plastics [3, 4]. The aliphatic PK is prepared via the polymerization of carbon monoxide and olefins in perfectly alternating sequence using palladium catalyst [5-9]. In addition, aliphatic PK is a semicrystalline thermoplastic that exhibits superior mechanical properties, barrier properties, and high temperature and chemical resistance. Due to these characteristics, aliphatic PK can be used for various applications, such as barrier packaging, engineering, and as fiber [10-12]. However, despite its high thermal stability, the combustibility of aliphatic PK restricts its applications. While several reports on the structural and mechanical properties of PK have been published [13-17], studies on flame retardancy are lacking.

Flame retardants are materials that impart flame retardancy to combustible polymers and can be classified into additive and reactive types according to the application method to the polymer matrix [18, 19]. Reactive type flame

retardants are introduced via chemical reactions with the polymer, which indicates that while the possibility of the flame retardant to affect the intrinsic physical properties of the polymer is low [20], the application process to the polymer is challenging. On the other hand, since the introduction of additive type flame retardants is performed via physical processes, they can present a broad range of applications. Considering the low chemical reactivity of PK, it was considered that additive types of flame retardants could be applicable to it.

Additive type flame retardants, such as halogen [21], phosphorus [22], and inorganic compounds [23], have been used to impart flame-retarding ability to various polymers. Among them, halogen flame retardants have been widely used in various industries owing to their excellent flame retardancy. However, recently, specific brominated-flame retardants have become regulated because they are known to be harmful to human health and the environment [24-27]. Therefore, many researchers have reported that phosphorus-nitrogen intumescent flame retardants could be alternatives for brominated-flame retardants [28-30]. Shuangyue et al. investigated the synergism of phosphorus- and nitrogen-containing flame retardants for the flame retardancy of polyoxymethylene (POM) [31]. By comparison with that of neat POM, the limiting oxygen index (LOI) of POM that contained

24 wt% phosphorus and 8 wt% nitrogen flame retardants was increased from 15.5 to 28.6%. Organic phosphorus flame retardants suppress combustion via radical trapping and formation of phosphorus-rich char, while nitrogen flame retardants can release inert gases during combustion. Therefore, phosphorus- and nitrogen-containing flame retardants are expected to confer polymers outstanding flame-retarding ability via the synergistic effect of phosphorus and nitrogen. However, according to many reports, large amounts of phosphorus-nitrogen flame retardants (PNFR) would be required to confer high flame retardancy to polymers. Consequently, this could deteriorate the intrinsic mechanical properties of polymers due to the poor compatibility between flame retardants and polymers [32]. Bin et al. synthesized triazine as char-forming agent (CFA) for polypropylene (PP) [33] and reported that the V-0 rating and 30.2% LOI value were achieved at the CFA loading of 18 wt%. However, despite its superior flame retardancy, the mechanical properties of the CFA-PP system gradually decreased as the CFA amount increased. Chao and Zhanhu et al. prepared a phosphorus-nitrogen intumescent flame retardant, 2,2-diethyl-1,3-propanediol phosphoryl melamine (DPPM), to impart flame retardancy to rigid polyurethane foam [34]. While the LOI value of 29.5% and V-0 rating were achieved at the DPPM loading of 25 php, the compressive

strength of the DPPM-RPUF system decreased by 25.0% compared with that of neat RPUF. Therefore, we designed and prepared a new PNFR, which could confer excellent flame-retarding ability to PK when added to it in small amounts.

The flame-retarding abilities of the neat and flame-retarding PKs, which were fabricated via solution casting, were evaluated using thin material vertical burning tests (UL 94 VTM) and their LOIs. Then, the morphologies of the residual chars were analyzed using scanning electron microscopy (SEM). The thermal degradation behavior and thermal stability of the samples were investigated using thermogravimetric analysis (TGA). The flame-retarding mechanisms of PNFR and the PK-PNFR systems were evaluated using TGA combined with Fourier-transform infrared (FTIR) spectroscopy (TGA-FTIR). The crystallinity of the PK-PNFR systems depended on the PNFR content and was analyzed using differential scanning calorimetry (DSC) and X-ray diffraction (XRD) experiments.

2.2. Experimental

Materials

The PK (intrinsic viscosity ~ 1.42 dL g⁻¹) used in this study was a terpolymer comprising ethylene, propylene, and carbon monoxide (4 mol% ethylene was replaced by propylene) and was supplied by the Hyosung Corporation. Phenylphosphonic dichloride (PPDC), 4-aminophenol, and *m*-cresol were purchased from Sigma-Aldrich. Allyl alcohol and triethylamine were obtained from the Samchun Chemical Corporation. Tetrahydrofuran (THF) and ethyl acetate (EA) were purchased from Daejung Chemicals and Metals Corporation and were used without purification.

Synthesis of PNFR

The synthesis of PNFR is illustrated in Figure 2.1a. First, 4-aminophenol (0.0846 mol) and triethylamine (TEA) (0.2115 mol) were dissolved in THF (200 mL) in a round-bottom flask. Then, PPDC (0.0705 mol) was slowly dropwise added to the flask under reflux. Afterward, allyl alcohol (0.0846

mol) was immediately added to the flask. Then, the mixture continued to react under reflux for 24 h. When the reaction was completed, all the TEA salt was removed by filtering. The resulting mixture was then extracted with EA and deionized water, and the organic solution obtained after extraction was dried in vacuum. A dark brown viscous product was obtained, and the yield was ~78%.

Preparation of neat and flame-retarding PKs

Samples of neat and flame-retarding PKs were prepared using the solution casting method because PNFR has lower thermal stability than PK (Figure 2.1b). First, 12 g PK was dissolved in 80 g *m*-cresol. Then, different amounts of PNFR were added to the PK solution to generate PK-PNFR systems containing 3, 5, and 7 wt% PNFR (Table 2.1). After the solutions had been mixed, they were poured into Teflon molds and were dried at ~100 °C overnight. All samples were subsequently placed in a vacuum oven and were heated at 200 °C overnight. The PK-PNFR samples containing 0, 3, 5, and 7 wt% PNFR were denoted PK-0, PK-3, PK-5, and PK-7, respectively.

Characterization

All ^1H NMR tests were performed on a Bruker 400 MHz spectrometer at room temperature in chloroform-d. The FTIR spectra were recorded on a Bruker Alpha-Platinum attenuated total reflectance (ATR)-FTIR spectrometer over the range of 4,000-450 cm^{-1} . Flame retardancy was confirmed by conducting thin material vertical burning tests (UL 94 VTM), and the test results were interpreted according to the ASTM D 4804 standard using samples having dimensions 125 mm \times 50 mm \times 0.6 mm. In addition, the LOIs of samples were measured using a FT-LOI-404 (FESTEC) tester according to the ASTM D2863 standard. All samples were 120 mm \times 15 mm \times 0.6 mm, as well. The TGA experiments were performed from room temperature to 800 $^{\circ}\text{C}$ at the heating rate of 10 $^{\circ}\text{C min}^{-1}$ under nitrogen or air atmosphere using a TGA 4000 (Perkin Elmer) instrument. The flame-retarding mechanism was evaluated using the TGA and FTIR results. After elevating the temperature to the required temperature during TGA in air, the chemical structures of the samples were analyzed using FTIR. The morphology of the residual char was recorded using a field emission (FE)-SEM JSM-7610F Plus (JEOL) utilizing platinum-coated

samples. In addition, the phosphorus contents of the char surfaces were investigated using SEM-energy dispersive X-ray spectroscopy (SEM-EDS). All DSC experiments were carried out in nitrogen atmosphere using a Discovery DSC 25 (TA Instruments-Waters LLC) calorimeter. The samples were heated from -20 °C to 250 °C at the rate of 10 °C min⁻¹ and were held at 250 °C for 3 min to remove their thermal history. The samples were then cooled to -20 °C at the rate of 10 °C min⁻¹. This process was repeated twice for the same temperature range and at the same rates. The XRD patterns were measured using a Rigaku Mode 1 SmartLab apparatus utilizing Cu K α radiation at 40 kV and 30 mA at room temperature.

2.3. Results and discussion

Chemical structure of PNFR

The structural information of the PNFR was recorded using ^1H NMR (in CDCl_3), and the results are illustrated in Figure 2.2. Specific peaks at $\delta = 4.6$, 5.2-5.3, 6.5-6.8, and 7.5-7.8 ppm can be observed in the spectrum. The absorption peaks located at 7.5-7.8 ppm were attributed to the protons of the phenyl group of the PNFR, which originated from PPDC. The peaks at 6.5-6.8 ppm were assigned to the protons of the aromatic group of the PNFR, which originated from 4-aminophenol. In addition, the other peaks at 4.6 and 5.2-5.3 ppm were attributed to the chemical shifts of the $-\text{CH}_2-\text{O}-$ and $=\text{CH}_2$ groups, respectively, which indicated that the PNFR was successfully synthesized. Comparing the integral regions of the proton of the aromatic (6.5-6.8 ppm) groups with that of the $-\text{CH}_2-\text{O}-$ (4.6 ppm) groups, the number of repeating units in the PNFR obtained from the reaction between PPDC and 4-aminophenol was two.

Thermal degradation behavior of PNFR

The TGA curves of the PNFR in nitrogen and air atmosphere are illustrated in Figure 2.3. In air, the initial degradation of the PNFR (5 wt% loss) started at 300 °C. Then, sharp decomposition occurred from 300 to 450 °C, which suggested that flame-retarding effect could be imparted to polymers in this temperature region. When phosphorus-containing flame retardants generally decomposed at 300-450 °C, they form phosphorus-rich barriers on polymer surfaces and can prevent the heat and mass transfer from the polymer surface [35]. Above 600 °C in air, the additional decomposition of the PNFR via the subsequent oxidation of residual char occurred, owing to the presence of oxygen. The decomposition behavior of PNFR in nitrogen atmosphere was different from that in air. In nitrogen atmosphere, rapid degradation occurred at 300-450 °C after the initial decomposition at 293 °C, which was similar to the process observed in air. However, the percentage of residual char at 600 °C was 32 wt%, which was much lower than that obtained in air, 52.8%. Unlike the TGA experiment in air, no further degradation of the PNFR was observed at higher temperature in nitrogen atmosphere. As indicated by these results, the char formation by the

decomposition of the phosphorus-containing group of the PNFR should be catalyzed by the oxygen in air.

The thermal degradation behavior of PNFR was further confirmed using FTIR analyses. Using the thermal degradation stages of the PNFR during the TGA investigation, FTIR experiments were performed in the temperature range from room temperature to 500 °C, in air, as depicted in Figure 2.4. The decrease in the characteristic peak intensities at approximately 935 cm⁻¹ (P-N-C stretching) and 1,020 cm⁻¹ (P-O-C stretching) were observed above 300 °C. This suggested that the PNFR began to decompose at that temperature [36]. Also, the peak at 1,045 cm⁻¹, which corresponded to the stretching vibration of P-N-C completely disappeared above 375 °C. On the other hand, a new band at 982 cm⁻¹ could be observed as the temperature reached 400 °C and beyond. Considering that this band could be assigned to the P-O-P stretching vibration, phosphorus oxides, such as P₂O₅, P₄O₁₀ appeared to be generated during the thermal decomposition of the PNFR [37].

The flame-retarding mechanism of PNFRs is generally divided into gas- and condensed-phases. During the condensed-phase [24, 38-40], the thermal degradation of the flame retardant induces the generation of phosphoric acid, which promotes dehydration and liberates water during pyrolysis. Protective

char is then formed on the polymer surface during the decomposition of the flame retardant. This char could prevent the heat and mass transfer and further combustion. On the other hand, during the gas-phase, the active radicals ($\text{PO}\cdot$, $\text{PO}_2\cdot$, and $\text{HPO}\cdot$) generated by the decomposition of the flame retardant act as scavengers of hydrogen and hydroxyl radicals, which are required for combustion. In addition, gases, including H_2O and CO_2 , could be generated during the gas-phase. Inert gases, such as N_2 , could also be produced by the decomposition of nitrogen compounds. These generated gases could lead to the reduction in the O_2 concentration around the polymer.

After the combustion of the PNFR at $500\text{ }^\circ\text{C}$, expandable residual char was obtained, as illustrated in the inset of Figure 2.5a. The generation of volatile material, such as inert gas, from the nitrogen groups of the PNFR was thought to induce this bubble-shaped residual char during the combustion process. In addition, traces of many dense and coherent bubbles were observed in the SEM image of the char surface, which indicated that volatile gases were released during combustion (Figure 2.5a). As illustrated in the SEM-EDS spectrum, phosphorus-rich char surface was formed after combustion. While the phosphorus content of the PNFR calculated based on its chemical structure was 12.55 wt%, the phosphorus content of the char surface at $500\text{ }^\circ\text{C}$ obtained from the SEM-EDS spectrum was 13.38 wt%

(Figure 2.5b). Therefore, this could indicate that the PNFR contributed to the condensed flame retardant mechanism of phosphorus, which formed phosphorus-rich char on the surface of the polymer as well as the gas flame retardant mechanism of nitrogen, which produced inert gases during decomposition. This synergistic effect of phosphorus and nitrogen in the PNFR should enhance the flame retarding ability of the PNFR.

Thermal degradation behaviors of neat and flame-retarding PKs

TGA was used to evaluate the thermal stability and degradation processes of neat and flame-retarding PKs. The TGA curves in nitrogen and air atmosphere are illustrated in Figure 2.6. All decomposition temperatures obtained from the TGA experiments are summarized in Table 2.2. Here the temperature at 5% weight loss is taken as the initial decomposition temperature. In nitrogen atmosphere, PK-0 was decomposed in one step, and T_{initial} and T_{max} were 386 and 416 °C, respectively. The decrease in the initial decomposition temperature for the flame-retarding PKs was compared with that of PK-0. The T_{initial} of PK-7 decreased to 289 °C

compared with that of PK-3, which was 298 °C. These results were due to the low thermal stability of the phosphorus compound, as mentioned above [41-43]. Meanwhile, two characteristic decomposition stages were observed for all flame-retarding PKs at 250-350 °C and 350-500 °C. The first decomposition temperature ($T_{\max 1}$) was attributed to the phosphorus-containing groups, which decomposed at relatively low temperature, as already discussed when we analyzed the TGA results of the PNFR [44]. During the second decomposition stage ($T_{\max 2}$), the main degradation occurred. Although $T_{\max 2}$ of PK-7 was lower than that of PK-0, PK-7 generated a considerable amount of residual char compared to that of PK-0. This indicated that the decomposed phosphorus-containing groups could form a protective char layer on the surface of PK.

In air, an additional thermal oxidative decomposition process occurred above 500 °C. For example, PK-0 presented a two-step decomposition process, while the flame-retarding PKs exhibited three-step decomposition processes. These results were similar with the TGA results of the PNFR which were caused by the presence of oxygen in air. As illustrated in Table 2.2, the third decomposition temperature ($T_{\max 3}$) values of the PK samples relatively increased with the addition of the PNFR, suggesting that the PNFR delayed the combustion process in air by acting as excellent barrier

on the PK surface. Therefore, the PNFR was expected to prevent the spread of a large fire in air atmosphere.

The experimental and calculated amounts of residual char, according to the temperature (700 and 800 °C) in nitrogen and air atmosphere are summarized in Table 2.3. The data in Figure 2.6 and Table 2.3 indicate that the amount of residual char of the flame-retarding PKs was considerable at high temperature. This implied that the PNFR generated stable char layers on the surfaces of the PK samples. The amount of residual char of the flame-retarding PKs increased as the amount of PNFR increased. The theoretical amount of residual char for the flame-retarding PKs could be calculated using the amounts of residual char of PK-0 and PNFR obtained from the TGA experiments [45, 46]. The residual char amounts for the flame-retarding PKs were obtained using the following Equation (1):

$$(\text{FR residue} \times \text{FR ratio}) + (\text{PK residue} \times \text{PK ratio}) = \text{calculated residual char of flame-retarding PKs} \quad (1)$$

Where $\text{FR}_{\text{residue}}$ is the experimental PNFR residue, FR_{ratio} is the PNFR ratio of the flame-retarding PK, $\text{PK}_{\text{residue}}$ is the experimental PK-0 residue, and PK_{ratio} is the PK ratio of the flame-retarding PK. The Equation was used at two temperatures: 700 and 800 °C.

The data in Table 2.3 indicate that the experimental char residue quantities of all flame-retarding PKs were larger than the calculated ones at both temperatures regardless of the atmosphere. For example, in nitrogen, the measured residual char of PK-5 was 43.0 and 41.8 wt% at 700 and 800 °C, respectively. These values were 150-170% higher than the theoretical values. The measured residual char of PK-5 in air was also 150 and 15% higher than the theoretical values at 700 and 800 °C, respectively. While PNFR itself exhibited high residual char yields, it was found that PNFR can induce the formation of a relatively larger amount of char when it is applied to PK. Considering that one of key factors for the efficiency of flame retardants is its degree of interaction with polymer matrix, the PNFR in these results shows higher flame-retardant efficiency for PK. Therefore, it could be considered that the PNFR could act as char-forming agent for PK via the superior condensed-phase flame-retardant mechanism of phosphorus.

Flame retarding ability of neat and flame-retarding PKs

Both UL 94 VTM and LOI test are commonly conducted to demonstrate the flammability of polymers [47, 48]. For UL 94 VTM testing, all samples

were evaluated according to the ASTM D 4804 standard. The UL 94 VTM rating, dripping behavior, and time to self-extinguishing after ignition results were summarized in Table 2.1, and indicated that the introduction of the PNFR into PK delayed and further inhibited the combustion of PK. PK-0 was highly flammable and continued to burn up to the holding clamp. Moreover, PK-0 also exhibited heavy drips occurring ignition of cotton. Therefore, no rating was obtained for PK-0 during the vertical burning test. Similarly to PK-0, PK-3 was also not classified because it presented heavy drips and did not feature self-extinguishable properties. The self-extinguishable properties of PK-5 were observed within 10 s after the first and second ignition. Furthermore, no drips were noticed. Consequently, PK-5 achieved the VTM-0 rating. In addition, PK-7 was also completely self-extinguishable. For the LOI tests, all samples were investigated according to the ASTM D 2863 standard. The LOI values increased as the amount of added PNFR increased. For example, while the LOI value of PK-0 was 20.2%, that of PK-5 was increased to 23.8%. For PK-7, the LOI value was significantly increased to 25.9%. As indicated by these results, even relatively small amounts of PNFR imparted powerful flame-retarding ability to PK.

Morphology of residual char

To further demonstrate their char-forming capacities, the residual char of the neat and flame-retarding PKs was obtained via combustion at 600 °C in a furnace in air. The morphology of the residue was recorded using SEM and the results were illustrated in Figure 2.7. As presented in Figure 2.7a, the char layer of PK-0 was brittle, incompact, and presented many holes, which indicated that PK-0 was flammable. PK-3 also featured some holes and flaws which could allow the transfer of heat and mass. While inert gas bubble traces that were generated during the decomposition of PNFR were observed on the surface of the char layer, PK-3 was not perfectly flame-retarding owing to brittleness of the char layer. This was consistent with the results of the UL 94 VTM test, where PK-3 did not receive any rating. Compact and dense char layers were observed for the PK-5 and PK-7 samples, indicating that the flame-retardant effect occurred when the content of PNFR in the PNFR-PK systems exceeded 5 wt%. From these results, it was concluded that the PNFR formed stable char layers on the surface of PK during combustion. The formed char layer could inhibit heat and mass transfer, which suggested that could also prevent the spreading of fire.

Flame retarding mechanism of flame-retarding PKs

The mechanism responsible for the PNFR imparting flame retardancy to PK was evaluated using TGA and FTIR. After elevating the temperature to the required temperature using TGA in air, the chemical structures of the samples were characterized using FTIR. The FTIR spectra of PK-0 and PK-7 are illustrated in Figure 2.8. Distinct absorptions peaks were observed at 1,690, 1,410, 1,333, 1,504, 804, and 600 cm^{-1} in the FTIR spectrum of PK-0. The band at 1,690 cm^{-1} was attributed to the C=O bond stretching vibration. The stretching, wagging, and rocking modes of CH_2 were detected at 1,410, 1,333, 1,054, 804, and 600 cm^{-1} [49]. Moreover, the relative intensities of the above-mentioned peaks decreased above 325 °C, which suggested that PK began to decompose. As illustrated in Figure 2.8a, PK-0 was completely decomposed above 400 °C. The characteristic peak at 1,282 cm^{-1} in the FTIR spectra of PK-7 (Figure 2.8b) was ascribed to the stretching vibration of the P=O bond. The bands at 929 and 778 cm^{-1} were attributed to the P-N-C and P-O-C bond stretching vibrations, respectively. The distinct peaks decreased and disappeared above 275 °C, which indicated that the PNFR presented low thermal stability and began to decompose. New bands were

observed above 275 °C, and the band at 1,265 cm⁻¹ was attributed to the poly-phosphonate structure. These results indicated that the PNFR in the PK-PNFR systems was initially decomposed and formed phosphorus-rich char. Above 350 °C, characteristic absorption peaks were observed at 866 and 746 cm⁻¹. The band at 746 cm⁻¹ was ascribed to the poly-aromatic structure, and the peak at 866 cm⁻¹ was attributed to the P-N structure, which implied that a P-N structure was incorporated in the char layer [50, 51].

Melting behaviors and crystallizations of neat and flame-retarding PKs

To investigate the effects of the PNFR on the physical properties of PK, the melting behaviors of PK-0 and flame-retarding PKs were evaluated using DSC. The thermograms and DSC results are illustrated in Figure 2.9 and Table 2.4. Figure 2.9 depicts the second heating step. The crystallinity (X_c) values of the samples were calculated using the enthalpy of fusion (ΔH_f) of 100% crystalline PK, which was 227 J g⁻¹ [52, 53]. The melting temperature (T_m) and ΔH_f of PK-0 were 207.2 °C and 48.0 J g⁻¹, respectively. As PNFR was added to PK, the T_m and ΔH_f of the flame-retarding PKs decreased. The

decrease in T_m of the flame-retarding PKs with the addition of PNFR was attributed to PNFR acting as plasticizer in the PK matrix. The PNFR in the PK matrix could interfere with the intra- and/or inter-actions between the main chains of PK. Therefore, the degrees of intra- and/or inter-action between PK chains in the flame-retarding PKs system became relatively weak compared to that of PK-0. In addition, the decrease in X_c indicated that the PNFR could have destroyed the molecular arrangement of PK by disturbing the regular folding of the main chain of PK.

To further investigate the effect of the PNFR on the crystallization of PK, XRD analysis was conducted (Figure 2.10.) The PK-0 sample presented characteristic peaks at $2\theta = 22^\circ$, 26° , and 31° , which correspond to the reflections of the (100), (200), and (210) planes, respectively [54]. The XRD pattern of PK-0 presented three planes, which suggested that PK was a crystalline polymer. As the PNFR contents of the PK-PNFR samples increased, however, the characteristic peaks became increasingly weak. For PK-7, the (100) and (210) planes were even more difficult to observe, which indicated that the PNFR disturbed the crystallization of the PK chains and acted as plasticizer [53, 54].

2.4. Conclusion

A novel PNFR was synthesized and incorporated into PK. Prior to analyzing the neat and flame-retarding PKs, the decomposition process of the PNFR was investigated using TGA and FTIR. Above 375 °C, the decomposition of the P-O-C and P-N-C bonds and the appearance of the P-O-P bond were observed, which indicated that PNFR generated phosphorus complexes, such as P_2O_5 , P_4O_{10} , which catalyzed the formation of char. The required VTM-0 rating was obtained for the PK-7 sample because it was self-extinguishable within 10 s after ignition and presented no drips. The LOI value also increased from 20.2% for PK-0 to 25.9% for PK-7. As the PNFR contents of the PK-PNFR samples increased, the decrease in the $T_{initial}$ values was observed. However, the amount of residual char was significantly improved. The measured amount of residual char was also larger than the theoretical amount in both nitrogen and air atmosphere. When the residual char was investigated using SEM, the results indicated that PNFR imparted flame retarding ability to PK via an excellent condensed-phase flame-retarding mechanism. While the residual char of the PK-PNFR samples containing less than 3 wt% PNFR presented many holes,

which allowed the heat and mass transfer to continue, that of the samples containing more than 5 wt% PNFR was compact and dense. From evaluating the melting behaviors of the samples, the decrease in the T_m , ΔH_f , and X_c values was observed after incorporating PNFR into PK. Using these results, it was concluded that PNFR could act as a flame retardant and plasticizer for PK even at relatively low contents.

2.5. References

1. Bao, F., et al., *Synthesis of novel poly (phthalazinone fluorenyl ether ketone ketone) s with improved thermal stability and processability*. *Thermochimica Acta*, 2020. **683**: p. 178184.
2. Bong, S., et al., *Highly soluble polyimide based on asymmetric diamines containing trifluoromethyl group for high performance dielectric material*. *Macromolecular Research*, 2018. **26**(1): p. 85-91.
3. Melton, G.H., E.N. Peters, and R.K. Arisman, *Engineering thermoplastics*, in *Applied plastics engineering handbook*. 2011, Elsevier. p. 7-21.
4. Smaardijk, A. and E. Drent, *Polyketones: Aliphatic*. *Encyclopedia of Materials: Science and Technology*, 2011: p. 7194-7196.
5. Lagaron, J., et al., *Crystalline structure in aliphatic polyketones*. *Polymer*, 2000. **41**(8): p. 3011-3017.
6. Chatani, Y., et al., *Crystal structure of polyketone (1: 1 ethylene/carbon monoxide copolymer)*. *Journal of Polymer Science*, 1961. **55**(162): p. 811-819.
7. Jiang, Z. and A. Sen, *Palladium (II)-catalyzed isospecific alternating copolymerization of aliphatic. alpha.-olefins with carbon monoxide and isospecific alternating isomerization cooligomerization of a 1, 2-disubstituted olefin with carbon monoxide. Synthesis of novel, optically active, isotactic 1, 4-and 1, 5-polyketones*. *Journal of the American Chemical Society*, 1995. **117**(16): p. 4455-4467.
8. Jo, H., et al., *Effect of thermal aging on the change of interfacial*

- adhesion between polyketone cord and rubber by RFL primer treatment.* Textile Coloration and Finishing, 2018. **30**(2): p. 77-89.
9. Matsuo, T., *Fibre materials for advanced technical textiles.* Textile Progress, 2008. **40**(2): p. 87-121.
 10. Colquhoun, H.M., et al., *Dithioacetalisation of PEEK: a general technique for the solubilisation and characterisation of semi-crystalline aromatic polyketones.* Chemical Communications, 2007(32): p. 3365-3367.
 11. Lu, J., et al., *Morphology and fracture behavior in aliphatic polyketones.* Journal of Materials Science, 2000. **35**(2): p. 271-277.
 12. Ash, C., *Alternating olefin/carbon monoxide polymers: a new family of thermoplastics.* International Journal of Polymeric Materials, 1995. **30**(1-2): p. 1-13.
 13. Kalay, G. and M.J. Bevis, *The effect of shear controlled orientation in injection moulding on the mechanical properties of an aliphatic polyketone.* Journal of Polymer Science Part B: Polymer Physics, 1997. **35**(3): p. 415-430.
 14. Kato, A., et al., *Phase separation and mechanical properties of polyketone/polyamide polymer alloys.* Journal of Applied Polymer Science, 2010. **116**(5): p. 3056-3069.
 15. Rouhi, S., et al., *Using molecular dynamics simulations and finite element method to study the mechanical properties of nanotube reinforced polyethylene and polyketone.* Modern Physics Letters B, 2015. **29**(26): p. 1550155.
 16. Lommerts, B., E. Klop, and J. Aerts, *Structure and melting of perfectly alternating ethylene-carbon monoxide copolymers.* Journal

- of Polymer Science Part B: Polymer Physics, 1993. **31**(10): p. 1319-1330.
17. Lim, M.-Y., et al., *Effect of antioxidant grafted graphene oxides on the mechanical and thermal properties of polyketone composites*. European Polymer Journal, 2015. **69**: p. 156-167.
 18. Alaei, M., et al., *An overview of commercially used brominated flame retardants, their applications, their use patterns in different countries/regions and possible modes of release*. Environment International, 2003. **29**(6): p. 683-689.
 19. Levchik, S.V. and E.D. Weil, *Thermal decomposition, combustion and flame-retardancy of epoxy resins—a review of the recent literature*. Polymer International, 2004. **53**(12): p. 1901-1929.
 20. Gao, L.-P., et al., *A flame-retardant epoxy resin based on a reactive phosphorus-containing monomer of DODPP and its thermal and flame-retardant properties*. Polymer Degradation and Stability, 2008. **93**(7): p. 1308-1315.
 21. Hamalainen, C. and J.D. Guthrie, *Bromine-containing phosphonitrilates as flame retardants for cotton*. Textile Research Journal, 1956. **26**(2): p. 141-144.
 22. Ren, H., et al., *Synthesis and properties of a phosphorus-containing flame retardant epoxy resin based on bis-phenoxy (3-hydroxy) phenyl phosphine oxide*. Polymer Degradation and Stability, 2007. **92**(6): p. 956-961.
 23. Wang, Q., et al., *Synthesis of flame-retardant polypropylene/LDH-borate nanocomposites*. Macromolecules, 2013. **46**(15): p. 6145-6150.

24. Lu, S.-Y. and I. Hamerton, *Recent developments in the chemistry of halogen-free flame retardant polymers*. Progress in Polymer Science, 2002. **27**(8): p. 1661-1712.
25. Qian, L.-J., et al., *The non-halogen flame retardant epoxy resin based on a novel compound with phosphaphenanthrene and cyclotriphosphazene double functional groups*. Polymer Degradation and Stability, 2011. **96**(6): p. 1118-1124.
26. Nguyen, T., D. Hoang, and J. Kim, *Effect of ammonium polyphosphate and melamine pyrophosphate on fire behavior and thermal stability of unsaturated polyester synthesized from poly (ethylene terephthalate) waste*. Macromolecular Research, 2018. **26**(1): p. 22-28.
27. Li, Y., K. Liu, and R. Xiao, *Preparation and characterization of flame-retarded polyamide 66 with melamine cyanurate by in situ polymerization*. Macromolecular Research, 2017. **25**(8): p. 779-785.
28. Leu, T.S. and C.S. Wang, *Synergistic effect of a phosphorus–nitrogen flame retardant on engineering plastics*. Journal of Applied Polymer Science, 2004. **92**(1): p. 410-417.
29. Jiang, P., et al., *Synthesis, characterization, and utilization of a novel phosphorus/nitrogen-containing flame retardant*. Industrial & Engineering Chemistry Research, 2015. **54**(11): p. 2974-2982.
30. Yang, S., et al., *Synthesis of a phosphorus/nitrogen-containing additive with multifunctional groups and its flame-retardant effect in epoxy resin*. Industrial & Engineering Chemistry Research, 2015. **54**(32): p. 7777-7786.
31. Sun, S., et al., *Flammability characteristics and performance of*

- halogen-free flame-retarded polyoxymethylene based on phosphorus–nitrogen synergistic effects*. Journal of Applied Polymer Science, 2010. **118**(1): p. 611-622.
32. Kiuchi, Y., et al., *Flame-retarding polylactic-acid composite formed by dual use of aluminum hydroxide and phenol resin*. Polymer Degradation and Stability, 2014. **109**: p. 336-342.
33. Li, B. and M. Xu, *Effect of a novel charring–foaming agent on flame retardancy and thermal degradation of intumescent flame retardant polypropylene*. Polymer Degradation and Stability, 2006. **91**(6): p. 1380-1386.
34. Wang, C., et al., *Flame-retardant rigid polyurethane foam with a phosphorus-nitrogen single intumescent flame retardant*. Polymers for Advanced Technologies, 2018. **29**(1): p. 668-676.
35. Chen, L., et al., *A new intumescent flame retardant containing phosphorus and nitrogen: Preparation, thermal properties and application to UV curable coating*. Progress in Organic Coatings, 2011. **70**(1): p. 59-66.
36. Zhang, P., et al., *Flame retardancy and hydrolysis resistance of waterborne polyurethane bearing organophosphate moieties lateral chain*. Progress in Organic Coatings, 2015. **89**: p. 170-180.
37. Gavgani, J.N., H. Adelnia, and M.M. Gudarzi, *Intumescent flame retardant polyurethane/reduced graphene oxide composites with improved mechanical, thermal, and barrier properties*. Journal of Materials Science, 2014. **49**(1): p. 243-254.
38. Liao, F., et al., *A novel efficient polymeric flame retardant for poly (lactic acid)(PLA): synthesis and its effects on flame retardancy and*

- crystallization of PLA*. *Polymer Degradation and Stability*, 2015. **120**: p. 251-261.
39. Levchik, S.V. and E.D. Weil, *Flame retardancy of thermoplastic polyesters—a review of the recent literature*. *Polymer International*, 2005. **54**(1): p. 11-35.
 40. Lin, H., L. Han, and L. Dong, *Thermal degradation behavior and gas phase flame-retardant mechanism of polylactide/PCPP blends*. *Journal of Applied Polymer Science*, 2014. **131**(13).
 41. Liu, Y.L., et al., *Phosphorus-containing epoxy for flame retardant. I. Synthesis, thermal, and flame-retardant properties*. *Journal of Applied Polymer Science*, 1996. **61**(4): p. 613-621.
 42. Wang, T.S., J.K. Parng, and M.D. Shau, *The synthesis and properties of new epoxy resin containing phosphorus and nitrogen groups for flame retardancy*. *Journal of Applied Polymer Science*, 1999. **74**(2): p. 413-421.
 43. Liu, Y.L., *Flame-retardant epoxy resins from novel phosphorus-containing novolac*. *Polymer*, 2001. **42**(8): p. 3445-3454.
 44. Costes, L., et al., *Cellulose/phosphorus combinations for sustainable fire retarded polylactide*. *European Polymer Journal*, 2016. **74**: p. 218-228.
 45. Wang, X., et al., *Comparative study of the synergistic effect of binary and ternary LDH with intumescent flame retardant on the properties of polypropylene composites*. *RSC Advances*, 2015. **5**(96): p. 78979-78985.
 46. Wei, L.-L., et al., *Effect of a phosphorus-containing flame retardant on the thermal properties and ease of ignition of poly (lactic acid)*.

- Polymer Degradation and Stability, 2011. **96**(9): p. 1557-1561.
47. Du, L., B. Qu, and Z. Xu, *Flammability characteristics and synergistic effect of hydrotalcite with microencapsulated red phosphorus in halogen-free flame retardant EVA composite*. Polymer Degradation and Stability, 2006. **91**(5): p. 995-1001.
 48. Cullis, C. and M. Hirschler, *Char formation from polyolefins. Correlations with low-temperature oxygen uptake and with flammability in the presence of metal halogen systems*. European Polymer Journal, 1984. **20**(1): p. 53-60.
 49. Ataollahi, N., et al., *A polyketone-based anion exchange membrane for electrochemical applications: synthesis and characterization*. Electrochimica Acta, 2017. **226**: p. 148-157.
 50. Sun, Z., et al., *Effect of additive phosphorus-nitrogen containing flame retardant on char formation and flame retardancy of epoxy resin*. Materials Chemistry and Physics, 2018. **214**: p. 154-164.
 51. Gao, F., L. Tong, and Z. Fang, *Effect of a novel phosphorous–nitrogen containing intumescent flame retardant on the fire retardancy and the thermal behaviour of poly (butylene terephthalate)*. Polymer Degradation and Stability, 2006. **91**(6): p. 1295-1299.
 52. Gupta, P., et al., *Development of high-strength fibers from aliphatic polyketones by melt spinning and drawing*. Journal of Applied Polymer Science, 2001. **82**(7): p. 1794-1815.
 53. Li, S., et al., *Nanoscale morphology, interfacial hydrogen bonding, confined crystallization and greatly improved toughness of polyamide 12/polyketone blends*. Nanomaterials, 2018. **8**(11): p. 932.

54. Waddon, A. and N. Karttunen, *Poly (olefin ketone) s: Comparison of the Effects of CH₃ and CH₃CH₂ Side Groups on the Crystal Structure*. *Macromolecules*, 2002. **35**(10): p. 4003-4008.

Table 2.1. Composition and flame-retarding properties of neat polyketone (PK) and flame-retarding PKs featuring different phosphorus-nitrogen flame retardant (PNFR) contents

Samples	PK (wt%)	PNFR (wt%)	UL 94 rating	After flame time (s)	Ignition of cotton	LOI (%)
PK-0	100	-	N.C.	-	Y	20.2
PK-3	97	3	N.C.	-	Y	22.1
PK-5	95	5	VTM-0	≤10 (3s)	N	23.8
PK-7	93	7	VTM-0	≤10 (3s)	N	25.9

Note: Here UL 94 VTM is the thin material vertical burning test and LOI is the limiting oxygen index. Abbreviation: N.C., not classified.

Table 2.2. Thermogravimetric analysis data of neat and flame-retarding polyketones (PKs) in nitrogen and air atmosphere; here, PK-0, PK-3, PK-5, and PK-7 represent PK-phosphorus-nitrogen flame retardant (PNFR) systems that contain 0, 3, 5, and 7 wt% PNFR, respectively, while T_{initial} , T_{max1} , T_{max2} , and T_{max3} are the initial, first, second, and third decomposing temperatures, respectively

Samples	N ₂			Air			
	T_{initial} (°C)	T_{max1} (°C)	T_{max2} (°C)	T_{initial} (°C)	T_{max1} (°C)	T_{max2} (°C)	T_{max3} (°C)
PK-0	386	-	416	350	-	416	553
PK-3	298	317	418	297	313	413	645
PK-5	295	309	418	293	304	409	650
PK-7	289	305	412	292	301	399	676

Table 2.3. Experimental (thermogravimetric analysis-determined) and calculated residual char of neat and flame-retarding polyketones (PKs) in nitrogen and air atmosphere; here, PK-0, PK-3, PK-5, and PK-7 represent PK-phosphorus-nitrogen flame retardant (PNFR) systems that contain 0, 3, 5, and 7 wt% PNFR, respectively

Samples	N ₂				Air			
	700 °C		800 °C		700 °C		800 °C	
	Exp.	Cal.	Exp.	Cal.	Exp.	Cal.	Exp.	Cal.
PNFR	30.4	-	27.8	-	42.3	-	13.2	-
PK-0	16.5	-	14.8	-	2.8	-	2.8	-
PK-3	39.0	16.9	37.8	15.2	8.1	4.0	2.9	3.1
PK-5	43.0	17.2	41.8	15.4	12.2	4.8	3.8	3.3
PK-7	44.3	17.5	43.3	15.7	22.8	5.6	3.8	3.5

Table 2.4. Differential scanning calorimetry results of neat and flame-retarding polyketones (PKs), where PK-0, PK-3, PK-5, and PK-7 represent PK-phosphorus-nitrogen flame retardant (PNFR) systems that contain 0, 3, 5, and 7 wt% PNFR, respectively, while T_m , ΔH_f , and X_c are the melting temperature, enthalpy of fusion, and crystallinity, respectively ($\Delta H_{f100\%}$ is 100% crystalline of polyketone, 227 J g⁻¹)

Samples	T_m (°C)	ΔH_f (J g⁻¹)	X_c (%)
PK-0	207.2 (± 3.8)	48.0 (± 3.4)	20.4
PK-3	182.3 (± 1.4)	20.9 (± 0.8)	9.8
PK-5	163.2 (± 0.9)	16.4 (± 1.5)	8.9
PK-7	148.1 (± 2.3)	8.9 (± 0.7)	6.0

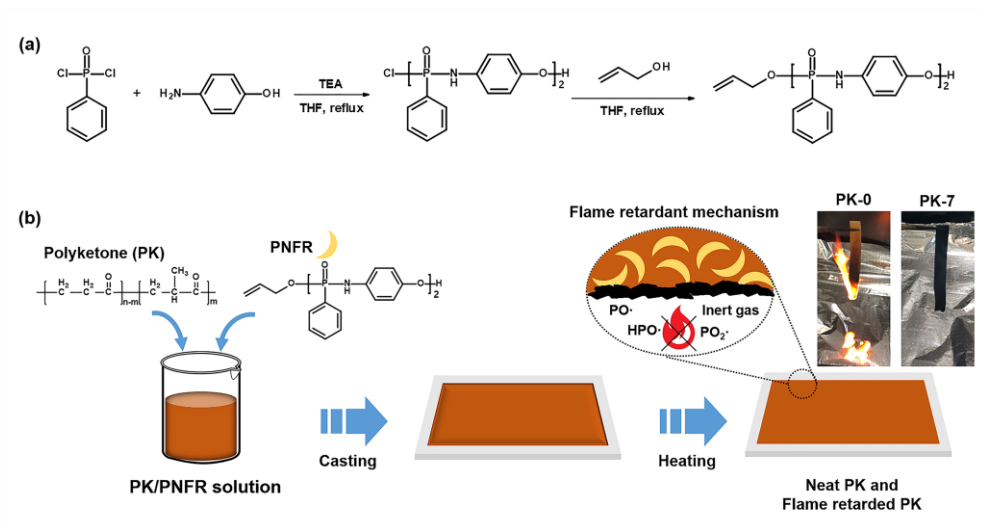


Figure 2.1. Schematics for (a) synthesis of phosphorus-nitrogen flame retardant (PNFR) and (b) preparation of neat and flame-retarding polyketones (PKs) via solution casting. Here TEA and THF are triethylamine and tetrahydrofuran, respectively, while PK-0 and PK-7 are pure PK and PK-PNFR containing 93 wt% PK and 7 wt% PNFR, respectively

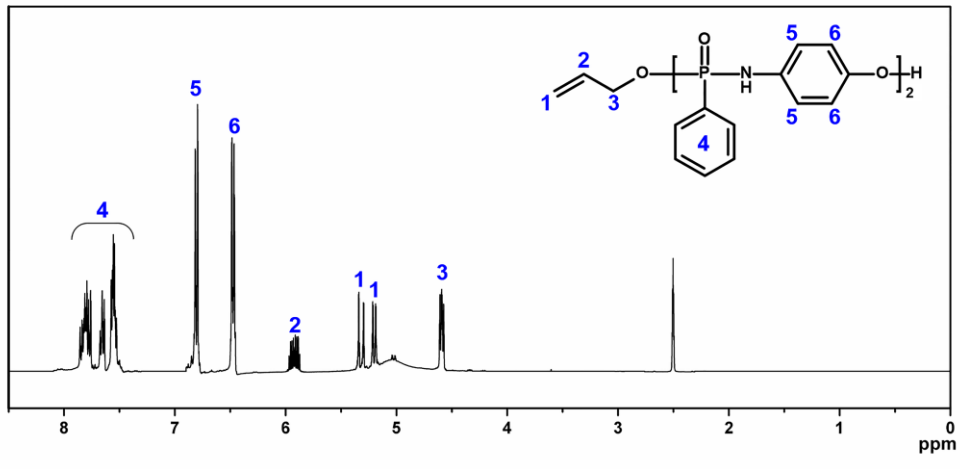


Figure 2.2. ¹H nuclear magnetic resonance spectrum of phosphorus-nitrogen flame retardant

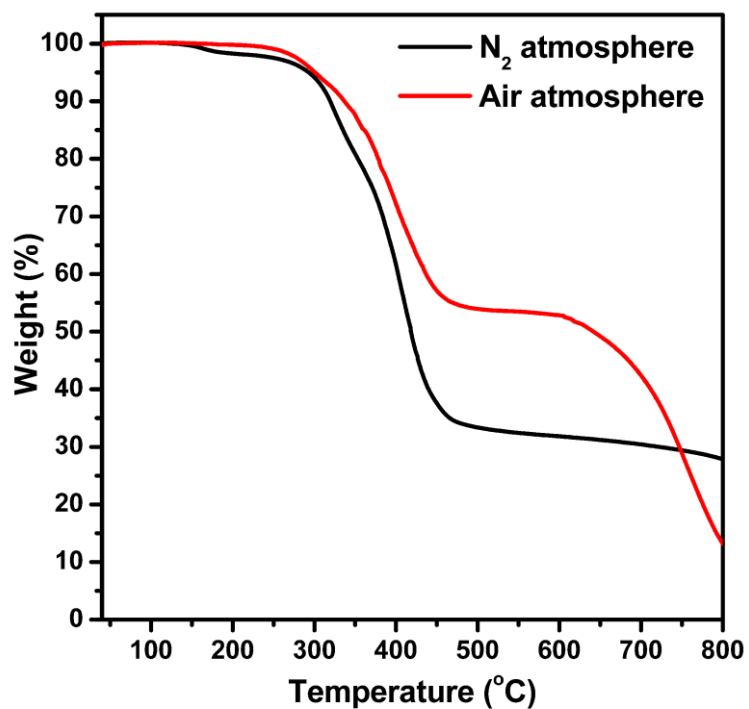


Figure 2.3. Thermogravimetric analysis curves of phosphorus-nitrogen flame retardant in nitrogen and air atmosphere

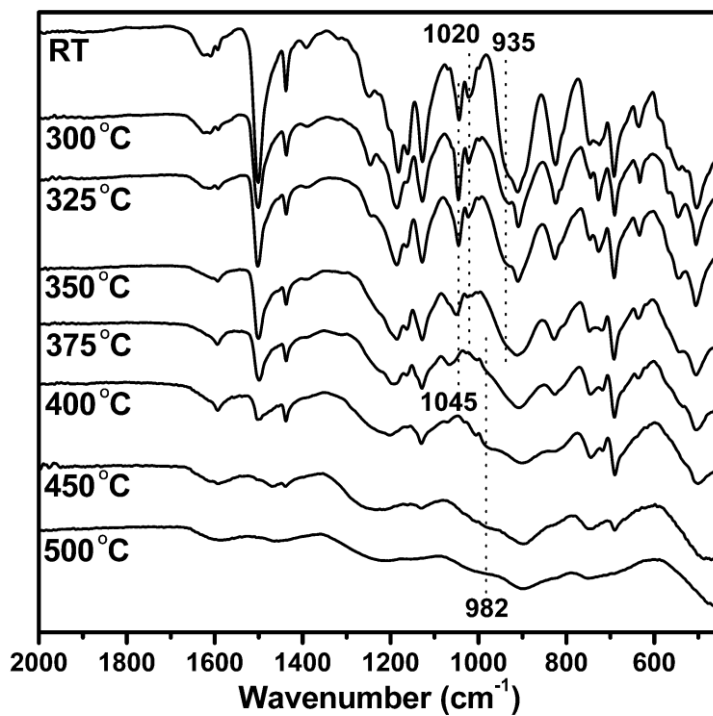


Figure 2.4. Fourier-transform infrared spectra of phosphorus-nitrogen flame retardant in the 25-500 °C temperature range in air atmosphere

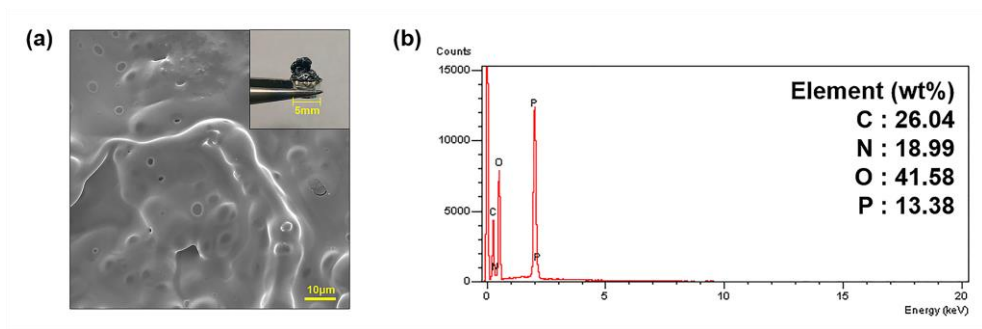


Figure 2.5. (a) Scanning electron microscopy (SEM) image and (b) SEM-energy dispersive X-ray spectroscopy results of residual char after combustion of phosphorus-nitrogen flame retardant. Inset in (a) is a digital photograph of residual char

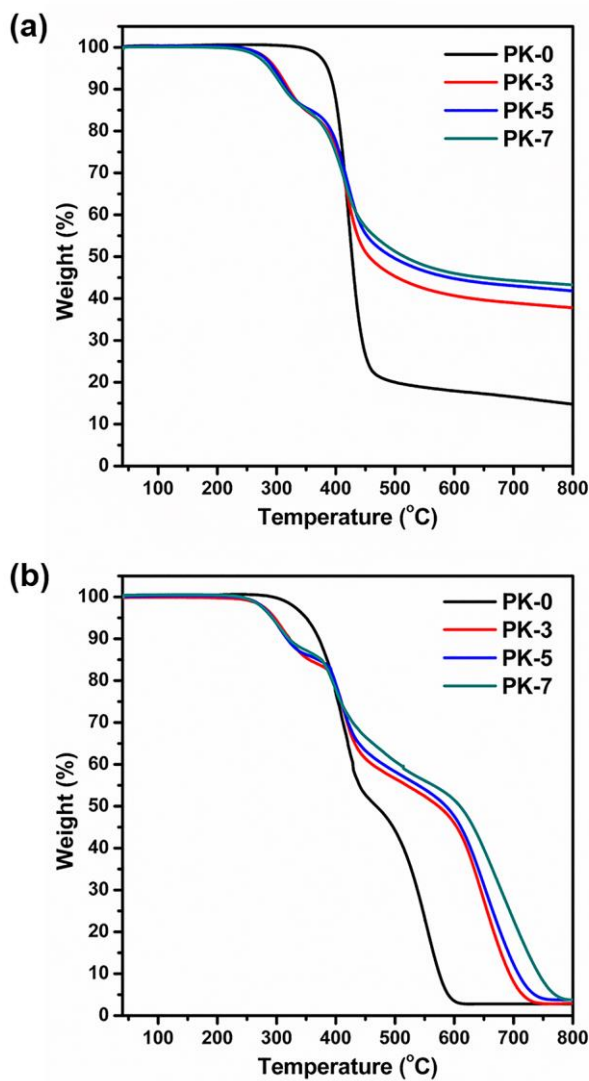


Figure 2.6. Thermogravimetric analysis curves of neat and flame-retarding polyketones (PKs) in (a) nitrogen and (b) air atmosphere; where PK-0, PK-3, PK-5, and PK-7 represent PK-phosphorus-nitrogen flame retardant (PNFR) systems that contain 0, 3, 5, and 7 wt% PNFR, respectively

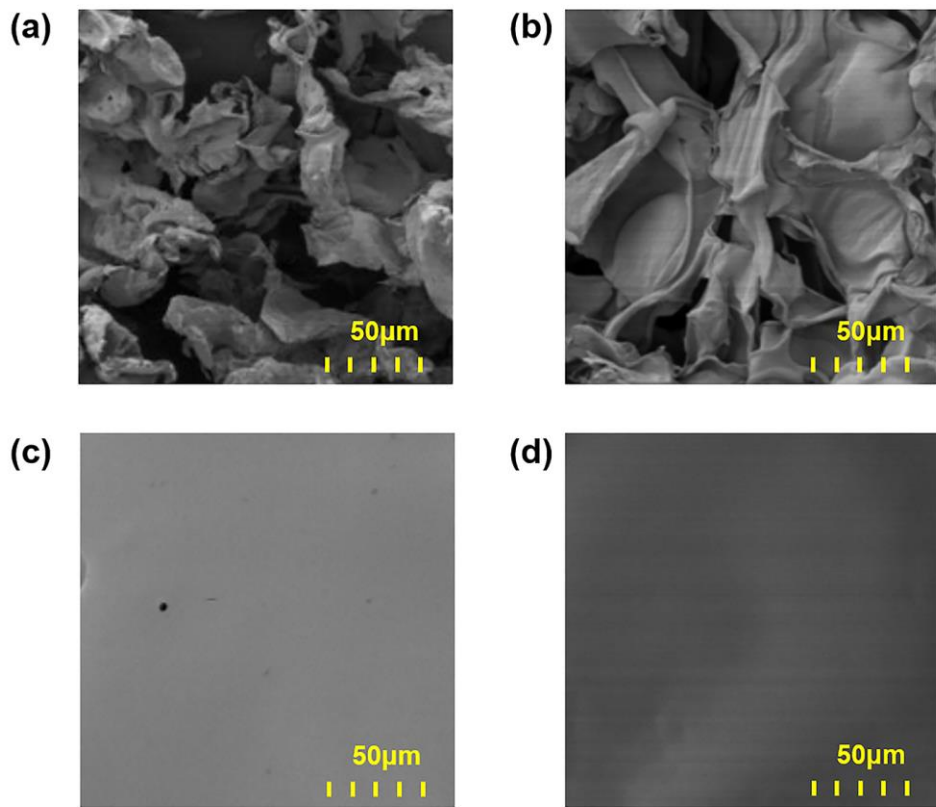


Figure 2.7. Scanning electron microscopy images of residual char from (a) PK-0, (b) PK-3, (c) PK-5, and (d) PK-7, where PK-0, PK-3, PK-5, and PK-7 represent PK-phosphorus-nitrogen flame retardant (PNFR) systems that contain 0, 3, 5, and 7 wt% PNFR, respectively

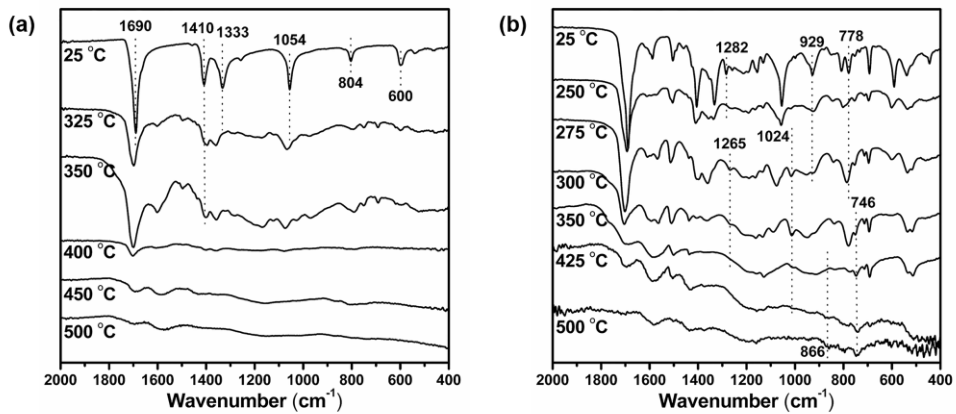


Figure 2.8. Fourier-transform infrared spectra of (a) PK-0 and (b) PK-7 in the 25-500 °C temperature range in air

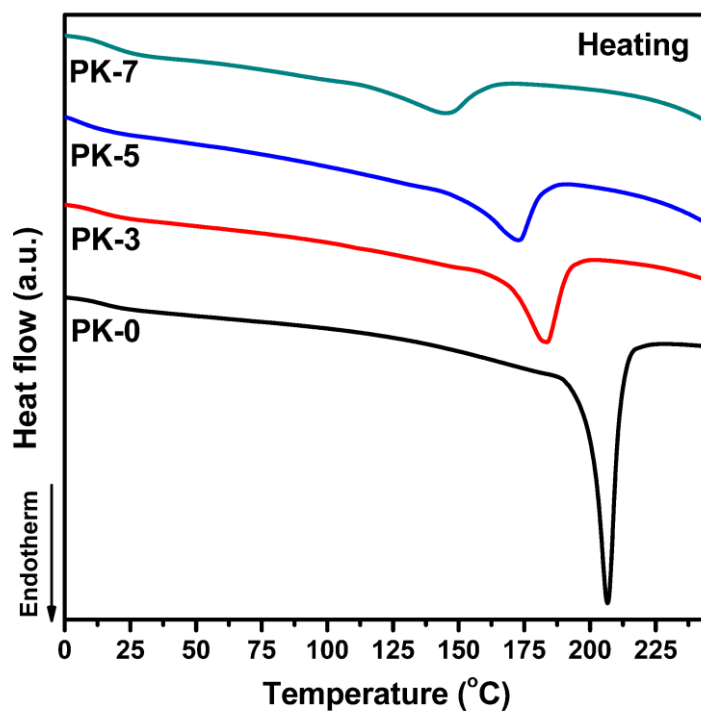


Figure 2.9. Differential scanning calorimetry thermograms of neat and flame-retarding polyketones (PKs), where PK-0, PK-3, PK-5, and PK-7 represent PK-phosphorus-nitrogen flame retardant (PNFR) systems that contain 0, 3, 5, and 7 wt% PNFR, respectively

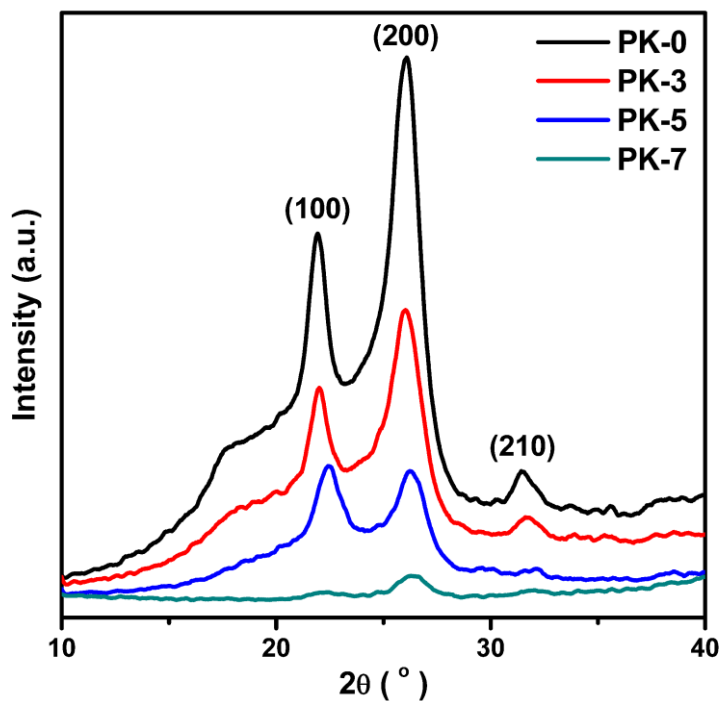


Figure 2.10. X-ray diffraction patterns of neat and flame-retarding PKs, where PK-0, PK-3, PK-5, and PK-7 represent PK-phosphorus-nitrogen flame retardant (PNFR) systems that contain 0, 3, 5, and 7 wt% PNFR, respectively

Chapter 3

**Enhancement of flame retardancy and
physical property for poly(vinyl chloride)
having renewable cardanol-based self-
polymerizable phosphonate under heat
treatment process**

3.1. Introduction

Poly(vinyl chloride) (PVC) is one of the most common thermoplastic polymers used in a wide range of applications such as pipes, food packaging, wire, and cables [1, 2]. Neat PVC is a rigid and brittle polymer with high glass transition temperature and low thermal stability attributing to the presence of chlorine atoms [3]. To overcome these disadvantages of neat PVC, plasticizers are generally used to enhance its flexibility, softness, and processability [4, 5]. The commonly used plasticizers for PVC are the diesters of phthalic acid, phthalates, e.g. dibutyl phthalate, and dioctyl phthalate [6, 7]. While phthalate-type plasticizers impart superior plasticizing effect to PVC, they are toxic and harmful to the environment [8]. Accordingly, plasticizers derived from renewable resources have gained significant scientific attention because of their non-toxicity, renewable raw materials, and environmental friendliness [9, 10]. However, as these bio-based plasticizers as well as phthalate-type plasticizers are vulnerable to heat or flame and can lead to the spreading of fire [11], their flame retardancy applications are restricted to plasticized PVCs. Therefore, to ameliorate the flammability of plasticized PVCs, it is essential to develop

environmentally friendly additives with flame retardancy.

To impart flame retardancy to polymers, one of the conventional methods is to add flame retardants with halogen, phosphorus, or inorganic compounds to their matrices [12-15]. However, flame retardants such as brominated-flame retardants, which are mainly used for fire safety, are regulated and banned in many countries as they generate substances toxic to both humans and the environment during the combustion process [16-19]. Because of these drawbacks of halogen flame retardants, other flame retardants containing phosphorus have been investigated [20]. Recently, various studies on phosphorus-containing flame retardants prepared from renewable resources such as eugenol [21, 22], vanillin [23], and cardanol [24, 25] have been reported. Among these renewable resources, functional additives using cardanol which is extracted from cashew nut shell liquid have been extensively investigated because of their unique chemical structure with a hydroxyl group and long alkyl chain including double bonds. This structure can be used to design structurally diverse molecules [24, 26]. However, only a few reports are available on cardanol-based additives that impart flame retardancy and plasticizing effect into PVCs.

Herein, we described a bio-based flame-retardant plasticizer, bis(cardanyl) phenylphosphonate (CP), which simultaneously acts as a

flame retardant and plasticizer for PVC. It was demonstrated that the phosphonate groups and long alkyl chains of CP enhanced the flame retardancy and flexibility of PVC, respectively. In contrast to the previously reported flame retardants, the PVC-CP system in this study exhibited self-polymerization by heat treatment and showed remarkable abilities for suppressing melt-drips and forming stable graphitized char, improving the flame retardancy of PVC without significantly reducing its flexibility.

3.2. Experimental

Materials

Cardanol was provided by Biochempia (Korea) and was used as received. PVC ($M_w \sim 43,000 \text{ g mol}^{-1}$, $M_n \sim 22,000 \text{ g mol}^{-1}$, inherent viscosity 0.51 dL g^{-1}), phenylphosphonic acid, and *N,N'*-dicyclohexylcarbodiimide (DCC) were purchased from Sigma-Aldrich. 4-Dimethylaminopyridine (DMAP) was purchased from TCI. Tetrahydrofuran (THF), ethyl acetate (EA), *N,N*-dimethylformamide (DMF), n-hexane, and magnesium sulfate (MgSO_4) were purchased from Daejung chemical & metals. All the other reagents and solvents were used without further purification.

Synthesis of bis(cardanyl) phenylphosphonate (CP)

CP was synthesized as follows: In a round-bottomed flask, cardanol (0.189 mol) was dissolved in DMF with magnetic stirring. Then, a mixture of phenylphosphonic acid (0.063 mol) and DMAP (9.45 mmol) dissolved in DMF was added dropwise into the flask over 1.5 h. After that, DCC was

immediately added dropwise into the flask. The reaction was carried out in an ice bath. The ice bath was removed after the addition of DCC, and the reaction was carried out for another 4 h at room temperature. After the completion of the reaction, the solution was washed with distilled water for 2–3 times. At this time, EA was used to extract the organic solution layer. The organic solution was then dried with anhydrous MgSO_4 . After removing the EA using a rotary evaporator, the crude product was dried under vacuum. The crude product was purified on silica gel using n-hexane/EA (10/1) as the eluent to yield CP as a yellow liquid (45%).

Preparation of flame-retarded PVCs (PVC films, X-PVC films)

The neat and flame-retarded PVCs were prepared as follows. PVC films were prepared via a solution casting method as follows: 20 g PVC was dissolved in 80 g THF. Then, to prepare the PVC films containing 0, 5, 7, and 10 wt% CP, different amounts of CP were added to the PVC solution (Table 3.1). After mixing for 1 h, the solutions were poured into glass molds and dried at room temperature overnight. Thereafter, the samples were dried

at 40 °C in vacuum to remove the solvent completely. The PVC films containing 0, 5, 7, and 10 wt% CP were labeled as PVC-0, PVC-5, PVC-7, and PVC-10, respectively.

To confirm whether the crosslinking network has an effect on the flame retardancy of PVC, cross-linked PVC (X-PVC) films were prepared. The X-PVC films were obtained via the thermo-crosslinking of CP in the PVC film as follows: each PVC film in a mold was heated at 120 °C for 1 h using a hot plate. The heat-treated PVC films were denoted as X-PVC-#, where # represents the amount of CP.

Characterization

The Fourier transform infrared (FTIR) spectra were obtained using a Bruker Alpha-Platinum attenuated total reflectance (ATR)-FTIR spectrometer over the wavenumber range of 4000–400 cm^{-1} . ^1H Nuclear magnetic resonance (^1H NMR) analysis was performed on a Bruker AVANCE-400MHz NMR spectrometer using CDCl_3 as the solvent. ^{31}P Nuclear magnetic resonance (^{31}P NMR) analysis was conducted using a Bruker AVANCE-500MHz NMR spectrometer. The transmittance of the

films was measured using a MECASYS Optizen UV-Vis spectrometer over the wavelength range of 400–700 nm. The samples had the dimensions of 20 mm × 8 mm × 1 mm. Thermogravimetric analysis (TGA) was carried out on a Perkin Elmer TGA 4000 instrument. The TGA experiment was performed from room temperature to 700 °C at a heating rate of 10 °C min⁻¹ under N₂. The morphology of the residual char was observed using a JEOL JSM-7601F PLUS field emission scanning electron microscope (FE-SEM). All the samples were coated with platinum. The phosphorus content of the residual char surface and dispersion of the additives were measured using a SEM-energy dispersive X-ray spectrometer (SEM-EDS). The chemical structure of the films was analyzed using TGA and FTIR. The samples were heated to the required temperature by TGA under an air atmosphere. Then, the chemical structure of the samples was recorded using an FTIR spectrometer. The limiting oxygen index (LOI) of the samples was determined using an FESTECC FT-LOI-404 LOI tester according to ASTM D2863 standard. The sample size was 120 mm × 15 mm × 3 mm. To perform the additional flame retardant test, a vertical burning test (UL-94 V test) was conducted according to ASTM D3801. Raman spectroscopy measurements were performed on Thermo Fisher DXR2xi at room temperature using a 532 nm laser line. The melting behavior of the films

was evaluated via differential scanning calorimetry (DSC). All the DSC experiments were carried out under a N₂ atmosphere using a Discovery DSC 25. The samples were heated from -20 to 150 °C at a heating rate of 10 °C min⁻¹. In addition, the crosslinking reaction of the samples was also investigated using DSC. The samples were heated to the required temperature at a heating rate of 10 °C min⁻¹. The X-ray diffraction (XRD) patterns were recorded on a Malvern Panalytical Empyrean diffractometer utilizing Cu K α radiation. The tensile test was performed using a QM100S universal testing machine (UTM) with a crosshead speed of 10 mm min⁻¹. The test was performed according to ASTM D638 standard at room temperature. Five samples (thickness: 0.3 mm) were analyzed for each film. The migration stability of the samples was measured in n-hexane or distilled water at room temperature. The samples (15 mm \times 15 mm \times 1 mm) were immersed in 20 mL n-hexane or distilled water and shaken occasionally. At various time intervals, 0.5 mL of the solvent was withdrawn and diluted in 2.5 mL n-hexane or distilled water. The migration behavior of the samples was analyzed by using an ultraviolet-visible (UV-Vis) spectrometer at 265 nm. Each type of sample was tested three times. Gel permeation chromatography (GPC) was performed on an Agilent Technologies 1260 infinity GPC system equipped with a 1260 refractive index detector.

Calibration was conducted using monodispersed polystyrene standards. THF was used as the solvent. The dispersion of chlorine or phosphorus atom was investigated using Tecnai G2 F30 S-Twin transmission electron microscope-energy dispersive X-ray spectroscopy (TEM-EDS). Samples were embedded in epoxy resin at 60 °C for 48 h, and then cut with Leica EM UC7 ultramicrotome. The sections with 150 nm in thickness were deposited on Cu grids for TEM-EDS.

3.3. Results and discussion

The bis(cardanyl) phenylphosphonate (CP) designed and synthesized in this study consisted of a phosphonate group and long alkyl chain, which are anticipated to improve the flame retardancy and flexibility of PVC, respectively (Figure 3.1). To verify the chemical structure of CP, FTIR measurements were conducted (Figure 3.2a and Table 3.2). Common specific vibrations corresponding to =C-H stretching of unsaturated hydrocarbons (3010 cm^{-1}), C-H stretching of aliphatic chains (2923 and 2854 cm^{-1}), and C=C stretching of aromatic groups (1590 and 1456 cm^{-1}) were observed in the spectra of both cardanol and CP. In the case of CP, the peaks at 3350 and 1348 cm^{-1} ascribed to the vibration of O-H disappeared. In addition, the vibration attributing to P-O-C stretching (960 cm^{-1}) and P=O stretching (1132 and 522 cm^{-1}) of aryl phosphonate were observed, indicating the successful occurrence of the condensation reaction between cardanol and phenylphosphonic acid. The ^1H NMR spectra clearly showed the chemical structure of cardanol and CP, as shown in Figure 3.2b. The peaks located at $0.8\text{--}2.9\text{ ppm}$ and $4.9\text{--}5.9\text{ ppm}$ were observed in the ^1H NMR spectra of both cardanol and CP. These peaks corresponded to the

protons of the saturated and unsaturated hydrocarbons in the alkyl chain, respectively. Meanwhile, the signals of aromatic protons of cardanol at 6.6–6.8 ppm shifted to 6.9–7.0 ppm in the ^1H NMR spectrum of CP. In addition, the peaks at 7.8–8.0 ppm, which originated from phenylphosphonic acid, were observed in the aromatic protons of CP. The cardanol:phenylphosphonic acid reaction ratio of 2:1 was obtained using the integral area ratio of *the a' and e peaks*. From the ^{31}P NMR spectrum of CP, a new chemical shift was confirmed at 9.42 ppm, and no peaks corresponds to phenylphosphonic acid (Figure 3.2c and Figure 3.2d), demonstrating that CP was successfully synthesized.

Then, CP was introduced into PVC via a simple solution casting method to evaluate its effect on physical properties and flame retardancy of PVC. The resulting PVC films were labeled as PVC-#, where # represents the weight percentage of CP (Table 3.1). It is widely known that the degree of dispersion of additives in a polymer plays an important role in improving its flame retardancy and physical properties [27-30]. Yuan et al. reported that PMMA composites with relatively well-dispersed nanotubes shows lower heat release rate than PMMA composites with poor dispersion [31]. Thus, the transparency of all the PVC films was examined using a UV-Vis spectrometer in the visible range (400–700 nm) because the flame

retardancy and mechanical properties of PVC could be affected by the degree of dispersion of the CP in it. As shown in Figure 3.3, all the PVC films exhibited a high transmittance of more than 85% at 600 nm. Even the transmittance of PVC-10 was 88%, which is only 2% lower than that of PVC-0 (90%). In addition, in Figure 3.3, the text under all the PVC films is clearly shown, implying that the PVC-# films prepared in this study contained relatively well-dispersed CP. Further, SEM-EDS and TEM-EDS could demonstrate the degree of dispersion of the CP in PVC (Figure 3.4 and Figure 3.5). Mapping was performed on the Cl or P atom to confirm the degree of dispersion of the CP. PVC-10 exhibited the well-dispersed Cl and P atoms without agglomerate in both SEM-EDS and TEM-EDS analyses, identifying CP was uniformly dispersed in PVC film.

To investigate the effect of CP on the thermal decomposition behavior of PVC, the TGA of the PVC films was carried out in a N₂ atmosphere, and the corresponding results are summarized in Table 3.3. As can be observed from Figure 3.6 and Figure 3.7, PVC-0 degraded via a two-step process, which is known to be the general thermal decomposition behavior of conventional PVC [32-34]. The first decomposition stage below 380 °C could mainly be attributed to the loss of HCl by the dehydrochlorination of PVC [35]. In the second decomposition stage at around 400–500 °C, the conjugated polyene

structure in PVC, which was formed during the previous dehydrochlorination process, degraded into aromatic compounds and hydrocarbon complexes [36]. All the PVC films containing CP showed thermal decomposition behavior similar to that of PVC-0, while they showed relatively higher thermal stability than PVC-0. For example, $T_{5\%}$ and $T_{50\%}$ of PVC-0 were 224 and 318 °C, respectively, whereas those for PVC-10 were 273 and 345 °C, respectively, indicating that the introduction of CP with the phosphonate structure improved the thermal stability of the PVC films.

To confirm the effect of the phosphonate group in CP on the formation of the residual char, the morphology of residual char was observed using the SEM after the combustion of the PVC films, as shown in Figure 3.8. While the residual char of PVC-0 showed a fractured structure with many voids and holes, which could easily transfer heat during combustion, the PVC films containing CP showed relatively dense and compact residual char, which prevented the transfer of heat, oxygen, and volatiles generated by the decomposition of the polymer. From the additional SEM-EDS analyses, it was found that the remaining content of phosphorus in the residual char increased with an increase in the CP content in the PVC films (Table 3.3). When the amount of CP increased from 5 to 10 wt%, the phosphorus

content in the residual char increased to 2.75 wt% for PVC-10 from 1.04 wt% for PVC-5.

For a more detailed study on the role of CP in PVC films during the initial thermal decomposition process, the chemical structures of PVC-0 and PVC-10 at different temperatures were analyzed using TG-FTIR (Figure 3.9 and Table 3.4). For PVC-0, the characteristic vibrations of -CH stretching (2978 cm^{-1}), CH_2 asymmetric stretching (2911 and 2853 cm^{-1}), CH_2 wagging (1426 and 1252 cm^{-1}), and C-Cl stretching (692 cm^{-1}) were observed (Figure 3.9a) [37, 38]. The intensity of these characteristic peaks decreased with an increase in temperature. From this decrease, the decomposition processes of PVC could be followed. For example, the peak at around 692 cm^{-1} assigned to the C-Cl bond disappeared at $350\text{ }^\circ\text{C}$, indicating that the complete dehydrochlorination of PVC-0 occurred during the first thermal decomposition stage. PVC-10 exhibits a thermal decomposition behavior similar to that of PVC-0, and some differences could be observed at temperatures higher than $300\text{ }^\circ\text{C}$. As shown in Figure 3.9b, the peaks corresponding to the P=O stretching vibration (1132 cm^{-1}) and the P-O-C stretching vibration (1094 , and 1063 cm^{-1}) attributing to the presence of CP became weak and shifted to a broad peak at around 1125 cm^{-1} (PO_2 asymmetric stretching vibration) at $300\text{ }^\circ\text{C}$. In addition, a P=O stretching

vibration peak was observed at around 1230 cm^{-1} , indicating the formation of phosphoric acid, which led to the carbonization and char formation of PVC [39]. Meanwhile, in PVC-10, the vibrations of CH_2 and C-Cl could be observed even at $350\text{ }^\circ\text{C}$. This indicates that the dehydrochlorination of PVC-10 did not occur completely. Thus, the addition of CP delayed the thermal decomposition process along by the dehydrochlorination of PVC. Consequently, the phosphonate moiety of CP induced the formation of both the phosphorus-containing complexes on PVC and the stable char layer at high temperatures, resulting in an improvement in the thermal stability of PVC.

However, considering that the decomposition of CP begins at around $300\text{ }^\circ\text{C}$, as shown in Figure 3.10, we were doubtful about the increase in $T_{5\%}$ of the PVC films with the addition of CP. The phosphonate group of CP induced flame retardancy in the PVC films after the decomposition at temperatures higher than $300\text{ }^\circ\text{C}$. Therefore, there should be another factor that played a key role in increasing the thermal stability of the PVC films below $300\text{ }^\circ\text{C}$. As unsaturated alkyl chains can trap various oxygen and alkyl radicals [40-42], herein, we focused on the anti-oxidant abilities of the unsaturated alkyl chains in CP, which suppressed the chain reaction of dehydrochlorination for PVC by a radical mechanism [34]. The various

radicals formed during the decomposition might be trapped by the unsaturated alkyl chain of CP and then induced inter and/or intra-polymerization between the unsaturated alkyl chains of CP [40]. This suggests that the cross-linked network structure formed by the inter and/or intra-polymerization of CP in PVC leads to an improvement in the thermal stability of PVC films at temperatures below 300 °C. Accordingly, we carried out DSC analyses to evaluate the polymerization ability between the unsaturated alkyl chain for cardanol and CP by heat treatment. As illustrated in Figure 3.11, an exothermic peak was observed at 143–195 °C during the first heating process, while no peak was observed in the second heating process in the DSC curves of cardanol. Similarly, the DSC curves of CP also exhibited an exothermic peak over a wide temperature range of 143–211 °C in only the first heating process, indicating that both the cardanol and CP exhibited inter- and/or intra-self-polymerization properties after the heat-treatment [43]. Therefore, we have focused on the effect of the cross-linked network structure of CP for PVC systems in the later part of this article.

First, we intentionally fabricated cross-linked PVC films from the PVC films by heat treatment. The PVC films cross-linked by the heat treatment were labeled as X-PVC-#, where # indicates the weight percentage of CP. Considering that the dehydrochlorination of PVC begins above

approximately 150 °C [44], the temperature for the heat treatment was set to 120 °C in air. To demonstrate that the heat treatment at 120 °C in air is an appropriate condition, the effect of temperature on the chemical structure of the PVC film was evaluated. The C-Cl bond at around 692 cm⁻¹ was observed even when the PVC films were heated at 140 °C for 1 h. However, the broad peak assigned to conjugated C=C stretching appeared at around 1600 cm⁻¹ for all the PVC films (Figure 3.12a) [45]. In addition, the color of the heated PVC films darkened because of PVC degradation [46]. Therefore, it was considered that the conjugated structures along the PVC chains were formed by the elimination of chlorine after the heat treatment at 140 °C. In contrast, after heating at 120 °C, the peak attributed to the conjugated C=C bonds and discoloration of PVC films were not observed, as shown in Figure 3.12b, indicating that the dehydrochlorination of PVC rarely occurs at 120 °C. DSC experiments were carried out to confirm the self-polymerization of CP in the PVC films, as shown in Figure 3.13a. It can be observed that the PVC films containing CP exhibited a broad exothermic peak over a wide temperature range of 160–200 °C owing to the self-polymerization of CP. This is consistent with the DSC results of CP. Meanwhile, after the heat treatment at 120 °C, the exothermic peak of the X-PVC films weakened or disappeared, confirming the occurrence of the

self-polymerization of CP in the PVC films (Figure 3.13b). Also, from the GPC analyses, the occurrence of self-polymerization of CP at 120 °C could be confirmed. The GPC trace of the heat-treated CP at 120 °C is shifted to a lower elution volume and broadened as compared to that of CP (Figure 3.14). It was thought that the cross-linked structure formed by self-polymerization of CP should increase the radius of gyration of the molecule compared to the uncross-linked structure, leading to a shift to lower elution volumes [47]. These results indicate that the heat treatment temperature of 120 °C was optimum for investigating the effect of the cross-linked network induced by the self-polymerization of CP on flame retardancy and physical properties of PVC.

To compare the flame retardancy of the PVC and X-PVC films, LOI and UL-94 V tests, which are usually used to confirm the flame retardancy of polymers [48], were conducted. The LOI and UL-94 ratings of the films are shown in Figure 3.15a and listed in Table 3.5. In general, when the LOI value of a polymer is more than 26.0%, it is considered to be flame-retardant [49]. From the LOI test results, it was found that the incorporation of CP increased the LOI value of PVC. The LOI value of PVC-0 was only 24.0%, which is comparable to the LOI value of conventional PVC reported previously [50], while the LOI values for the PVC-5, PVC-7, and PVC-10

films were 24.9%, 26.1%, and 26.2%, respectively. These results could be explained by the TG-FTIR results (Figure 3.9) that the phosphonate group in CP generated phosphoric acid during the combustion and forms stable char on PVC. This is regarded as a typical condensed-phase flame-retardant mechanism [39, 51]. It is noteworthy that the cross-linked network of CP in PVC considerably increases the LOI value, as shown in Figure 3.15a. The X-PVC-5, X-PVC-7, and X-PVC-10 films exhibited increased LOI values compared to the PVC-5, PVC-7, and PVC-10 films, respectively. For example, even 5 wt % of CP in PVC increased the LOI value from 24.9% to 28.6 % after the heat treatment. The UL-94 V test results also showed that the flame retardancy of PVC films containing CP increased after the heat treatment. The PVC films with relatively low amounts of CP burned continuously with no extinguishing and ignited the cotton with heavy melt-dripping, which resulted in the failure to pass the UL-94 V test. However, when more CP was added (PVC-7 and PVC-10), the films showed self-extinguishing properties within 10 s and had no melt-dripping throughout the test, and hence achieved the V-0 rating. The burning processes of the PVC-0 and PVC-10 films are shown in Figure 3.16. Meanwhile, the heat-treated PVC film with only 5 wt% of CP, X-PVC-5, showed evidently improved flame-retardant performance compared to PVC-5. As mentioned

earlier, PVC-5 was not classified in the UL-94 V test because of its flammability, while X-PVC-5 showed self-extinguishing properties with igniter removal and exhibited anti-dripping properties by forming char on PVC (Figure 3.16c). Therefore, all the X-PVC films in this study achieved the V-0 rating in the UL-94 V test, which suggests that the cross-linked network of CP significantly enhanced the flame retardancy of PVC by inducing anti-dripping performance and the formation of intumescent char on the bottom of the PVC film (Figure 3.15a).

To corroborate the flame-retardant effect of the cross-linked CP, PVC-10 and X-PVC-10 (20 mm × 20 mm × 1 mm) were heated in a muffle furnace at 350 °C in air. As shown in Figure 3.15b, although there was intumescent char in both the films, X-PVC-10 shows more expanded char than PVC-10, indicating that the cross-linked CP induced the formation of a large and thick char layer on PVC after the heat treatment by increasing the char forming efficiency. To further investigate the chemical structure of the char layer, Raman spectroscopy, which is a powerful tool to characterize carbonaceous materials [12] was performed for the PVC and X-PVC films after combustion (Figure 3.15c and Figure 3.17). As shown in Figure 3.15c, the Raman spectra for PVC-10 and X-PVC-10 showed two peaks with the maximum intensity at 1584 (G band) and 1380 cm⁻¹ (D band), which

represents polyaromatic species. The G band corresponds to the vibration mode in the sp^2 carbon atoms in the organized graphitic structure, and the D band is associated with a disordered carbon structure [52]. Herein, the integrated intensity ratio of the D and G bands (I_D/I_G) was used to characterize the graphitization degree of the char layer [53]. Figure 3.15d shows the decrease in the I_D/I_G value of the residual char on the PVC films with an increase in the CP content: PVC-5 (2.36) > PVC-7 (2.28) > PVC-10 (1.74), suggesting that the incorporation of CP into PVC formed a more graphitized carbon structure. In addition, all the X-PVC films showed lower I_D/I_G values than the PVC films, which indicates that the cross-linked network of CP facilitated the formation of graphitized char. These results are consistent with the LOI and UL-94 V test results. Considering that the graphitized structure is more stable than a disordered carbon structure, it was thought that the cross-linked CP could effectively protect PVC by forming of a graphitic structured char layer on the surface, which in turn enhanced the flame retardancy of the X-PVC films [54, 55].

In addition to the flame retardancy, the physical properties of the PVC and X-PVC films were investigated using tensile tests to evaluate the potential of CP as a plasticizer for PVC (Figure 3.18). With the incorporation of CP, the elongation at break of the PVC films increased, while the tensile

strength decreased, indicating that CP had a significant plasticizing effect on the PVC films. For example, the elongation at break of PVC-10 increased by about 148% (137.4% (± 8.5)) as compared to that of PVC-0 (55.4% (± 1.9)). This can be explained by the fact that the long alkyl chain of CP improves the flexibility of PVC films by decreasing the cohesion force between the PVC chains. A similar trend was observed for the elongation at break in the X-PVC films, while the absolute values were smaller than those of each PVC film having the same amount of CP. However, in the case of the tensile strength, the X-PVC films showed higher values than the corresponding PVC film. This can be attributed to the relatively restricted mobility of the PVC chains due to the formation of an interpenetrating network from the inter/intra-polymerization of CP in the PVC film. To clearly investigate the effect of CP on the flexibility of PVC during the heat treatment, DSC measurements were carried out (Figure 3.19). As shown in Figure 3.19a, the glass transition temperature (T_g) of the PVC films decreased with an increase in the CP content: T_g of PVC-0 (79.4 °C) and T_g of PVC-10 (24.1 °C). Also, DSC results showed that CP does not affect the crystallinity of PVC, and these results are supported by XRD analysis (Figure 3.20). XRD pattern of PVC-0 showed a broad peak at $2\theta = 24.5^\circ$, which demonstrates its amorphous nature [56]. All the PVC films containing

CP were similar to that of PVC-0, indicating that the amorphous nature of PVC was maintained even if CP is added. Also, even with the incorporation of CP, no difference in the d-spacing of PVC was observed. As can be seen from the DSC and XRD results, it is shown that CP occupies the space between the PVC chains without d-spacing change, leading to an improvement in the flexibility of the PVC films. Meanwhile, from Figure 3.19b, it can be observed that the T_g of all the X-PVC films increased because the mobility of the PVC chains was restricted by the self-polymerization of CP, while it was still lower than that of PVC-0, implying that the cross-linked network of CP induced a plasticizing effect in PVC. Furthermore, we directly examined the flexibility of X-PVC-10, as illustrated in Figure 3.21. X-PVC-10 could accommodate various deformations such as twisting and bending, indicating that the film maintained its flexibility even after the heat-treatment. Consequently, in the X-PVC films, the cross-linked network of CP led to an increase in T_g and a decrease in the elongation at break of the films. However, the flexibility of the X-PVC films was still higher than that of PVC-0, and the tensile strength of the X-PVC films improved after the heat treatment as compared to that of PVC-0. Therefore, in this study, PVC films with high flexibility and improved mechanical strength were fabricated via a simple heat-

treatment process.

The results discussed thus far indicate that CP as a plasticizer increases the flexibility of PVC. However, because these small molecules often cause migration problems, which might be harmful to human health [57, 58], it is important to investigate the migration behavior of plasticizers from PVC. In this study, the migration behaviors of CP from the PVC and X-PVC films in polar distilled water and nonpolar n-hexane were monitored using UV absorbance at 265 nm. The cumulative amount of migration with time was calculated using calibration curves (Figure 3.22). As illustrated in Figure 3.23a, for all the PVC films, migration was almost not observed in n-hexane for 24 h. In comparison with the migration behavior of di-(2-ethylhexyl) phthalate (DEHP), which is widely used as a plasticizer for PVC [59], CP exhibited much lower migration. When immersed in n-hexane, DEHP shows a migration of approximately 20% after 2 h [59], whereas CP did not show migration even after 12 h. The rate of migration decreased with an increase in the number of carbon atoms due to the increase in the hydrophobicity of the long alkyl chain [60]. As shown in Figure 3.23c, no migration was observed in n-hexane for all the X-PVC films, indicating that the migration was much more restricted by the cross-linked network of CP. In particular, Figure 3.23b and Figure 3.23d show that migration was not observed in

distilled water for both the PVC and X-PVC films because CP is insoluble in distilled water. Therefore, considering the actual application and its environment, we believe that CP is suitable as an additive for PVC. In addition, X-PVC films manifest superior transparency, as shown in Figure 3.24. The text under all the X-PVC films is clearly shown, which means that the transparency of the films did not deteriorate even after the heat treatment. Consequently, considering the advantages of the PVC-CP system, CP, which shows considerably improved flame retardancy by self-polymerization, is a potential candidate for plasticized PVC.

3.4. Conclusion

In summary, a renewable cardanol-based additive for PVC, CP, was successfully synthesized with the expectation that the phosphonate group and long alkyl chain of CP can enhance the flame retardancy and flexibility of PVC, respectively. Then, transparent PVC films with different CP contents were prepared via simple solution casting. The incorporation of CP into PVC facilitated the formation of compact and dense char, which is beneficial for improving the thermal stability and flame retardancy of PVC films. When incorporating more than 7 wt% CP into PVC, the PVC films showed an increase in LOI value and an achievement on V-0 rating in UL-94 V test in comparison with PVC-0. Moreover, an enhancement in the flexibility of PVC with an increase in the CP content was demonstrated by the increased elongation and reduced T_g . Meanwhile, it was demonstrated that CP can self-polymerize by heat treatment. We systematically investigated whether the cross-linked network of CP affects the flame retardancy and physical properties of PVC. While the LOI value of PVC-5 was 24.9% with no rating in the UL-94 V test, the LOI value of 28.6% and the UL-94 rating of V-0 were achieved for the X-PVC-5 film. It was

demonstrated that the cross-linked network of CP improved the flame retardancy of PVC more effectively, which might have contributed to the anti-dripping property by the formation of more expandable graphitized char. Although the elongation at break of the PVC films decreased after the heat treatment, the films showed enhanced mechanical strength and flexibility after the heat treatment. Furthermore, because the X-PVC films exhibited high transparency and migration stabilities, it was anticipated that CP with the self-polymerization property is a potential green, flexible, and flame-retarding additive for PVC.

3.5. References

1. Bocqué, M., et al., *Phosphonated lipids as primary plasticizers for PVC with improved flame retardancy*. European Journal of Lipid Science and Technology, 2018. **120**(8): p. 1800062.
2. Wu, W.H., et al., *Two series of inorganic melamine salts as flame retardants and smoke suppressants for flexible PVC*. Polymer Composites, 2018. **39**(2): p. 529-536.
3. Li, M., et al., *Tung oil based plasticizer and auxiliary stabilizer for poly (vinyl chloride)*. Materials & Design, 2017. **122**: p. 366-375.
4. Jia, P., et al., *Green plasticizers derived from soybean oil for poly (vinyl chloride) as a renewable resource material*. Korean Journal of Chemical Engineering, 2016. **33**(3): p. 1080-1087.
5. Yoon, S.K. and D.J. Chung, *Development of blood compatible composite using MPC copolymer and polyolefin for non-PVC blood bag application*. Macromolecular Research, 2020. **28**(4): p. 319-326.
6. Chen, J., et al., *Synthesis and properties of a novel environmental epoxidized glycidyl ester of ricinoleic acetic ester plasticizer for poly (vinyl chloride)*. Polymers, 2017. **9**(12): p. 640.
7. Kumar, S., *Recent developments of biobased plasticizers and their effect on mechanical and thermal properties of poly (vinyl chloride): a review*. Industrial & Engineering Chemistry Research, 2019. **58**(27): p. 11659-11672.
8. Perez, A.L., et al., *Health risk assessment of exposures to a high molecular weight plasticizer present in automobile interiors*.

- Chemosphere, 2017. **167**: p. 541-550.
9. Chen, J., et al., *Synthesis and application of a novel environmental plasticizer based on cardanol for poly (vinyl chloride)*. Journal of the Taiwan Institute of Chemical Engineers, 2016. **65**: p. 488-497.
 10. Chen, J., et al., *Epoxidized castor oil-based diglycidyl-phthalate plasticizer: Synthesis and thermal stabilizing effects on poly (vinyl chloride)*. Journal of Applied Polymer Science, 2019. **136**(9): p. 47142.
 11. Jia, P., et al., *Design and synthesis of a castor oil based plasticizer containing THEIC and diethyl phosphate groups for the preparation of flame-retardant PVC materials*. RSC Advances, 2017. **7**(2): p. 897-903.
 12. Zhao, H.-B., et al., *A flame-retardant-free and thermo-cross-linkable copolyester: Flame-retardant and anti-dripping mode of action*. Polymer, 2014. **55**(10): p. 2394-2403.
 13. Kim, D.K., et al., *PPE/nylon 66 blends with high mechanical toughness and flame Retardancy*. Macromolecular Research, 2020. **28**(2): p. 103-109.
 14. Gholamian, F., et al., *The effect of flower-like magnesium hydroxide nanostructure on the thermal stability of cellulose acetate and acrylonitrile–butadiene–styrene*. Journal of Cluster Science, 2013. **24**(1): p. 73-84.
 15. Joulaei, M., K. Hedayati, and D. Ghanbari, *Investigation of magnetic, mechanical and flame retardant properties of polymeric nanocomposites: Green synthesis of MgFe₂O₄ by lime and orange extracts*. Composites Part B: Engineering, 2019. **176**: p. 107345.

16. Yu, G., et al., *Brominated flame retardants (BFRs): A review on environmental contamination in China*. Chemosphere, 2016. **150**: p. 479-490.
17. Pittinger, C.A. and A.M. Pecquet, *Review of historical aquatic toxicity and bioconcentration data for the brominated flame retardant tetrabromobisphenol A (TBBPA): effects to fish, invertebrates, algae, and microbial communities*. Environmental Science and Pollution Research, 2018. **25**(15): p. 14361-14372.
18. Dingemans, M.M., M. van den Berg, and R.H. Westerink, *Neurotoxicity of brominated flame retardants:(in) direct effects of parent and hydroxylated polybrominated diphenyl ethers on the (developing) nervous system*. Environmental Health Perspectives, 2011. **119**(7): p. 900-907.
19. Ghanbari, D., M. Salavati-Niasari, and M. Ghasemi-Kooch, *In situ and ex situ synthesis of poly (vinyl alcohol)-Fe₃O₄ nanocomposite flame retardants*. Particuology, 2016. **26**: p. 87-94.
20. Pham, L.H., et al., *Effective phosphorus/phosphorus-nitrogen fire retardants applied to biocomposites based on polypropylene-wood flour: flammability, thermal behavior, and mechanical properties*. Macromolecular Research, 2019. **27**(12): p. 1185-1192.
21. Faye, I., et al., *Eugenol bio-based epoxy thermosets: from cloves to applied materials*. Green Chemistry, 2017. **19**(21): p. 5236-5242.
22. Zhang, X., et al., *Hexa (eugenol) cyclotriphosphazene modified bismaleimide resins with unique thermal stability and flame retardancy*. Reactive and Functional Polymers, 2017. **113**: p. 77-84.
23. Wang, S., et al., *Vanillin-derived high-performance flame retardant*

- epoxy resins: facile synthesis and properties*. *Macromolecules*, 2017. **50**(5): p. 1892-1901.
24. Phalak, G., et al., *Synthesis of acrylated cardanol diphenyl phosphate for UV curable flame-retardant coating application*. *European Polymer Journal*, 2019. **121**: p. 109320.
 25. Ecochard, Y., et al., *Cardanol and eugenol based flame retardant epoxy monomers for thermostable networks*. *Molecules*, 2019. **24**(9): p. 1818.
 26. Ravichandran, S., et al., *A renewable waste material for the synthesis of a novel non-halogenated flame retardant polymer*. *Journal of Cleaner Production*, 2011. **19**(5): p. 454-458.
 27. Isitman, N.A. and C. Kaynak, *Tailored flame retardancy via nanofiller dispersion state: Synergistic action between a conventional flame-retardant and nanoclay in high-impact polystyrene*. *Polymer Degradation and Stability*, 2010. **95**(9): p. 1759-1768.
 28. Kashiwagi, T., et al., *Flammability properties of polymer nanocomposites with single-walled carbon nanotubes: effects of nanotube dispersion and concentration*. *Polymer*, 2005. **46**(2): p. 471-481.
 29. Ghanbari, D., M. Salavati-Niasari, and M. Sabet, *Polymeric matrix nanocomposites: influence of cadmium sulfide nanostructure on the thermal degradation of poly (vinyl alcohol) and cellulose acetate*. *Journal of Cluster Science*, 2012. **23**(4): p. 1081-1095.
 30. Shams, H.R., et al., *Solvothermal synthesis of carbon nanostructure and its influence on thermal stability of poly styrene*. *Composites*

Part B: Engineering, 2013. **55**: p. 362-367.

31. Yuan, B., et al., *Poorly-/well-dispersed graphene: abnormal influence on flammability and fire behavior of intumescent flame retardant*. Composites Part A: Applied Science and Manufacturing, 2018. **109**: p. 345-354.
32. Pagacz, J. and K. Pielichowski, *Preparation and characterization of PVC/montmorillonite nanocomposites—a review*. Journal of Vinyl and Additive Technology, 2009. **15**(2): p. 61-76.
33. Jia, P., et al., *PVC materials without migration obtained by chemical modification of azide-functionalized PVC and triethyl citrate plasticizer*. Materials Chemistry and Physics, 2017. **190**: p. 25-30.
34. Yu, J., et al., *Thermal degradation of PVC: A review*. Waste Management, 2016. **48**: p. 300-314.
35. Hasan, M., et al., *Synthesis of PVC/CNT nanocomposite fibers using a simple deposition technique for the application of Alizarin Red S (ARS) removal*. RSC Advances, 2015. **5**(19): p. 14393-14399.
36. Zhu, H., et al., *TG-FTIR analysis of PVC thermal degradation and HCl removal*. Journal of Analytical and Applied Pyrolysis, 2008. **82**(1): p. 1-9.
37. Alghunaim, N., *Spectroscopic analysis of PMMA/PVC blends containing CoCl₂*. Results in Physics, 2015. **5**: p. 331-336.
38. Truc, N.T.T., et al., *Development of hydrophobicity and selective separation of hazardous chlorinated plastics by mild heat treatment after PAC coating and froth flotation*. Journal of Hazardous Materials, 2017. **321**: p. 193-202.
39. Green, J., *A review of phosphorus-containing flame retardants*.

- Journal of Fire Sciences, 1992. **10**(6): p. 470-487.
40. John, G. and C. Pillai, *Synthesis and characterization of a self-crosslinkable polymer from cardanol: Autooxidation of poly (cardanyl acrylate) to crosslinked film*. Journal of Polymer Science Part A: Polymer Chemistry, 1993. **31**(4): p. 1069-1073.
 41. Ohkatsu, Y., T. Matsuura, and M. Yamato, *A phenolic antioxidant trapping both alkyl and peroxy radicals*. Polymer Degradation and Stability, 2003. **81**(1): p. 151-156.
 42. Rodrigues, F.H.A., et al., *Antioxidant activity of cashew nut shell liquid (CNSL) derivatives on the thermal oxidation of synthetic cis-1, 4-polyisoprene*. Journal of the Brazilian Chemical Society, 2006. **17**(2): p. 265-271.
 43. Sakulsaknimitr, W., et al., *Structure and thermal properties of polyurethanes synthesized from cardanol diol*. Journal of Polymers and the Environment, 2015. **23**(2): p. 216-226.
 44. Zheng, X.-G., et al., *Dehydrochlorination of PVC materials at high temperature*. Energy & Fuels, 2003. **17**(4): p. 896-900.
 45. Rahmah, M. and N.N. Mohd, *FTIR characterization and conductivity studies of undoped and doped synthesized polyene from polyvinylchloride with sustainable epoxidised oil coating resin*. Australian Journal of Basic and Applied Sciences, 2014. **8**(5): p. 313-318.
 46. Tian, W., et al., *Facile synthesis of exfoliated vermiculite nanosheets as a thermal stabilizer in polyvinyl chloride resin*. RSC Advances, 2019. **9**(34): p. 19675-19679.
 47. Smaldone, R.A., E.c. Lin, and J.S. Moore, *Intrastrand foldamer*

- crosslinking by reductive amination*. Journal of Polymer Science Part A: Polymer Chemistry, 2010. **48**(4): p. 927-935.
48. Tao, K., et al., *A novel phosphazene cyclomatrix network polymer: Design, synthesis and application in flame retardant polylactide*. Polymer Degradation and Stability, 2011. **96**(7): p. 1248-1254.
 49. Cullis, C. and M. Hirschler, *Char formation from polyolefins. Correlations with low-temperature oxygen uptake and with flammability in the presence of metal halogen systems*. European Polymer Journal, 1984. **20**(1): p. 53-60.
 50. Wang, H., et al., *Flame retardant property of Sb₂O₃/SnO₂ and their synergism in flexible PVC*. Journal of Fire Sciences, 2006. **24**(3): p. 195-210.
 51. Green, J., *Mechanisms for flame retardancy and smoke suppression-a review*. Journal of Fire Sciences, 1996. **14**(6): p. 426-442.
 52. Sun, Z., et al., *Effect of additive phosphorus-nitrogen containing flame retardant on char formation and flame retardancy of epoxy resin*. Materials Chemistry and Physics, 2018. **214**: p. 154-164.
 53. Pimenta, M., et al., *Studying disorder in graphite-based systems by Raman spectroscopy*. Physical Chemistry Chemical Physics, 2007. **9**(11): p. 1276-1290.
 54. Duan, L., et al., *Hyperbranched phosphorus/nitrogen-containing polymer in combination with ammonium polyphosphate as a novel flame retardant system for polypropylene*. Polymer Degradation and Stability, 2016. **134**: p. 179-185.
 55. Cai, W., et al., *A novel strategy to simultaneously electrochemically prepare and functionalize graphene with a multifunctional flame*

- retardant*. Chemical Engineering Journal, 2017. **316**: p. 514-524.
56. Hasan, M. and M. Lee, *Enhancement of the thermo-mechanical properties and efficacy of mixing technique in the preparation of graphene/PVC nanocomposites compared to carbon nanotubes/PVC*. Progress in Natural Science: Materials International, 2014. **24**(6): p. 579-587.
57. Tickner, J.A., et al., *Health risks posed by use of Di-2-ethylhexyl phthalate (DEHP) in PVC medical devices: A critical review*. American Journal of Industrial Medicine, 2001. **39**(1): p. 100-111.
58. Al Salloum, H., et al., *Studying DEHP migration in plasticized PVC used for blood bags by coupling Raman confocal microscopy to UV spectroscopy*. Materials Science and Engineering: C, 2016. **61**: p. 56-62.
59. Pan, S., et al., *A potentially general approach to aliphatic ester-derived PVC plasticizers with suppressed migration as sustainable alternatives to DEHP*. Green Chemistry, 2019. **21**(23): p. 6430-6440.
60. Kastner, J., et al., *Aqueous leaching of di-2-ethylhexyl phthalate and "green" plasticizers from poly (vinyl chloride)*. Science of the Total Environment, 2012. **432**: p. 357-364.

Table 3.1. Formulations of the PVC films with different CP contents

Sample	PVC (wt%)	CP (wt%)
PVC-0	100	-
PVC-5	95	5
PVC-7	93	7
PVC-10	90	10

Table 3.2. FTIR assignments for cardanol and CP

Wavenumber (cm⁻¹)	Assignment
3350, 1348	O-H stretching
3010	=C-H stretching of unsaturated hydrocarbons
2923, 2854	C-H stretching of aliphatic chains
1590, 1456	C=C stretching of aromatic group
1132, 633	P=O stretching of aryl phosphonate
960	P-O-C stretching of aryl phosphonate

Table 3.3. TGA results and P content in residual char of the PVC films

Sample	T_{5%} (°C)	T_{50%} (°C)	Residual char (%)	P content (wt%) after combustion
PVC-0	224	318	10.1	0
PVC-5	267	330	10.0	1.04
PCV-7	264	336	10.1	2.07
PVC-10	273	345	14.3	2.75

Table 3.4. FTIR assignments for thermal degradation behavior of PVC-0 and PVC-10

Wavenumber (cm⁻¹)	Assignment
2978	-CH stretching
2911, 2853	CH ₂ asymmetric stretching
1426, 1252	CH ₂ wagging
1230	P=O stretching of phosphoric acid
1131	P=O stretching of aryl phosphonate
1125	PO ₂ asymmetric stretching
1094, 1063	P-O-C stretching of aryl phosphonate
692	C-Cl stretching

Table 3.5. LOI and UL-94 test results of the PVC and X-PVC films

Sample	Time to self-extinguishing (s)	Drips	Ignition to cotton	UL 94 rating	LOI (%)
PVC-0	-	Y	Y	N.C.	24.0
PVC-5	-	Y	Y	N.C.	24.9
PVC-7	≤ 10	N	N	V-0	26.1
PVC-10	≤ 10	N	N	V-0	26.2
X-PVC-5	≤ 10	N	N	V-0	28.6
X-PVC-7	≤ 10	N	N	V-0	29.3
X-PVC-10	≤ 10	N	N	V-0	29.8

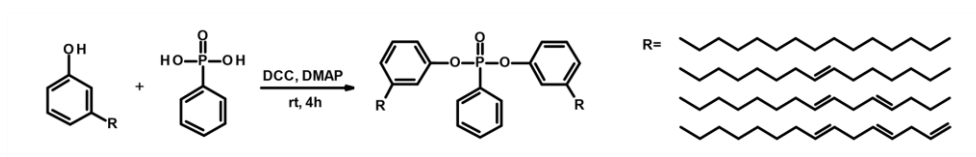


Figure 3.1. Schematic illustration of synthesis route of CP

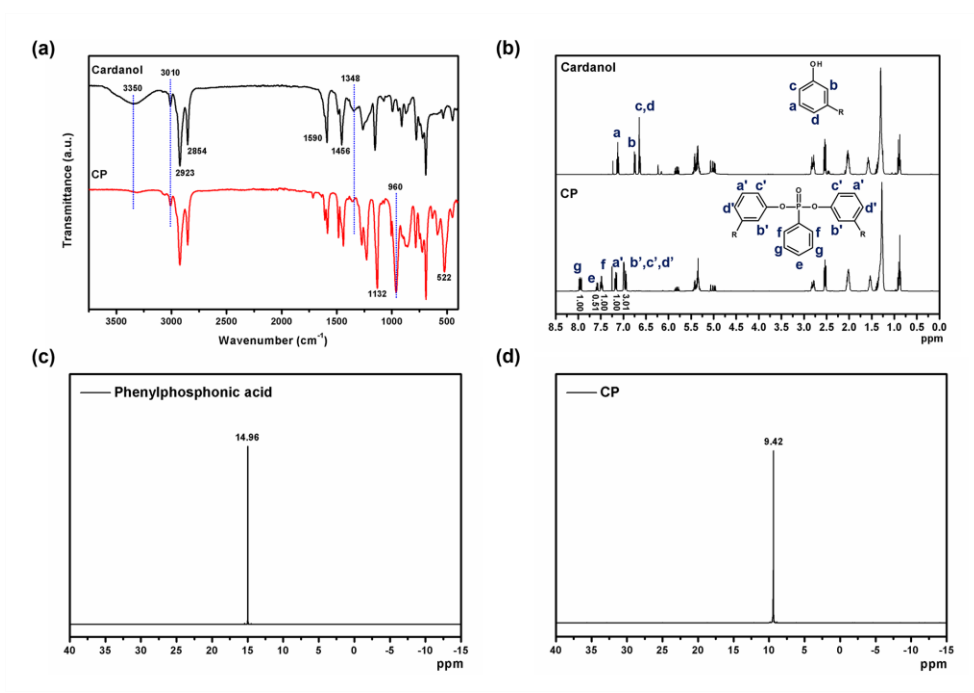


Figure 3.2. (a) FTIR spectra of cardanol and CP, (b) ¹H NMR spectra of cardanol and CP, and ³¹P NMR spectra of (c) phenylphosphonic acid and (d) CP

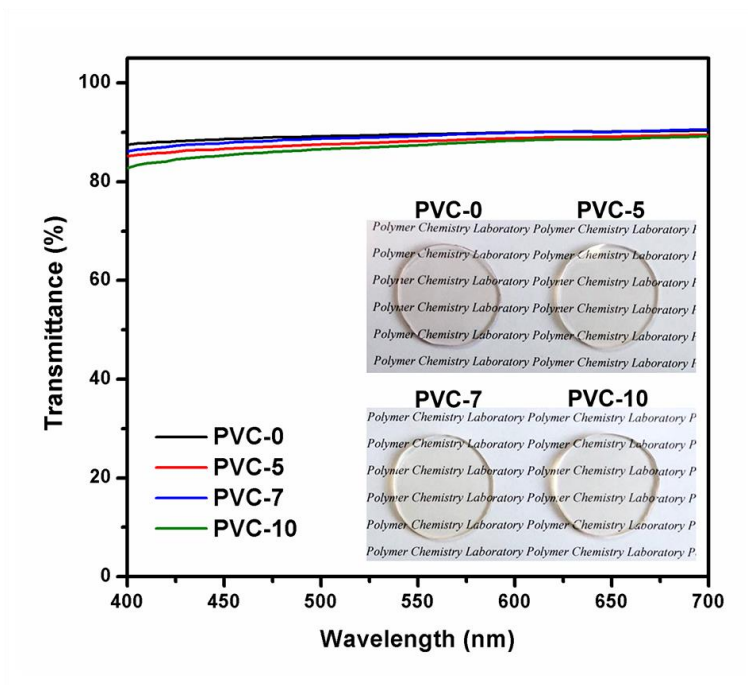


Figure 3.3. Transmittance spectra of PVC films over the wavelength range of 400-700 nm (inset pictures: digital photographs of the PVC films)

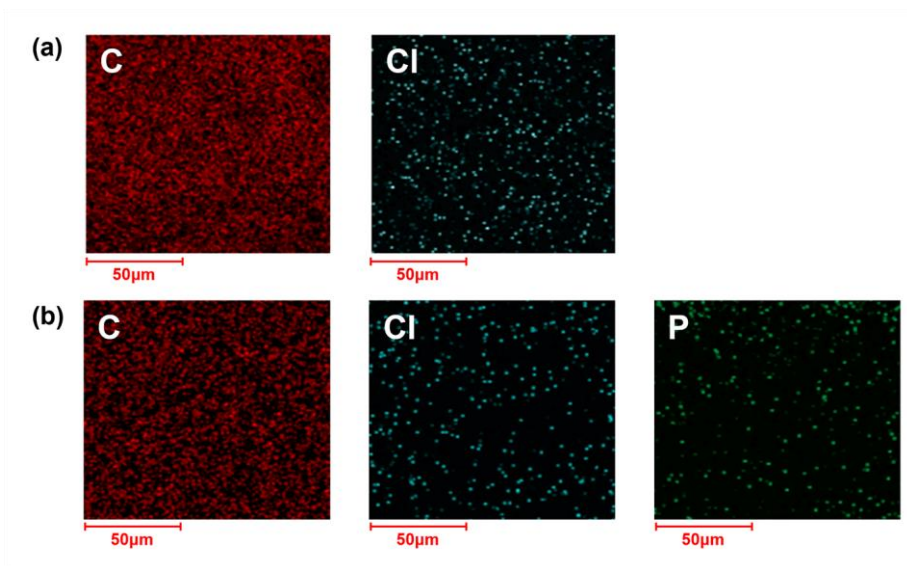


Figure 3.4. SEM-EDS of (a) PVC-0 and (b) PVC-10

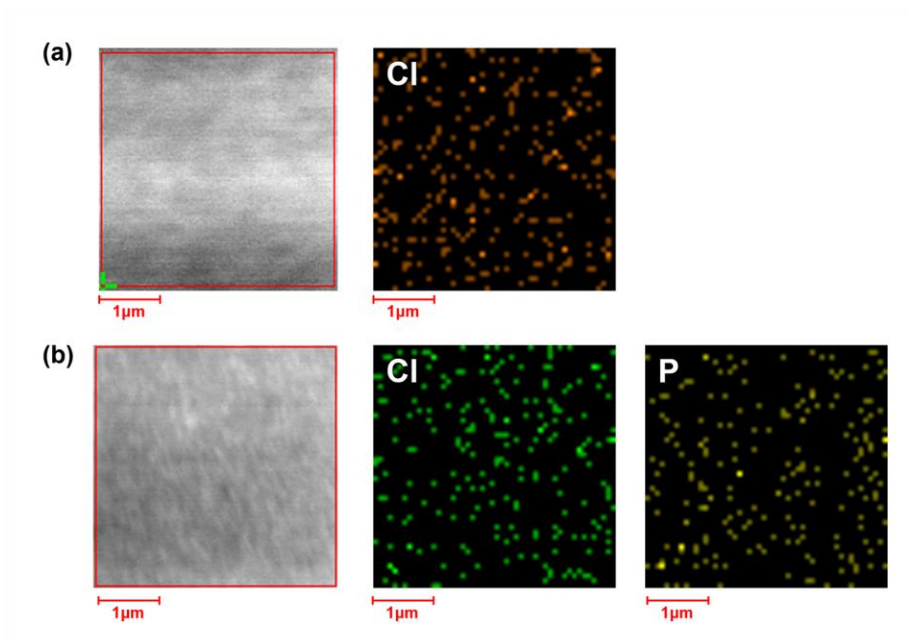


Figure 3.5. TEM-EDS of (a) PVC-0 and (b) PVC-10

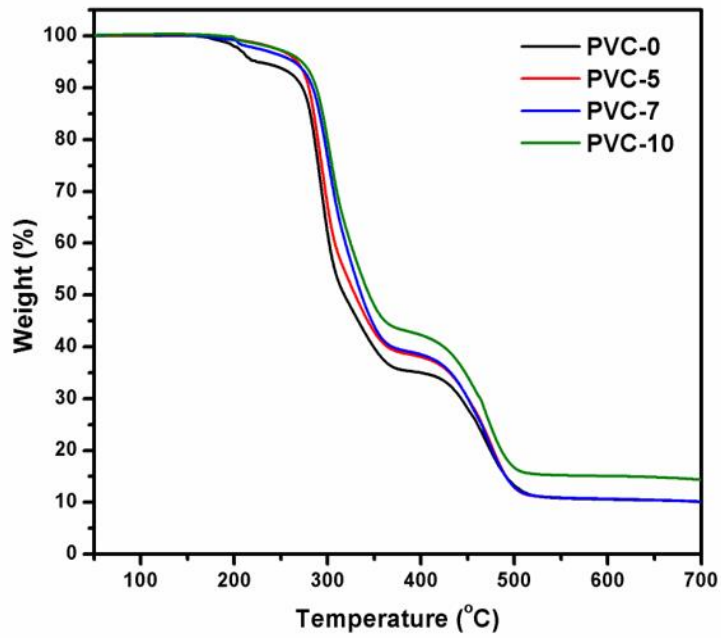


Figure 3.6. TGA curves of the PVC films in N₂

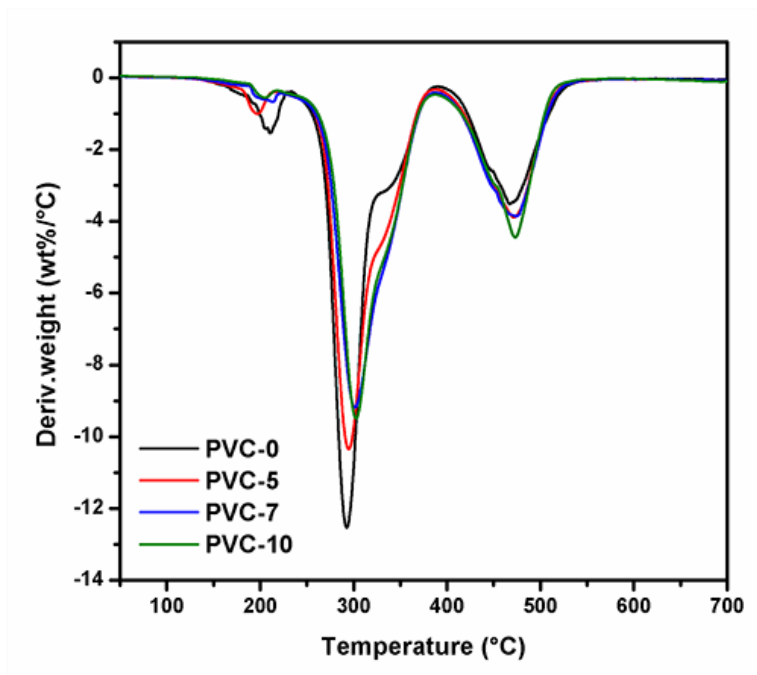


Figure 3.7. DTG curves of the PVC films

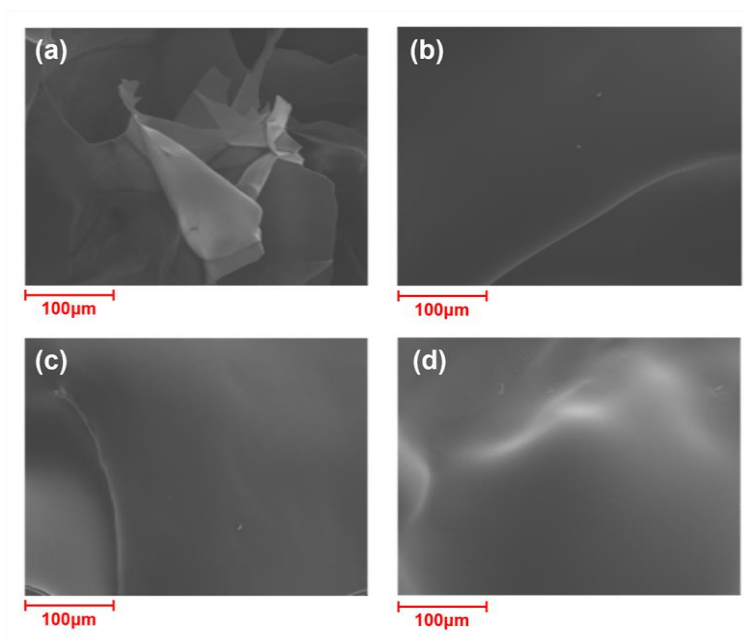


Figure 3.8. SEM images for the residual char of (a) PVC-0, (b) PVC-5, (c) PVC-7, and (d) PVC-10

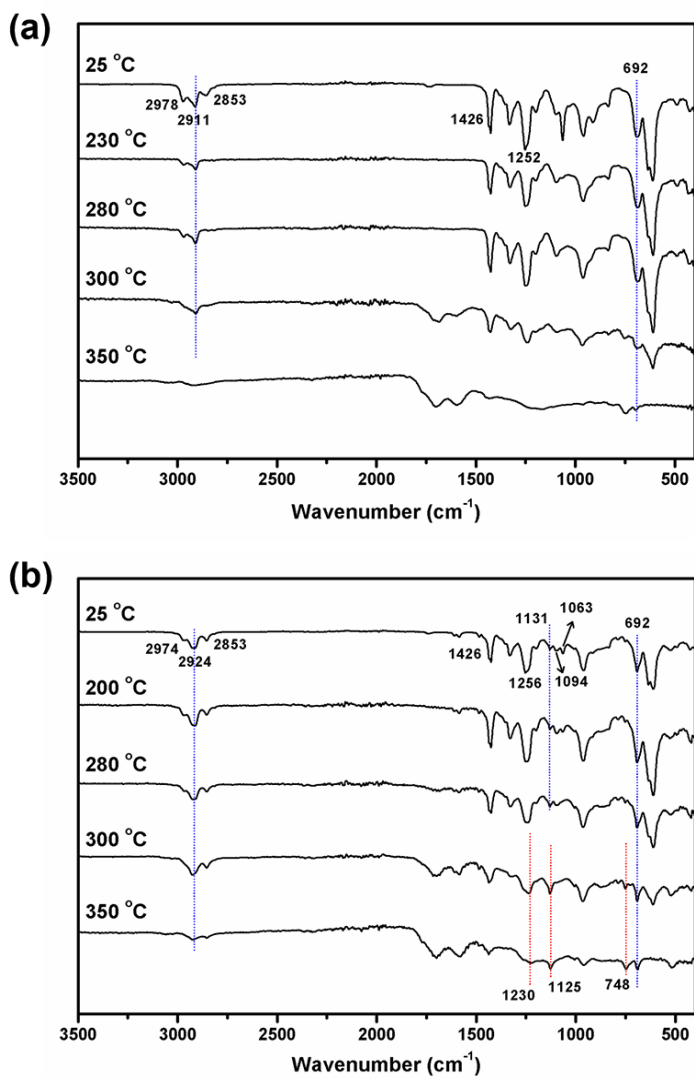


Figure 3.9. TG-FTIR spectra of (a) PVC-0 and (b) PVC-10

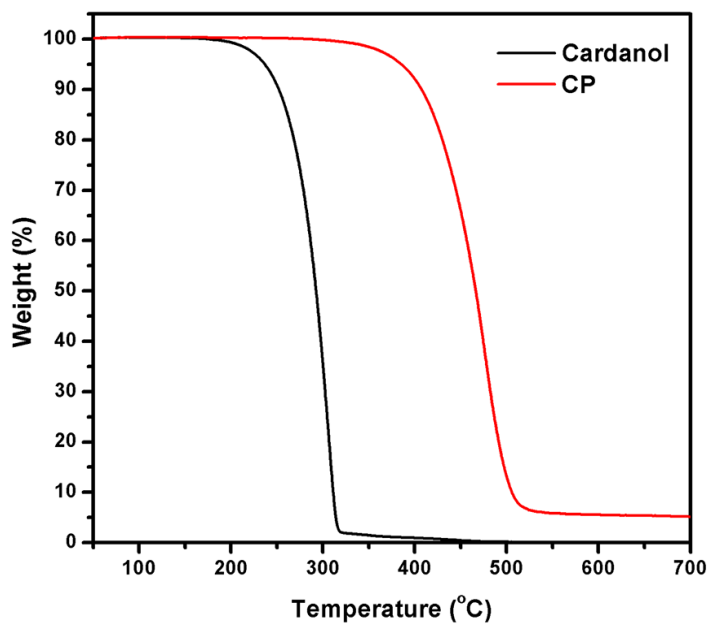


Figure 3.10. TGA curves of cardanol and CP

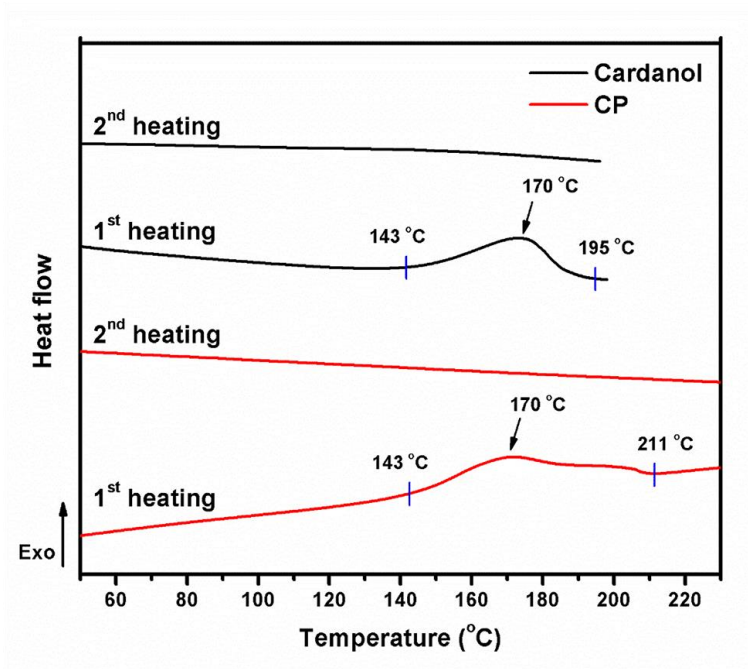


Figure 3.11. DSC curves of cardanol and CP

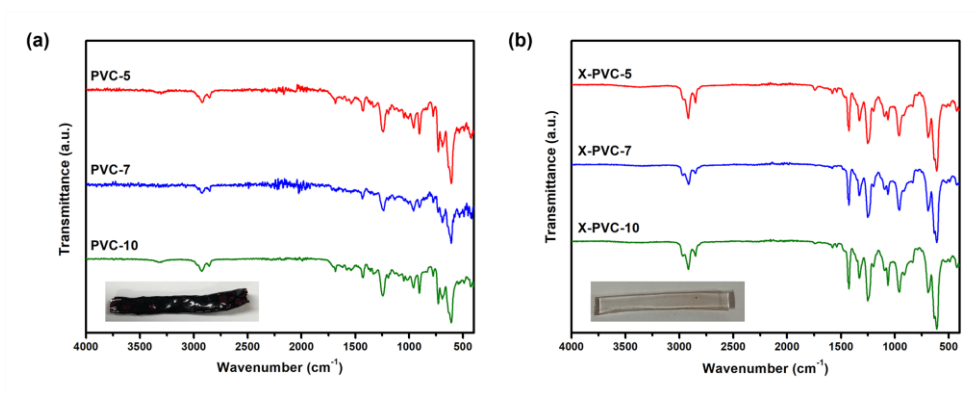


Figure 3.12. FTIR spectra of the PVC films after heat-treatment at (a) 140 °C for 1 h and (b) 120 °C for 1 h

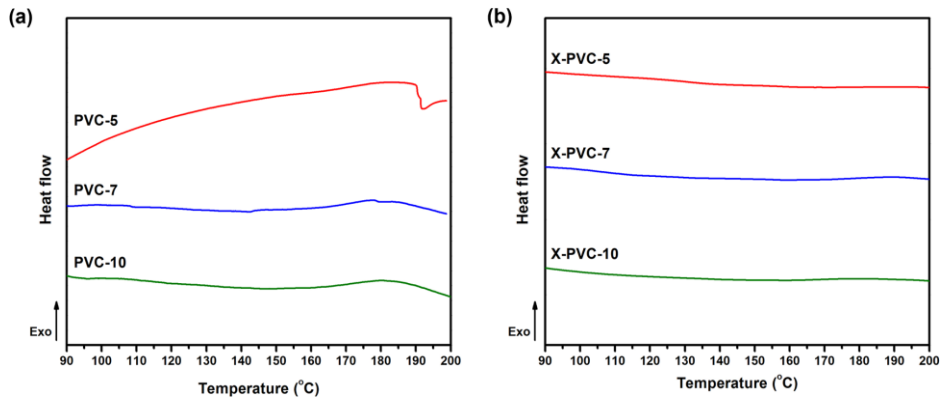


Figure 3.13. DSC curves of the (a) PVC films and (b) X-PVC films

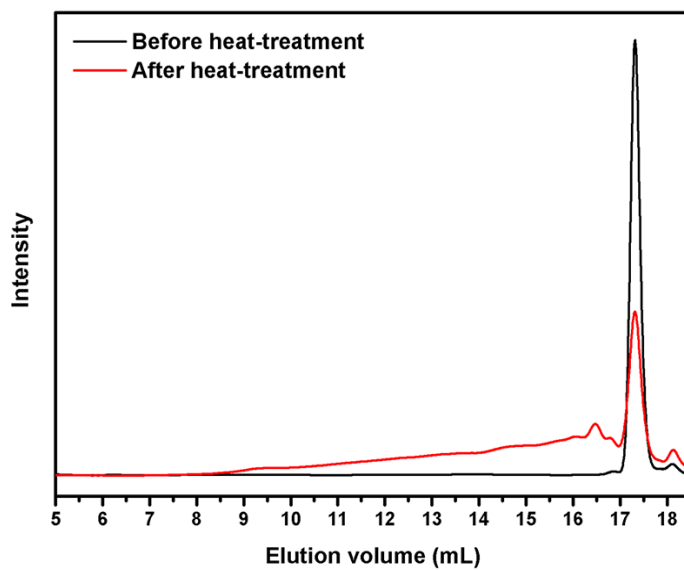


Figure 3.14. GPC results of CP of before and after the heat-treatment

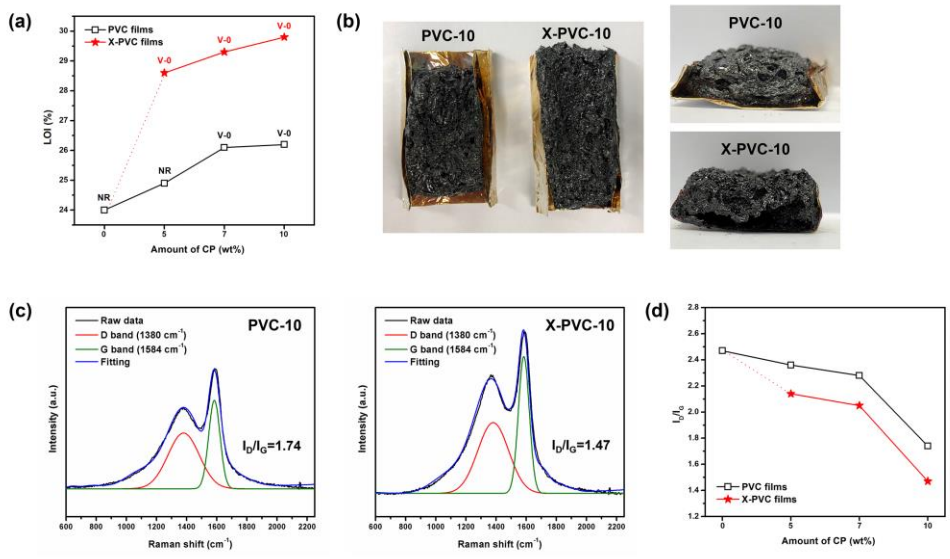


Figure 3.15. (a) LOI values and UL-94 ratings of the PVC and X-PVC films, (b) digital photographs for residual char of PVC-10 and X-PVC-10, (c) Raman spectra for residual char of PVC-10 and X-PVC-10, and (d) I_D/I_G values of the PVC and X-PVC films, as obtained from the Raman spectroscopy results

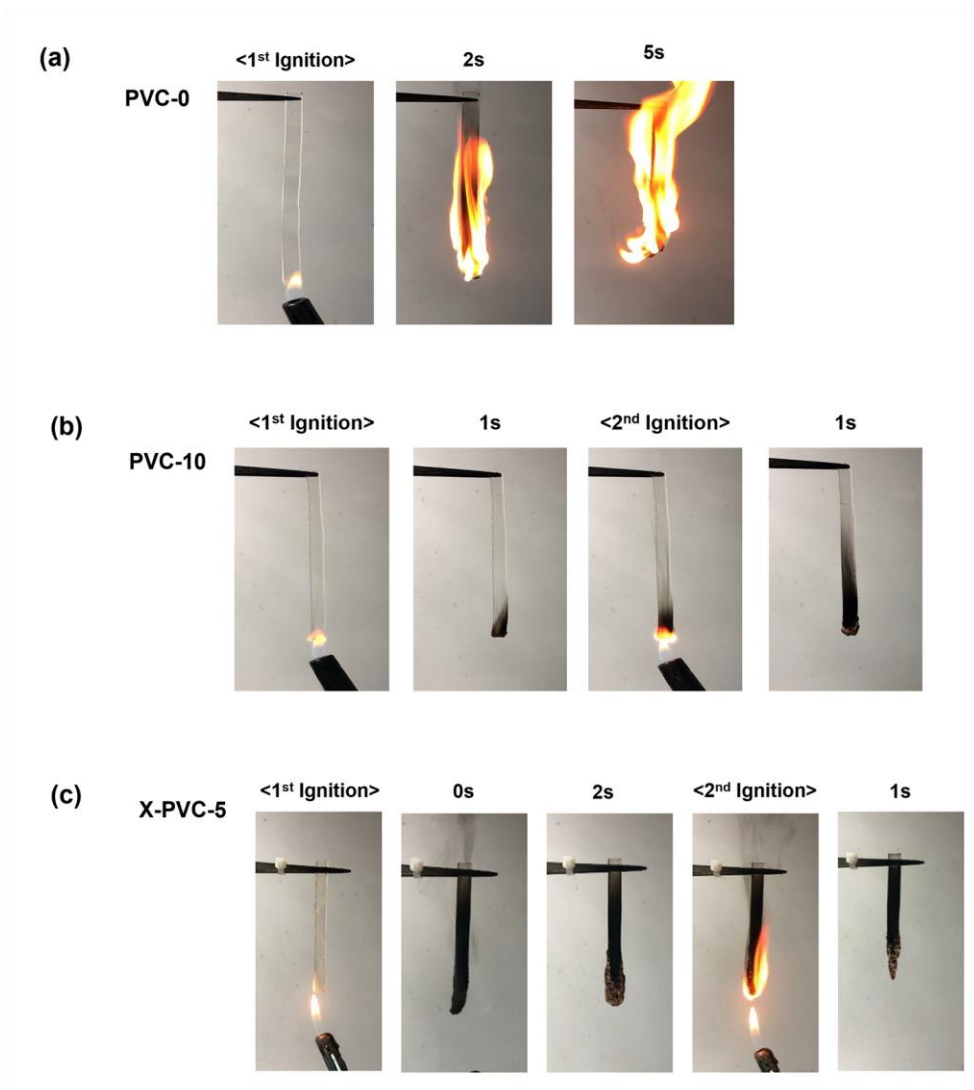


Figure 3.16. Digital photographs of burning process for (a) PVC-0, (b) PVC-10, and (c) X-PVC-5

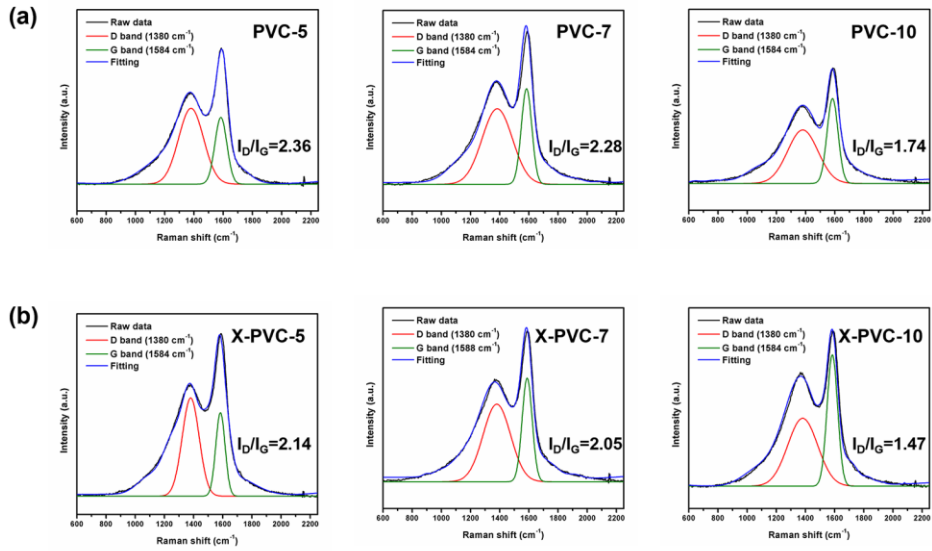


Figure 3.17. Raman spectra for residual char of the (a) PVC films and the (b) X-PVC films

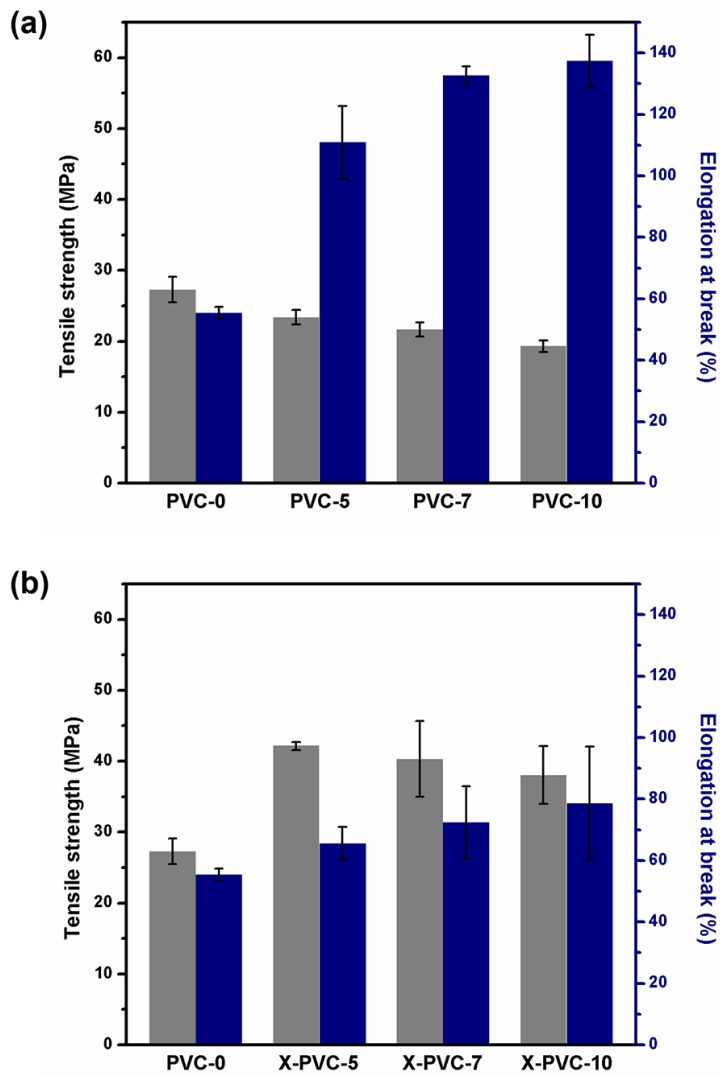


Figure 3.18. Tensile test results of the (a) PVC and (b) X-PVC films

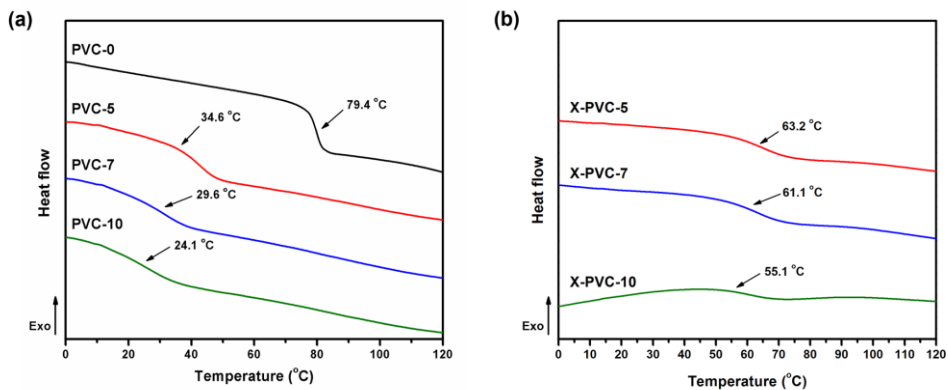


Figure 3.19. Glass transition temperatures (T_g) of the (a) PVC films and (b) X-PVC films from DSC thermograms

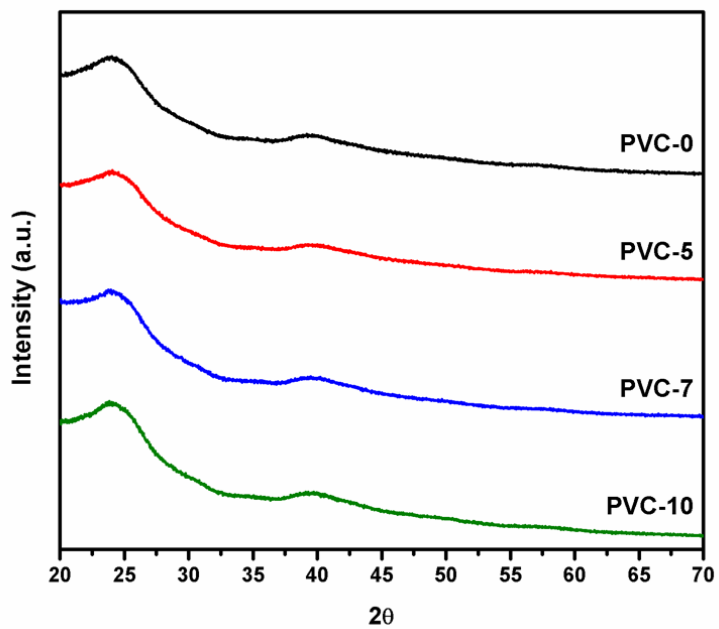


Figure 3.20. XRD patterns of the PVC films

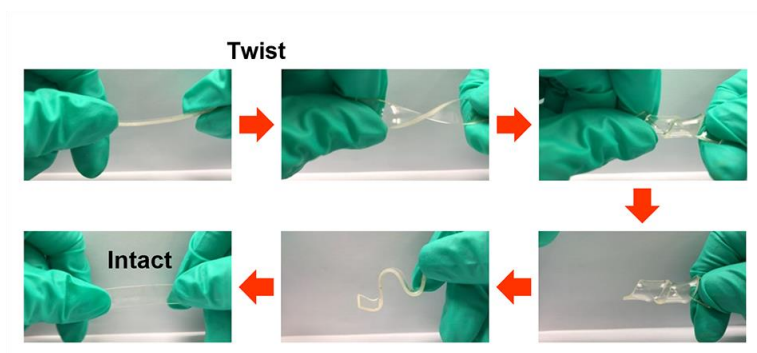


Figure 3.21. Digital photographs of X-PVC-10 under various deformation conditions

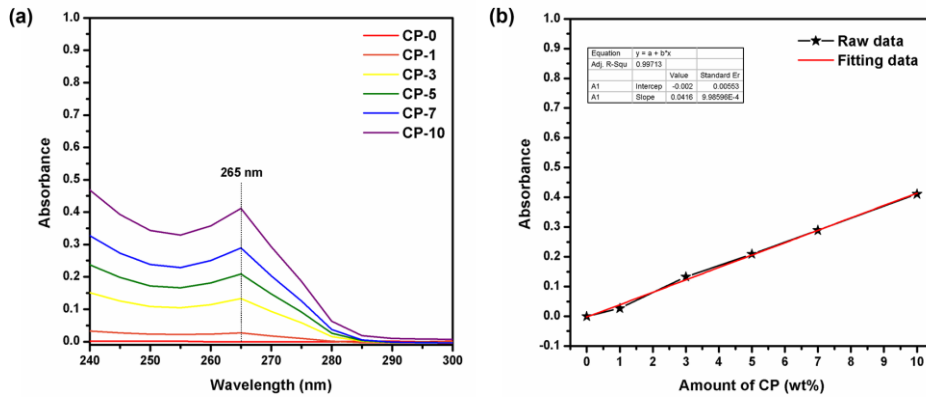


Figure 3.22. Calibration curve based on the UV absorption at 265 nm against amount of CP

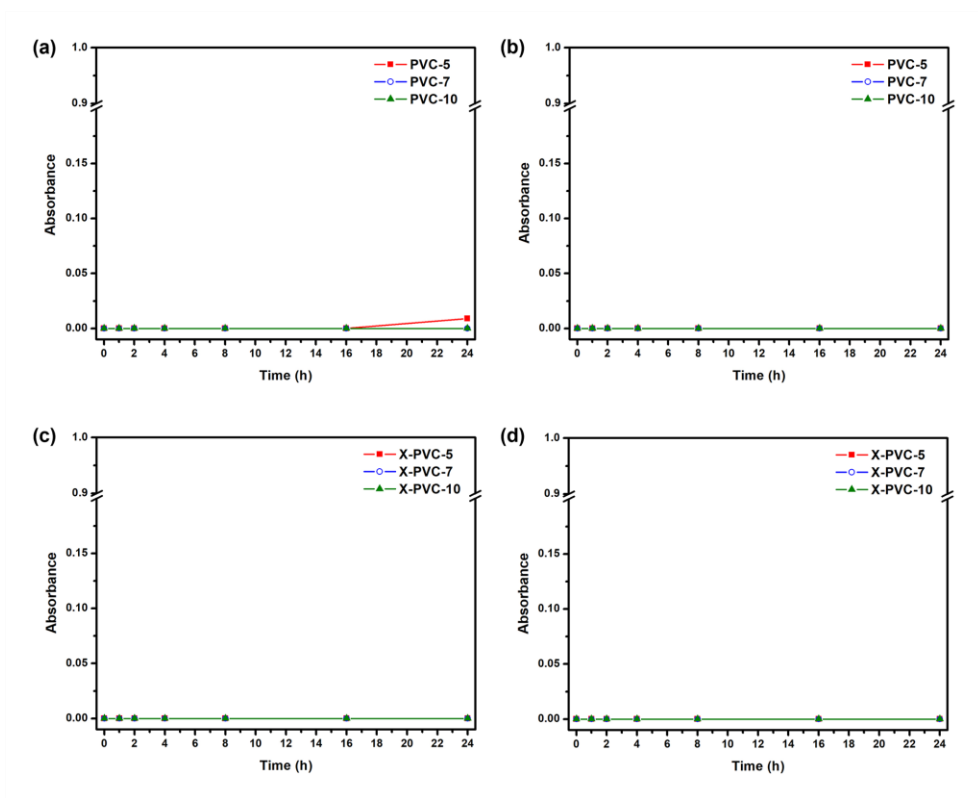


Figure 3.23. Migration stability test of the PVC films in (a) n-hexane and (b) distilled water; migration stability test of the X-PVC films in (c) n-hexane and (d) distilled water

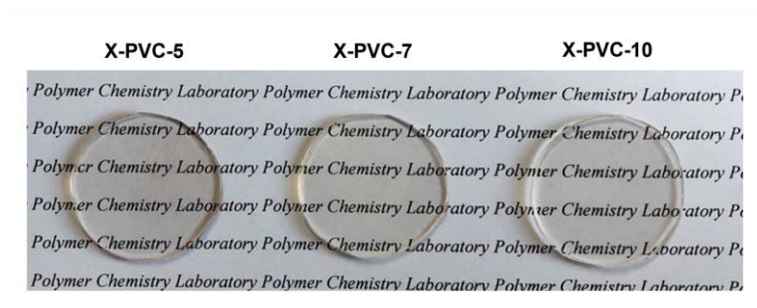


Figure 3.24. Digital photographs of the X-PVC films

Chapter 4

Controllable surface functionalization of boron nitride by heat treatment and its effect on flame retardancy of poly(lactic acid)

4.1. Introduction

Since Novoselov and Geim reported that graphene could be successfully isolated from graphite via the Scotch tape method [1], two-dimensional (2D) materials have attracted tremendous research attraction owing to their attractive features compared to those of their bulk form [2, 3]. Among 2D materials, boron nitride (BN), which is a structural analogue of graphene, has been widely investigated for various applications [4-7]. BN consists of a sp^2 honeycomb network with alternating boron and nitrogen atoms, and the B–N bond with partially ionic character endows BN with unique properties, such as electrical insulation, high thermal conductivity, and outstanding chemical and thermal stability [8-11]. Consequently, these properties have provided a driving force for the application of BN as a promising filler for high-performance nanocomposites.

Typically, BN with functional groups, such as –OH and –NH₂ (f-BN), is prepared by the mechanical exfoliation of bulk hexagonal boron nitride (h-BN), such as ultrasonication, ball milling, or liquid exfoliation [12, 13]. Although these methods can be used to prepare f-BN with high crystallinity and small lateral size, certain factors, such as relatively long reaction time

and low yield, have limited the further application of these methods [14]. In contrast, the pyrolysis of boron and nitrogen precursors, which is one of the bottom-up synthetic strategies, has been introduced as an effective method for preparing f-BN owing to its simple and large-scalable process [15]. However, despite the various available synthetic strategies for f-BN, the low functionalization efficiency of f-BN, which induces an aggregation of f-BN in nanocomposites, has limited the further application of these methods. Particularly, the further surface functionalization of f-BN is imperative to enhance their dispersion within nanocomposites to enhance their performance. Although several studies have investigated the surface functionalization of f-BN, they focused on non-covalent surface functionalization, and only a considerably low functionalization degree of approximately 5% has been achieved to date [16-18].

In this study, we described a facile functionalization method of f-BN using L-lactic acid under heat treatment. To increase the surface functionalization degree, first, f-BN was synthesized via a pyrolysis process at 800 °C, after which the sample was subjected to further surface functionalization using L-lactic acid under various heating conditions. The observation of the sample revealed that the mixing of f-BN and L-lactic acid resulted in the grafting of L-lactic acid on f-BN via amidation regardless of heating condition. In

addition, we observed that another reaction site was activated at heat treatment temperatures above 90 °C, which resulted in a significant increase in the degree of functionalization of f-BN. This report systematically addresses the routes involved in the functionalization of f-BN using L-lactic acid by heat treatment. Additionally, f-BN and L-BN were incorporated into poly(lactic acid), PLA, in order to evaluate the effect of functionalization of f-BN on flame retardancy.

4.2. Experimental

Materials

Commercially available boron nitride, boric acid, melamine, and L-lactic acid were purchased from Sigma-Aldrich. Ethanol, N,N-dimethylformamide, ethyl acetate, acetone, isopropyl alcohol, chloroform, and n-hexane were purchased from Daejung chemical & metals. Poly(lactic acid) (PLA, 4023D) resin was purchased from NatureWorks. All the other reagents and solvents were used without further purification.

Synthesis of boron nitride (f-BN)

The boron nitride with functional groups (f-BN) was synthesized as follows: In a round-bottomed flask, boric acid was dissolved in ethanol with stirring. After that, melamine was added into the flask and the mixture was vigorously stirred for 24 h. Then, the precursor, which was a white powder was filtered and dried at 50 °C for 48 h. The f-BN was obtained by calcination in a horizontal furnace under N₂ at 800 °C for 1 h.

Preparation of L-BN

To improve the dispersity of f-BN, the further surface modification of f-BN was carried out using L-lactic acid as follows: In a vial, f-BN (100 mg) was mixed with a solution of L-lactic acid (100 mg) in N,N-dimethylformamide (5 mL). The mixture was stirred at 25, 50, 90, and 120 °C for 24 h. Subsequently, the crude product was washed using ethyl acetate and acetone sequentially, and dried at 50 °C for 48 h to obtain L-BN.

Preparation of PLA nanocomposites

The PLA nanocomposites with f-BN and L-BNs were prepared as follows: In a vial, f-BN or L-BNs was dispersed in chloroform under ultrasonication for 1 h. Then, the dispersed f-BN or L-BNs solutions were mixed with a solution of PLA in chloroform. The mixture was vigorously stirred for 1 h, and then was poured into glass mold. Next, the samples were dried at room temperature for 48 h and were dried 60 °C in oven to remove the solvent completely. As a control sample, the PLA nanocomposites with commercially available BN was prepared via the same preparation steps as

the PLA nanocomposites with f-BN or L-BNs.

Characterization

Fourier transform infrared (FTIR) spectra were collected using a Bruker Alpha-Platinum attenuated total reflectance (ATR)-FTIR spectrometer over the range 4000–400 cm^{-1} . X-ray diffraction (XRD) patterns were obtained using a Malvern Panalytical Empyrean diffractometer using $\text{Cu K}\alpha$ radiation. The morphology of the sample was observed using a JEOL JSM-7601F PLUS field emission scanning electron microscope (FE-SEM) and a Tecnai G2 F3 S-Twin transmission electron microscopy (TEM). Thermogravimetric analysis (TGA) was performed using a Perkin Elmer TGA 4000 instrument from room temperature to 500 $^{\circ}\text{C}$ at a heating rate of 10 $^{\circ}\text{C min}^{-1}$ under N_2 atmosphere. X-ray photoelectron spectrometry (XPS) was performed using Thermo Scientific K-alpha. ^1H Nuclear magnetic resonance (^1H NMR) spectra were recorded on a Bruker AVANCE-400 MHz NMR spectrometer using $\text{DMSO-}d_6$ as the solvent. The solid-state NMR data were observed using 2.5 mm CPMAS probes and 500 MHz Bruker AVANCE III HD NMR spectrometer. The dispersion state of fillers was observed using a scanning

electron microscope-energy dispersive X-ray spectrometer (SEM-EDS). The limiting oxygen index (LOI) was measured using an FESTECC FT-LOI-404 LOI tester according to ASTM D2863 standard. The sample size was 100 mm × 10 mm × 1.5 mm. The differential scanning calorimetry (DSC) measurements were performed under a N₂ using a Discovery DSC 25. The samples were heated from 0 °C to 200 °C at a heating rate of 10 °C min⁻¹. The tensile strength and elongation at break were obtained by QM100S universal testing machine (UTM) with a crosshead speed of 5 mm min⁻¹. The experiments were carried out according to ASTM D638 standard at room temperature, five times for each sample.

4.3. Results and discussion

In this study, f-BN was synthesized via the pyrolysis of boric acid (B source) and melamine (N source). Briefly, f-BN precursor was prepared by adding melamine into boric acid in ethanol at room temperature. Subsequently, the obtained precursor, which was a white powder, was calcinated in a horizontal furnace under N₂ at 800 °C for 1h (Figure 4.1a). Peaks were observed in the Fourier transform infrared (FTIR) spectrum of the f-BN sample at 1370 and 790 cm⁻¹, which were attributed to the typical stretching vibration of B–N and B–N–B bonds, respectively, demonstrating the successful synthesis of f-BN (Figure 4.1b). In addition, f-BN exhibited broad peaks at approximately 1000 and 3300 cm⁻¹, which were ascribed to B–O and –OH/–NH₂, respectively, indicating the presence of B–OH and B–NH₂ groups in the synthesized f-BN. Transmission electron microscopy (TEM) revealed that the synthesized f-BN exhibited a sheet-structured morphology with an interlayer distance of 0.33 nm, which was assigned to the (002) plane of typical BN (Figure 4.1c) [19]. Figure 4.2 shows the X-ray diffraction (XRD) patterns of commercially available BN and the synthesized f-BN. Two major peaks were observed in the XRD pattern of f-

BN, which were contributed to the (002) and (100) planes. Compared to the commercially available BN, the broadening of the diffraction peaks of f-BN corresponded to a remarkable decrease in its crystallinity. Combined with the FTIR results, this result indicates that the f-BN prepared used pyrolysis exhibited a turbostratic structure, and contained functional groups, such as B–OH and B–NH₂.

To improve the dispersion of f-BN to enhance its application in nanocomposites, the surface of f-BN was further functionalized using L-lactic acid under various heating conditions: the samples were named L-BN-x (where x is the heat treatment temperature). Typically, L-BN samples were prepared by simply mixing a suspension of f-BN (100 mg) with a solution of L-lactic acid (100 mg) in dimethylformamide (DMF; 5mL). Subsequently, the mixture was stirred at 25, 50, 90, and 120 °C for 24 h, after which the crude product was washed four times using ethyl acetate and acetone sequentially, to remove nongrafted L-lactic acid. To investigate the degree of functionalization of L-BNs, thermogravimetric analysis (TGA) was performed (Figure 4.3a and Figure 4.4). The TGA results revealed that the thermal decomposition of f-BN started at 180 °C, and the weight loss at 500 °C was approximately 7%. In order to confirm the cause of this weight loss, we carried out FTIR analysis for f-BN which was heated to 500 °C via

TGA. As shown in Figure 4.5, the FTIR spectra of f-BN show that the broad peak at around 3300 cm^{-1} ascribed to OH and NH groups were disappeared after heat treatment to $500\text{ }^{\circ}\text{C}$. It implied that the weight loss of 7% at $500\text{ }^{\circ}\text{C}$ which was observed in TGA result of f-BN was attributed to the functional groups on the surface of f-BN, such as B–OH and B–NH₂. Next, the degree of functionalization of L-BNs was calculated based on the thermal degradation behavior of f-BN. The results revealed that the heat treatment induced a notable increase in the functionalization degree of L-BNs (Figure 4.3a). For example, compared to that of L-BN-25 (6.9%), the surface functionalization degree of L-BN-50 and L-BN-90 significantly increased to 13.8 and 26.4%, respectively. In addition, L-BN-90 and L-BN-120 exhibited almost similar degree of functionalization, suggesting that the functionalization efficiency was saturated at temperatures above $90\text{ }^{\circ}\text{C}$. This will be further discussed later in this paper.

First, to investigate the covalent surface functionalization of f-BN by L-lactic acid, we performed the ^1H nuclear magnetic resonance (NMR) analysis of the crude product. To prepare the ^1H NMR sample, a solution of the crude product (0.2 mL) was mixed with dimethyl sulfoxide (DMSO)-d₆ solvent (0.8 mL). At this time, both L-BNs and nongrafted L-lactic acid were present in the crude product. Two peaks were observed at 1.23 and

4.04 ppm in the ^1H NMR spectrum of L-lactic acid (Figure 4.6). In the case of L-BN-25 and L-BN-50, the intensity of the peak at 1.23 ppm, which corresponded to the methyl group of L-lactic acid, decreased, and a new peak emerged at 1.14 ppm. This observation is consistent to that of a previous study that reported that when alkyl alcohol was introduced to the surface of boron nitride nanotube (BNNT), there is an up-field movement in the chemical shift of protons closer to BNNT in the ^1H NMR spectrum [20]. Therefore, the upward chemical shift from 1.23 to 1.14 ppm corresponded to the covalent reaction of L-lactic acid with f-BN. Furthermore, the peak at 1.23 ppm completely disappeared in the ^1H NMR spectra of L-BN-90 and L-BN-120, and small peaks emerged at approximately 1.11 ppm. Moreover, there was a slight decrease in the intensity of the peak at 4.04 ppm, which was ascribed to the proton on the carbon adjacent to the $-\text{OH}$ of L-lactic acid, and a new peak emerged at 3.80 ppm. This corresponded to the additional secondary reaction between the $-\text{OH}$ of L-lactic acid and f-BN that occurred at temperatures above $90\text{ }^\circ\text{C}$ in addition to the functionalization reaction that occurred in L-BN-25 and L-BN-50.

Next, to clarify the further functionalization on f-BN with L-lactic acid, FTIR analysis of L-BNs was performed (Figure 4.3b and Figure 4.7). All the L-BN samples exhibited the characteristic peaks at 1370 and 780 cm^{-1} ,

which were ascribed to B–N and B–N–B bonds, respectively. Also, the peak at 1122 cm^{-1} attributed to C–O bonds of L-lactic acid was appeared, indicating that the surface functionalization was successfully processed. In addition, compared to that of f-BN, a new C=O peak was observed in the FTIR spectra of the L-BN sample at approximately 1670 cm^{-1} , which was ascribed to the amide group [21], verifying the successful further surface functionalization via the amidation reaction between the –COOH of L-lactic acid and the B–NH₂ of f-BN regardless of the heating conditions. Furthermore, an additional peak corresponding to the C=O of carboxylic acid group was observed at 1720 cm^{-1} in the FTIR spectra of L-BN-90 and L-BN-120, indicating the presence of free carboxylic acid groups on the surface of L-BN-90 and L-BN-120. Therefore, we believed that at high temperatures, L-lactic acid was grafted onto f-BN via other activation sites in addition to the amidation reaction that occurred at low temperature, which is consistent with the ¹H NMR results. Accordingly, X-ray photoelectron spectroscopy (XPS) was performed to further determine the heat treatment-induced additional functionalization route. Compared to f-BN (Figure 4.8), a small peak was observed in the N_{1s} spectrum of L-BN-25 and L-BN-50 at 398.9 eV, which corresponded to N–C bonds, whereas there was no difference in the B_{1s} spectrum (Figure 4.9a-b and Figure 4.10). This

indicated that the N atom of the B-NH₂ groups on f-BN was the only reaction site at a relatively low temperature via the amidation reaction with -COOH of L-lactic acid. In contrast, the XPS profiles of L-BN-90 and L-BN-120 exhibited an additional peak at 193.0 eV, which was ascribed to the B-O bond, suggesting that the B atom in the B-OH groups of f-BN was an additional reaction site at high temperatures (Figure 4.9c and Figure 4.10c). The B-O bonds in these samples exhibited a higher binding energy than the B-O bonds observed in the spectrum of f-BN. This could be attributed to the introduction of highly electronegative C atom on B atom by the formation of boronate ester between the -OH of L-lactic acid and the B-OH of f-BN at heat treatment temperatures above 90 °C [22], which is consistent with the FTIR results. Furthermore, a small peak attributed to -NH₂ was observed at 401.2 eV in the N_{1s} spectra of L-BN-90 and L-BN-120 (Figure 4.9d and Figure 4.10d), which corresponded to the formation of boronate ester by the reaction of oxygen species with the B atom of f-BN [23, 24]. These results indicated that while an amidation reaction was the only reaction that occurred in the surface functionalization of f-BN with L-lactic acid under heat treatment at lower temperatures, both amidation and boronate ester formation reactions simultaneously occurred at higher temperatures, which in turn, increased the surface functionalization degree of L-BN. These

results were also shown in solid-state NMR analysis (Figure 4.11). In the case of f-BN, the one broad peak was observed at around 6.8 ppm, which means that B–OH and B–NH₂ groups were overlapped. Compared with f-BN, a small peak attributed to –OH of L-lactic acid appeared at around 1.1 ppm, indicating the surface functionalization of L-lactic acid onto f-BN in the NMR spectra of L-BN-25 and L-BN-50. In the case of L-BN-90 and L-BN-120, a new peak at around 2.6 ppm was additionally observed. This peak was ascribed to –COOH of L-lactic acid. These results were coincident with other results.

This boronate ester formation by heat treatment was further confirmed by the reaction between boric acid and L-lactic acid. To this end, a solution of boric acid (100 mg) in DMF was mixed with a solution of L-lactic acid (145 mg) at 25 or 90 °C. Subsequently, the reaction mixture was stirred for 24 h, after which the mixture was washed four times using chloroform and acetone to remove unreacted L-lactic acid. The main difference between the products obtained at 25 and 90 °C is underlined in Figure 4.12. At 25 °C, the FTIR spectrum of the product was similar to that of boric acid, indicating that no reaction occurred between boric acid and L-lactic acid at 25 °C. In contrast, at 90 °C, characteristic absorption peaks were observed at 1720 and 1279 cm⁻¹, which were ascribed to the C=O of carboxylic acid group

and B–O–C, respectively. Considering that the C=O of L-lactic acid should shift a higher wavenumber when L-lactic acid participates in reactions, such as esterification [25], the –COOH of L-lactic acid should not react with the B–OH of boric acid. Therefore, this verifies that the heat treatment at temperatures above 90 °C resulted in a boronate ester formation reaction between the –OH of L-lactic acid and B–OH of boric acid, which is consistent with the aforementioned results.

Based on the aforementioned analysis, we propose the routes of the further functionalization of f-BN using L-lactic acid via heat treatment (Figure 4.13). In this study, the reaction sites of f-BN were B–OH and B–NH₂ groups, and those of L-lactic acid were –COOH and –OH groups. At a relatively low temperature, a single functionalization occurred via the amidation reaction between the –COOH of L-lactic acid and the B–NH₂ of f-BN. With an increase in the heat treatment temperature, secondary functionalization occurred via boronate ester formation reaction by the activation of additional reaction sites. Consequently, two functionalization mechanisms were occurred simultaneously at high temperatures, resulting in the high functionalization degree. In addition, the additional functionalization reaction had no effect on the sheet-structured morphology of L-BNs (Figure 4.13). This indicates that the further surface

functionalization by L-lactic acid had no effect on the physical structure of f-BN. Finally, to investigate the effect of further functionalization on dispersion state, we performed the dispersion test in various solvents (water, IPA, chloroform, and n-hexane). Each sample (5 mg) was dispersed in various solvents (5 mL) via ultrasonication for 1 h and observed for 1 day (Figure 4.14). As expected, all the samples showed aggregation and sedimentation in n-hexane and chloroform in just 1 hours. In contrast, in IPA and water, while f-BN exhibited complete sedimentation after 1 day, the dispersions of L-BNs remained stable over 1 day except L-BN-25. These results indicate that further surface functionalization of f-BN with L-lactic acid improves dispersion stability. In particular, L-BN functionalized with a relatively large amount of L-lactic acid by heat treatment enables fine dispersion, which is suitable for application as a nanofiller.

In order to analyze the effect of degree of functionalization of f-BN on flame retardancy, the PLA nanocomposites were prepared by incorporating f-BN and L-BNs into the PLA as polymer matrix. At this time, among the L-BNs samples, L-BN-25 and L-BN-90 were chosen for comparison. The PLA nanocomposites were denoted as PLA-#fBN (PLA nanocomposites with f-BN), PLA-#LBN25 (PLA nanocomposites with L-BN-25), and PLA-#LBN90 (PLA nanocomposites with L-BN-90), and # is the weight

percentage of fillers. To investigate the dispersion state of fillers in the PLA matrix, SEM analysis and SEM-EDS mapping were used for the PLA nanocomposites. As seen in Figure 4.15, while the PLA showed the smooth surface, the PLA nanocomposites with 3.0 wt% fillers exhibited rougher surface, demonstrating that f-BN, L-BN-25, and L-BN-90 were uniformly dispersed in the PLA. From SEM-EDS, all the PLA nanocomposites showed the well-dispersed boron atoms without agglomerates, which reveals the homogeneous dispersion of f-BN, L-BN-25, and L-BN-90.

To evaluate the flame retardancy of the PLA nanocomposites, a limiting oxygen index (LOI) measurement were carried out as a tool to investigate the flame retardancy of polymeric materials. The LOI values of the PLA nanocomposites were illustrated in Figure 4.16. For comparison, the PLA nanocomposites with commercially available BN (PLA-#BN) was additionally fabricated via the same preparation steps as the PLA-#fBN. The LOI value of the PLA was 19.0%, which is similar to the LOI value of the PLA reported previously. It was found that the LOI values of PLA-BN were not significantly different with those of the PLA. In contrast, with incorporating 3 wt% f-BN into the PLA, the LOI value of the PLA was increased to 23.0%. It indicates that f-BN could further improve the flame retardancy of the PLA compared to commercially available BN. It can be

explained the dispersion state of fillers in PLA. As seen in Figure 4.17, PLA-3.0BN showed the smooth surface with some agglomerates, which demonstrates the poor dispersion state of commercially available BN in PLA. Thus, since f-BN has functional groups such as $-OH$ and $-NH_2$, it interacts with PLA via hydrogen bond, resulting in good dispersion state and enhanced flame retardancy. In addition, the LOI values of PLA-LBN25 were more increased in comparison with those of PLA-fBN. For example, while the LOI values of PLA-1.0fBN and PLA-3.0fBN were 21.0% and 23.0%, it increased to 23.8% and 24.2% for PLA-1.0LBN25 and PLA-3.0LBN25, respectively. It might be contributed to further improved dispersion state by surface functionalization. However, although L-BN-90 showed better dispersion state than L-BN-25, the LOI values of PLA-LBN90 were rather decreased compared to those of PLA-LBN25. Maybe, as the degree of functionalization increases, the content of carbon and oxygen increases, which is a factor that reduces flame retardancy. Consequently, when L-BN-25 was introduced into PLA, it showed the best performance in terms of flame retardancy.

4.4. Conclusion

In conclusion, this study introduced an efficient surface functionalization strategy for f-BN. f-BN was synthesized via the calcination of melamine-boric acid complex and functionalized using L-lactic acid under various heating conditions. The results revealed that the functionalization of f-BN by L-lactic acid occurred via two distinct functionalization routes: a single functionalization route occurred at low temperature conditions, whereas two functionalization routes occurred simultaneously at high temperature conditions, with the sample achieving a high functionalization degree of up to 26%. As this study systematically revealed the surface functionalization routes of f-BN under various heating conditions and controlled the degree of functionalization, which have not been previously reported to the best of our knowledge, we believe that the facile and efficient strategy introduced in this study would be attractive for the preparation of BN for nanocomposites. Additionally, to confirm the effect of the functionalization degree of L-BN on flame retardancy, L-BN-25 and L-BN-90 were introduced into PLA as polymer matrix. Although L-BN-90 has higher functionalization degree than L-BN-25, lower flame retardancy was found compared to L-BN-25. These

results might be contributed to the increase in the amount of carbon and oxygen by high functionalization efficiency. Consequently, when L-BN-25 was introduced into PLA, it showed the best performance in terms of flame retardancy.

4.5. References

1. Novoselov, K.S., et al., *Electric field effect in atomically thin carbon films*. Science, 2004. **306**(5696): p. 666-669.
2. Zhang, K., et al., *Two dimensional hexagonal boron nitride (2D-hBN): synthesis, properties and applications*. Journal of Materials Chemistry C, 2017. **5**(46): p. 11992-12022.
3. Shin, H., et al., *Improving physical properties of polypropylene nanocomposites by a natural resource-based bottom-up graphene oxide filler*. Macromolecular Research, 2021. **29**(7): p. 487-493.
4. Paine, R.T. and C.K. Narula, *Synthetic routes to boron nitride*. Chemical Reviews, 1990. **90**(1): p. 73-91.
5. Li, X., et al., *Hexagonal boron nitride nanosheet as an effective nanoquencher for the fluorescence detection of microRNA*. Chemical Communications, 2021. **57**(65): p. 8039-8042.
6. Rosely, C.S., et al., *Phytic acid modified boron nitride nanosheets as sustainable multifunctional nanofillers for enhanced properties of poly (L-lactide)*. ACS Sustainable Chemistry & Engineering, 2020. **8**(4): p. 1868-1878.
7. Kong, S., et al., *Improvement in mechanical and thermal properties of polypropylene nanocomposites using an extremely small amount of alkyl chain-grafted hexagonal boron nitride nanosheets*. Polymer, 2019. **180**: p. 121714.
8. Hou, J., et al., *Preparation and characterization of surface modified*

- boron nitride epoxy composites with enhanced thermal conductivity*. RSC Advances, 2014. **4**(83): p. 44282-44290.
9. Castillo, C.T., C. Bruel, and J. Tavares, *Chemical affinity and dispersibility of boron nitride nanotubes*. Nanoscale Advances, 2020. **2**(6): p. 2497-2506.
 10. Yin, J., et al., *Boron nitride nanostructures: fabrication, functionalization and applications*. Small, 2016. **12**(22): p. 2942-2968.
 11. Li, Q., et al., *Realizing Rationally-Balanced Dielectric Properties in Fluoropolymer/Cr₂AlC MAX Composites Modified by 2D-BN*. Macromolecular Research, 2020. **28**(1): p. 1261-1267.
 12. Luo, W., et al., *Solution processed boron nitride nanosheets: synthesis, assemblies and emerging applications*. Advanced Functional Materials, 2017. **27**(31): p. 1701450.
 13. Li, L.H., et al., *Large-scale mechanical peeling of boron nitride nanosheets by low-energy ball milling*. Journal of Materials Chemistry, 2011. **21**(32): p. 11862-11866.
 14. Xiao, F., et al., *Controllable synthesis of few-layered and hierarchically porous boron nitride nanosheets*. Chemical Communications, 2016. **52**(20): p. 3911-3914.
 15. Han, R., et al., *Functionalised hexagonal boron nitride for energy conversion and storage*. Journal of Materials Chemistry A, 2020. **8**(29): p. 14384-14399.
 16. Yu, L., et al., *Improved Thermal conductivity of polymer composites by noncovalent modification of boron nitride via tannic acid chemistry*. Industrial & Engineering Chemistry Research, 2021.

- 60(34): p. 12570-12578.
17. Meng, Q., et al., *Noncovalent modification of boron nitride nanosheets for thermally conductive, mechanically resilient epoxy nanocomposites*. Industrial & Engineering Chemistry Research, 2020. **59**(47): p. 20701-20710.
 18. Lee, H., et al., *Dual functionalization of hexagonal boron nitride nanosheets using pyrene-tethered poly (4-vinylpyridine) for stable dispersion and facile device incorporation*. ACS Applied Nano Materials, 2020. **3**(8): p. 7633-7642.
 19. Bai, Y., et al., *Ball milling of hexagonal boron nitride microflakes in ammonia fluoride solution gives fluorinated nanosheets that serve as effective water-dispersible lubricant additives*. ACS Applied Nano Materials, 2019. **2**(5): p. 3187-3195.
 20. Smith, K.K., et al., *Surface modification and functionalization of boron nitride nanotubes via condensation with saturated and unsaturated alcohols for high performance polymer composites*. ACS Applied Nano Materials, 2019. **2**(7): p. 4053-4060.
 21. Sainsbury, T., et al., *Self-assembly of gold nanoparticles at the surface of amine-and thiol-functionalized boron nitride nanotubes*. The Journal of Physical Chemistry C, 2007. **111**(35): p. 12992-12999.
 22. Gupta, V., et al., *Assigning oxidation states to organic compounds via predictions from X-ray photoelectron spectroscopy: a discussion of approaches and recommended improvements*. Journal of Chemical Education, 2014. **91**(2): p. 232-238.
 23. Sainsbury, T., et al., *Oxygen radical functionalization of boron*

- nitride nanosheets*. Journal of the American Chemical Society, 2012. **134**(45): p. 18758-18771.
24. Lee, J., et al., *Boron nitride nanosheets (BNNs) chemically modified by “Grafting-From” polymerization of poly (caprolactone) for thermally conductive polymer composites*. Chemistry–An Asian Journal, 2016. **11**(13): p. 1921-1928.
25. Gupta, A., et al., *Effects of amphiphilic chitosan on stereocomplexation and properties of poly (lactic acid) nanobiocomposite*. Scientific Reports, 2018. **8**(1): p. 1-13.

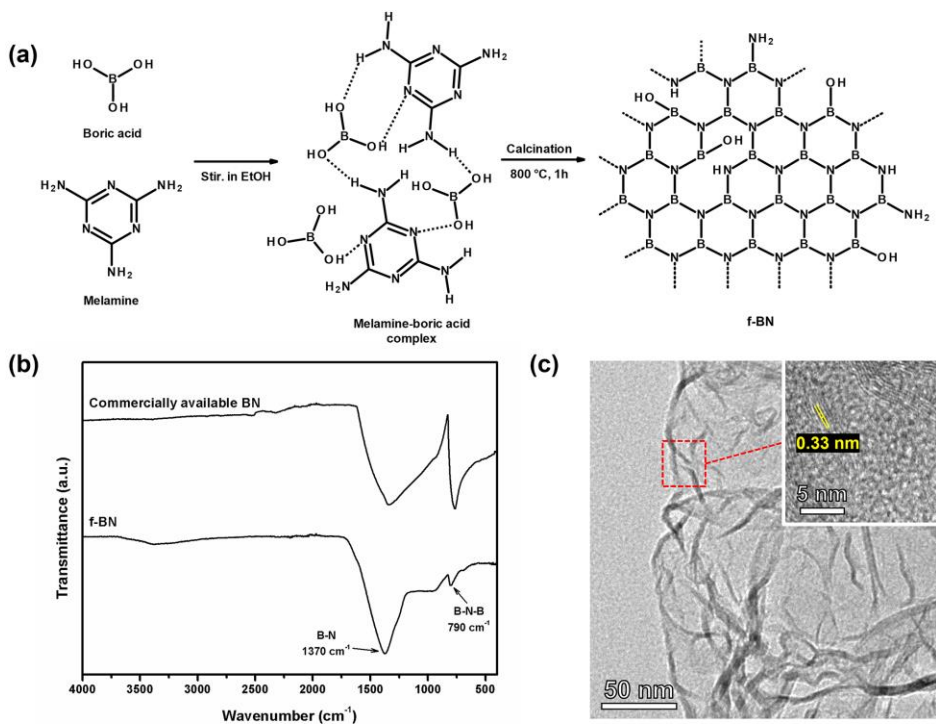


Figure 4.1. (a) Schematic illustration of the synthetic process of boron nitride with functional groups (f-BN), (b) fourier transform infrared (FTIR) spectra of commercially available BN and f-BN, and (c) transmission electron microscopy (TEM) image of f-BN (inset: high-magnification TEM image)

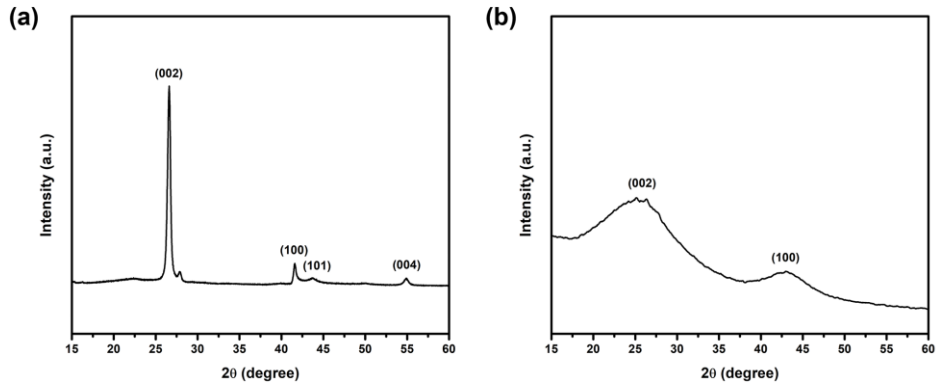


Figure 4.2. X-ray diffraction (XRD) patterns of (a) commercially available BN and (b) f-BN

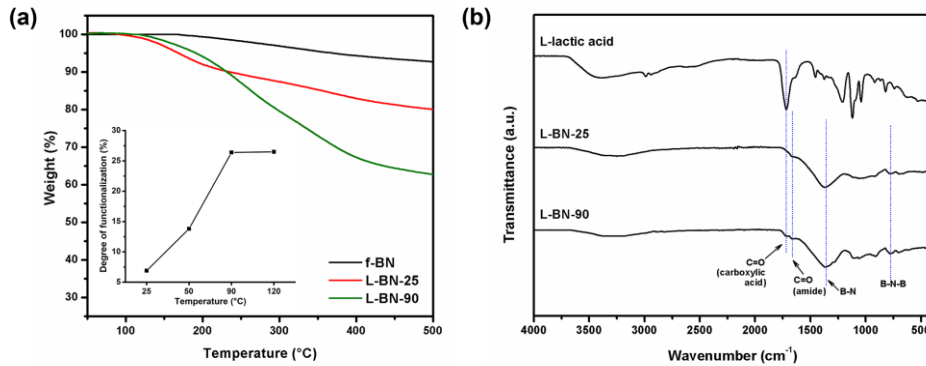


Figure 4.3. (a) Thermogravimetric analysis (TGA) curves of f-BN and L-BNs (inset: the degree of functionalization depending on heating conditions), and (b) FTIR spectra of L-BN-25, L-BN-90, and L-lactic acid

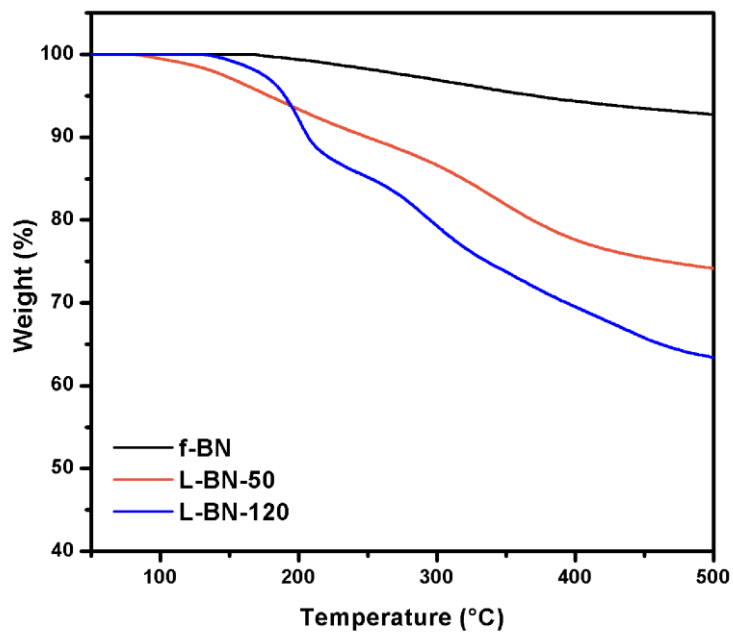


Figure 4.4. Thermogravimetric analysis (TGA) curves of f-BN, L-BN-50, and L-BN-120

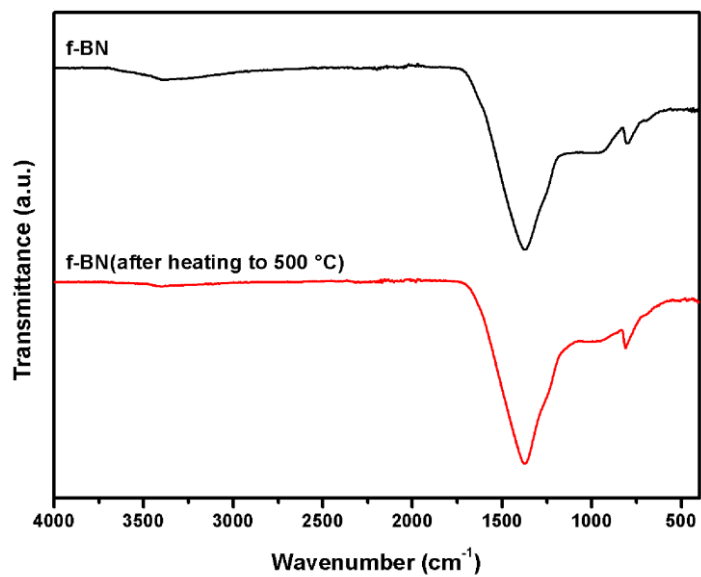


Figure 4.5. The Fourier transform infrared (FTIR) spectra of f-BN before and after heat treatment to 500 °C

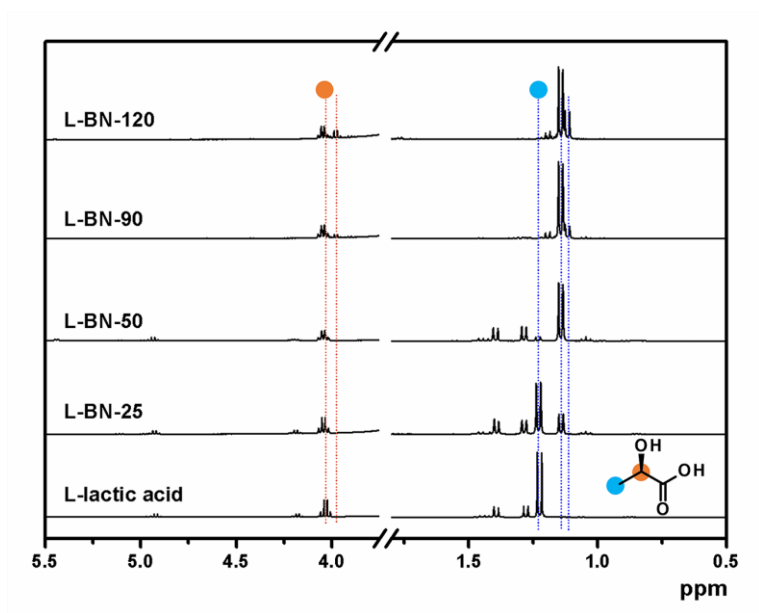


Figure 4.6. ^1H nuclear magnetic resonance (NMR) spectrum of the crude product after the further surface functionalization

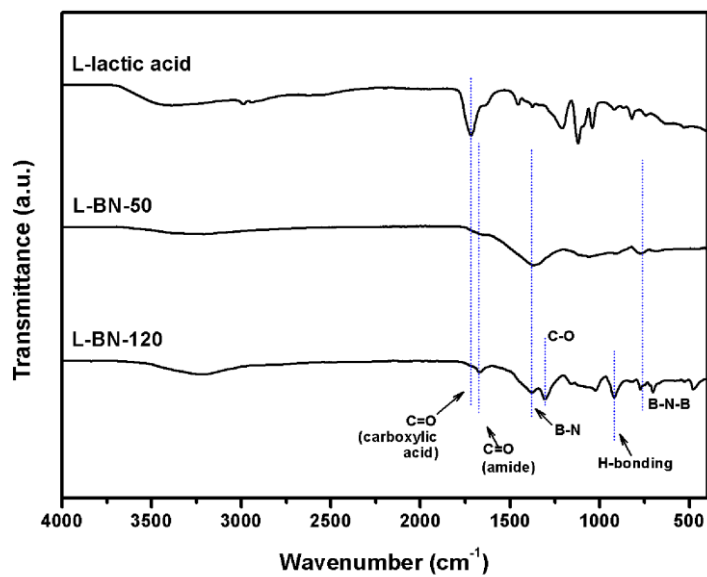


Figure 4.7. The FTIR spectra of L-lactic acid, L-BN-50, and L-BN-120

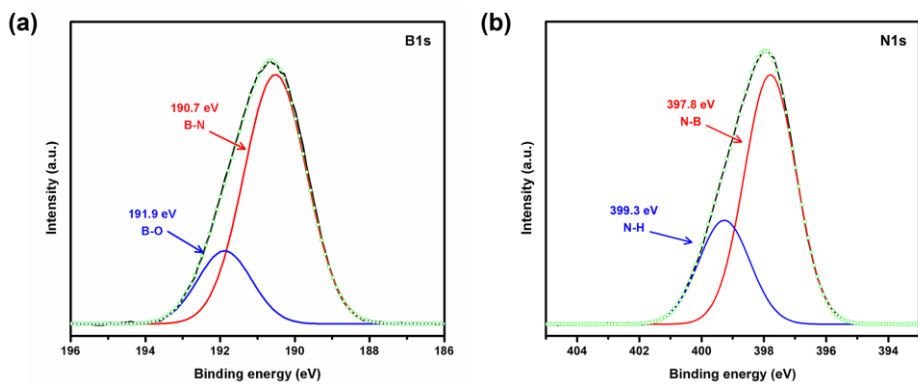


Figure 4.8. (a) B_{1s} and (b) N_{1s} X-ray photoelectron spectroscopy (XPS) profile of f-BN

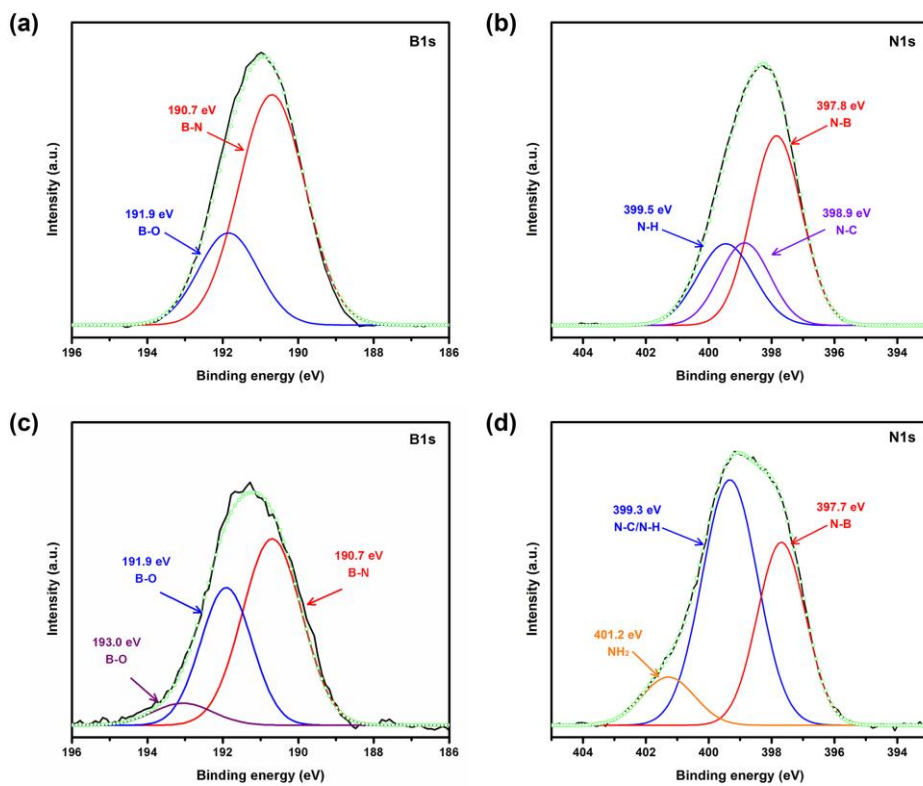


Figure 4.9. (a) B_{1s} X-ray photoelectron spectroscopy (XPS) profile of L-BN-25, (b) N_{1s} XPS profile of L-BN-25, (c) B_{1s} XPS profile of L-BN-90, and (d) N_{1s} XPS profile of L-BN-90

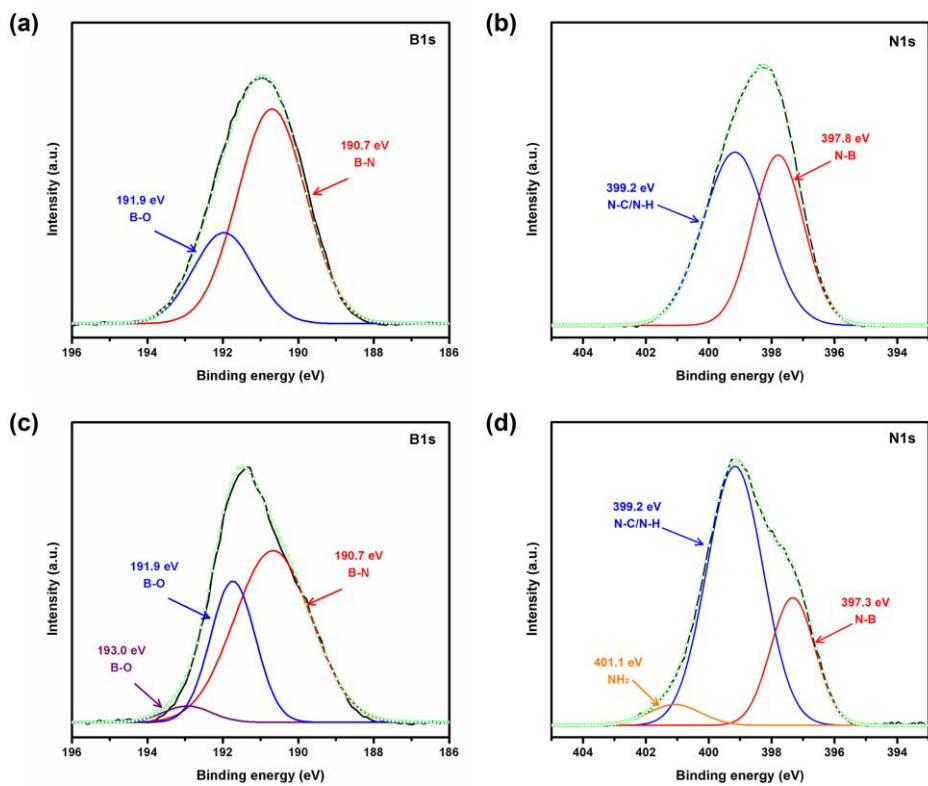


Figure 4.10. (a) B_{1s} XPS profile of L-BN-50, (b) N_{1s} XPS profile of L-BN-50, (c) B_{1s} XPS profile of L-BN-120, and (d) N_{1s} XPS profile of L-BN-120

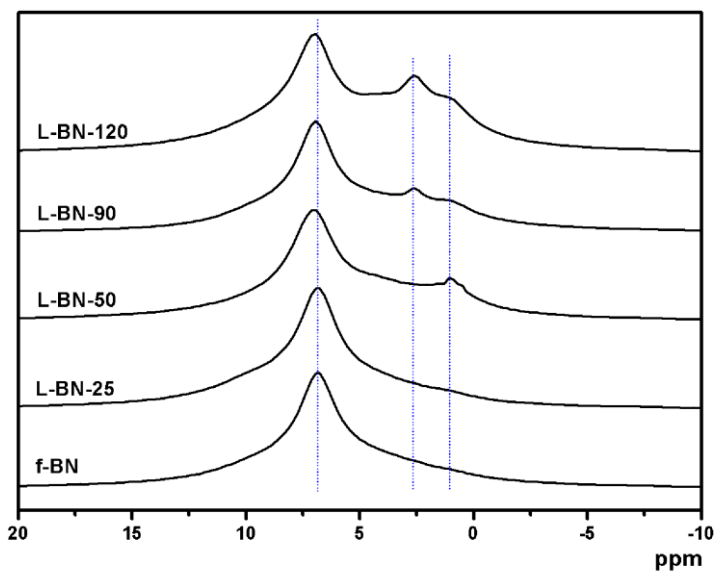


Figure 4.11. The solid-state NMR spectra of f-BN and L-BNs

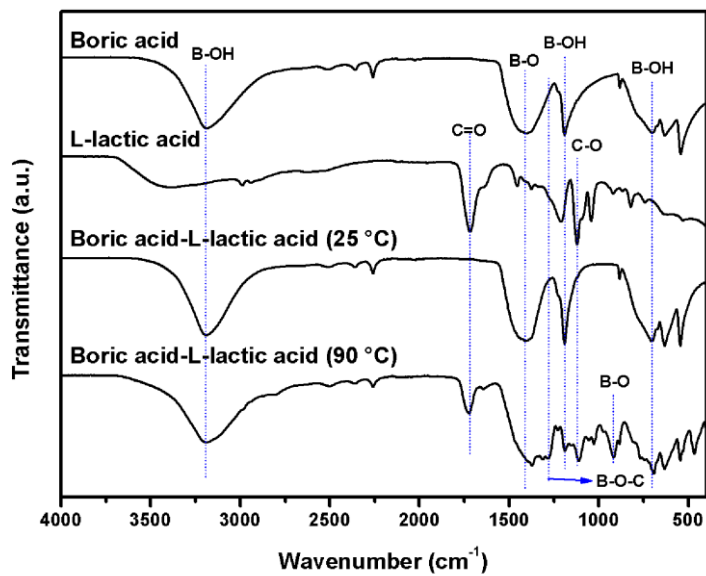


Figure 4.12. FTIR spectra of the product of the reaction between L-lactic acid and boric acid under heat treatment

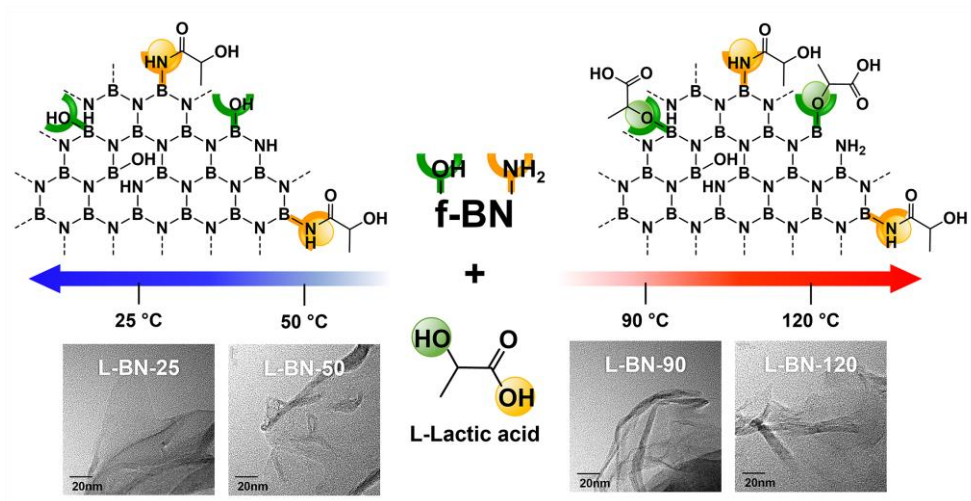


Figure 4.13. Routes of the surface functionalization of f-BN using L-lactic acid under various heating conditions

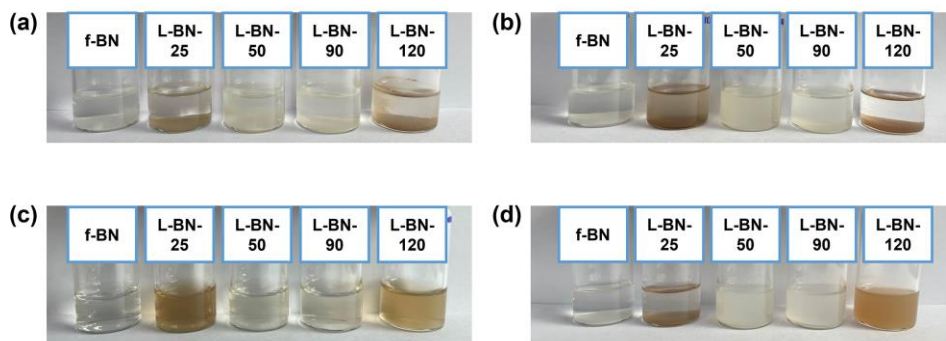


Figure 4.14. The dispersion test for f-BN and L-BNs in (a) n-hexane, (b) chloroform, (c) water, and (d) isopropyl alcohol (IPA)

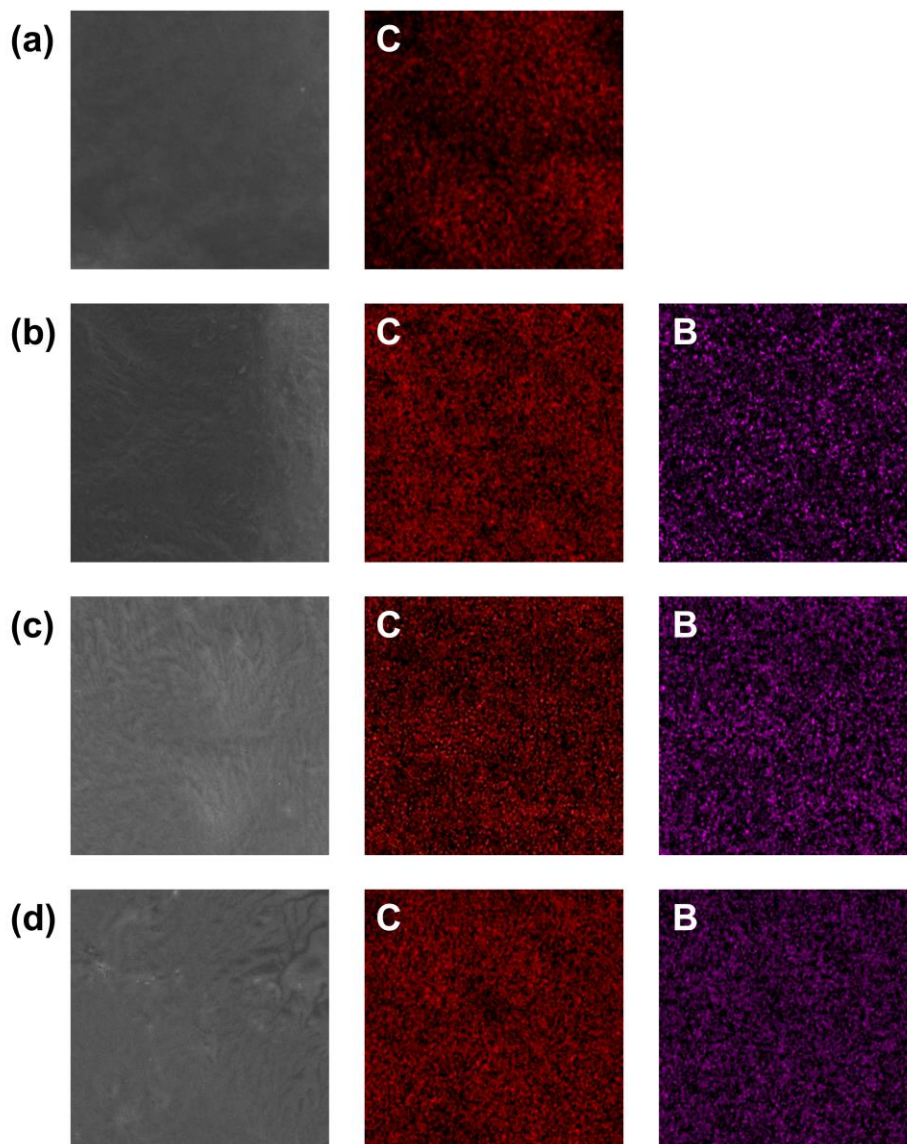


Figure 4.15. SEM images and EDS mapping of (a) PLA, (b) PLA-3.0fBN, (c) PLA-3.0LBN25, and (d) PLA-3.0LBN90

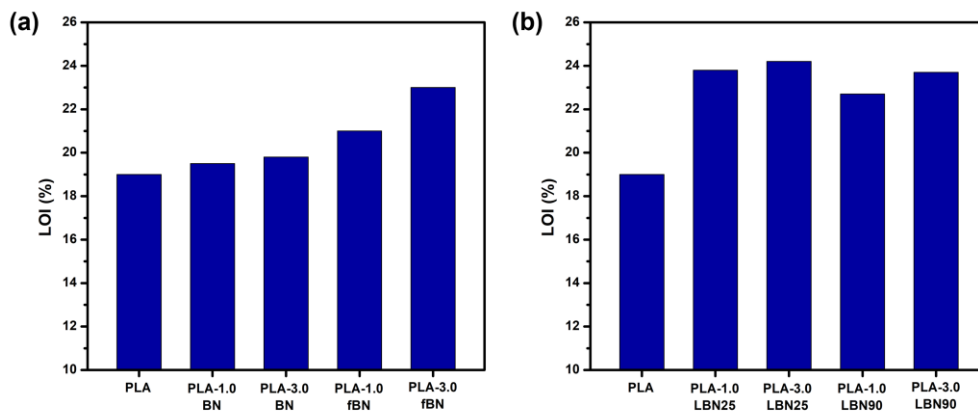


Figure 4.16. The limiting oxygen index (LOI) results (a) PLA, PLA-BN, and PLA-fBN, (b) PLA, PLA-LBN25, and PLA-LBN90

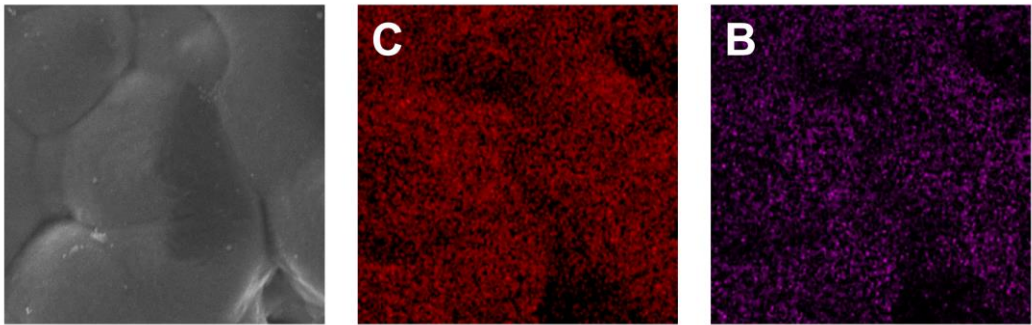


Figure 4.17. SEM image and EDS mapping of PLA-3.0BN

초 록

본 연구에서는 기 보고된 인계 난연제의 비교적 낮은 난연 성능 문제를 개선하기 위한 연구를 진행하였다. 첫째, 신규 인-질소계 난연제의 구조는 인과 질소의 시너지 효과를 통해 난연성을 극대화하도록 설계하였다. 인-질소계 난연제는 성공적으로 합성되었으며, 엔지니어링 플라스틱 중 하나인 폴리케톤에 도입하였다. 순수 폴리케톤은 20.2%의 한계산소지수 값을 가지며, 수직연소시험에서 불에 완전히 연소되는 결과를 보였다, 반면, 7 중량 퍼센트의 인-질소계 난연제가 도입된 폴리케톤은 한계산소지수 값이 25.9%까지 증가하며, 수직연소시험에서 가장 우수한 난연등급인 VTM-0 등급을 달성하였다. 즉, 본 연구를 통해 합성된 인-질소계 난연제가 폴리케톤에 우수한 난연성을 부여하였다. 이때, 인과 질소의 시너지 효과로 인한 인-질소계 난연제의 효과적인 차르(char) 형성 능력과 함께 불활성 가스의 방출이 폴리케톤의 난연성을 크게 향상시키는 것으로 나타났다.

둘째, 가교 네트워크가 인계 난연제의 난연성을 향상시킬 수 있음을 발견하였다. 자가 중합이 가능한 포스포네이트 난연제인 비스(카다닐) 페닐포스포네이트 (CP)가 성공적으로 합성되었으며, 이를

폴리염화비닐에 도입하여 성능을 평가하였다. CP 의 포스포네이트 그룹과 긴 알킬 사슬은 각각 폴리염화비닐의 난연성 및 유연성을 향상시켰다. 또한, CP 는 열처리에 의해 자가 중합이 될 수 있으며, CP 의 가교 네트워크는 안정한 차르 형성을 유도하여 폴리염화비닐의 난연성을 더욱 향상시켰다. 따라서, 자가 중합 특성을 가지는 CP 는 폴리염화비닐의 열안정성, 난연성, 그리고 유연성을 동시에 향상시키는 전도유망한 물질이라고 할 수 있다.

마지막으로, 2 차원의 층상 무기 재료 중, 질화붕소는 전기 절연성과 우수한 화학적 및 열적 안정성 등의 특성을 가지고 있어 고성능 나노복합재의 충전제로써 각광받고 있다. 그러나 질화붕소의 낮은 표면 개질 효율로 인해 발생하는 질화붕소의 심각한 응집현상은 이의 응용 범위를 제한한다. 따라서, 고분자 나노복합재 내의 질화붕소의 분산성을 향상시키기 위해, 본 연구에서는 질화붕소의 합성 및 기능화 방법을 제안하였다. 멜라민-붕산 복합체의 열처리 공정을 통해 얻어진 작용기를 가지는 질화붕소는 L-락트산을 사용하여 추가로 개질되었다. 연구 결과, L-락트산이 열처리에 의한 두 가지 주요 개질 경로를 통해 질화붕소에 접목되었음을 확인하였다. 본 연구에서, 질화붕소의 개질 정도가 난연성에 미치는 영향을 조사하기 위하여, 이를 폴리락트산에 도입하여 성능을 평가하였다. 저온에서 L-락트산으로 개질된

질화붕소는 표면 개질을 통해 폴리락트산과의 수소결합을 형성하여 난연성을 더욱 향상시키는 결과를 보여주었다. 한편, 고온에서 L-락트산으로 개질된 질화붕소는 26% 이상의 개질 정도를 보유하기 때문에 상대적으로 가연특성을 가지는 탄소 및 산소의 양이 증가하여 난연성을 감소시키는 것으로 나타났다. 하지만, 본 연구에서 합성 및 개질된 질화붕소는 상용화된 질화붕소에 비해 개선된 분산성으로 인해 적은 함량으로 폴리락트산의 난연성을 향상시켰다. 본 연구에서 제시하는 질화붕소의 합성 및 기능화 방법은 가열 조건에 따라 질화붕소의 개질 정도를 조절할 수 있어 향후 다양한 응용 분야에 적용할 수 있는 효과적인 전략이다.

주요어: 인계 난연제, 인-질소계 난연제, 폴리케톤, 폴리염화비닐, 난연성, 질화 붕소, 표면 개질

학 번 : 2018-34202